Universiteit Gent
Faculteit Wetenschappen
Vakgroep Vaste-stofwetenschappen

Advantages and challenges of plasma enhanced atomic layer deposition

Jan Musschoot

Proefschrift voorgelegd tot het behalen van de graad van
Doctor in de Wetenschappen: Fysica
Academiejaar 2010-2011

Universiteit Gent
Faculteit Wetenschappen
Vakgroep Vaste-stofwetenschappen

Promotor: Prof. Dr. Christophe Detavernier

Universiteit Gent
Faculteit Wetenschappen

Vakgroep Vaste-stofwetenschappen
Krijgslaan 281, S1 B-9000 Gent, België

Proefschrift voorgelegd tot het behalen van de graad van
Doctor in de Wetenschappen: Fysica
Academiejaar 2010-2011

Dankwoord

Op de kaft van een doctoraatsthesis staat slechts één auteur, maar vele mensen dragen bij aan het tot stand komen ervan. Daarom ben ik blij hen hier te kunnen bedanken.

Vooreerst mijn promotor Prof. Dr. Christophe Detavernier, voor zijn visie om het ALD onderzoek in Gent op te starten en het vele nalezen van teksten en presentaties. Prof. Dr. ir. Roland Van Meirhaeghe wil ik danken voor zijn inbreng tijdens de aanvang van mijn doctoraatsonderzoek.

Zonder de ontwerpen van Prof. Dr. Em. Johan Haemers ('postdoc Jo') en de know-how en bouwinspanningen van Dr. Davy Deduytsche zouden geen experimenten mogelijk geweest zijn. Davy wordt speciaal bedankt voor de vele keren dat hij een schijnbaar onoverkomelijk probleem in een handomdraai wist op te lossen.

I thank Dr. Qi Xie for the many scientific discussions and for working together on the reactors and experiments. Jolien Dendooven heeft samen met mij over vele ALD problemen nagedacht en ze duidelijker helpen maken.

Uiteraard ook dank aan alle huidige en gewezen leden van de CoCooN onderzoeksgroep: Bob, Boris, Charlotte, Delphine, Geert, Kilian, Koen, Liesje, Shaoren en Werner, alsook de andere S1 collega's voor de leuke jaren. Karl en Marc, de 'ALDers van Imec' mogen zeker niet vergeten worden.

Het werk dat ATP'ers Gilbert, Jo, Lode, Nico en Olivier voor me uitvoerden kon ik ten zeerste waarderen. Ik kon steeds rekenen op Elly en Kristof van het secretariaat bij administratieve problemen.

Eén van de aangenaamste aspecten van dit doctoraatsonderzoek was dat er met verschillende onderzoeksgroepen binnen en buiten de UGent werd samengewerkt. Daarom dank ik graag Prof. Johan Martens, Jens Emmerich en Sreeprasanth Pulinthanathu Sree (KULeuven) en Prof. Pascal Van Der Voort, Ilke Muylaert en Karen Leus (UGent) voor de 'chemische' samenwerking. The brief but very succesful collaboration with Nursen Avci and the other people from Lumilab was appreciated. Ook voor Dr. Koen Martens (Imec), Linny Baeten (UHasselt) en Dr. Michiel Blauw (Holst Center) hoop ik dat de Gentse ALD films hun eigen onderzoek vooruit hebben geholpen. Ik ben alle mensen die metingen voor me gedaan hebben zeer erkentelijk voor hun werk. De co-auteurs van publicaties bedank ik voor de mooie resultaten die we samen behaalden.

Dr. Sven Van den Berghe van het Studiecentrum voor Kernenergie (SCK)

verdient een speciale vermelding. Dankzij hem kon ik cruciale XPS metingen doen in het SCK te Mol en kreeg ik tegelijk ook een inkijk in de 'nucleaire wereld'.

Arne Vansteenkiste, Koen De Keyser en Koen Van Aeken worden bedankt voor de hulp bij LaTeX problemen.

De leden van de jury bedank ik voor het kritisch doornemen van dit proefschrift.

Ik ben het IWT-Vlaanderen erkentelijk voor de financiering van het SBO project 'Metacel', waar dit doctoraatsonderzoek in kaderde.

Jan Musschoot

Table of Contents

List of Abbreviations

A

AAO	anodized aluminum oxide
ALD	atomic layer deposition
ALE	atomic layer epitaxy

C

CMOS	complementary metal-oxide-semiconductor
CMP	chemical mechanical planarization
Cp	cyclopentadienyl
CVD	chemical vapor deposition

D

DEZ	di(ethyl) zinc, $Zn(C_2H_5)_2$
DFT	density functional theory
DRAM	dynamic random access memory

E

Et	ethyl, C_2H_5

G

GPC	growth per cycle

H

HEt	ethane, C_2H_6

I

IC	integrated circuit
ITO	indium doped tin oxide

L

LED	light emitting diode

M

MEMS	micro electromechanical systems
MLD	molecular layer deposition
MOSFET	metal oxide silicon field effect transistor
MIM	metal insulator metal

O

OES	optical emission spectroscopy
OLED	organic light emitting diode

P

PE	plasma enhanced
PE ALD	plasma enhanced atomic layer deposition

PET	poly(ethylene terephthalate)
PID	proportional integral derivative
PTFE	poly(tetrafluoroethylene)
PVD	physical vapor deposition

Q

QMS	quadropole mass spectrometer/quadrupole mass spectroscopy

R

RF	radio frequent
RIE	reactive ion etching
RTA	rapid thermal anneal
RTP	rapid thermal processing

S

SAM	self assembled monolayer
SE	spectroscopic ellipsometry
SEM	scanning electron microscope
SOFC	solid oxide fuel cell

T

TDMAT	tetrakis di(methyl) titanium, $Ti(N(CH_3)_2)_4$
TEM	transmission electron microscope
TMA	tri(methyl) aluminum, $Al(CH_3)_3$
TTIP	titanium tetra(isopropoxide), $Ti(OC_3H_7)_4$

V

VTIP	vanadyl tri(isopropoxide)

W

WVTR	water vapor transmission rate

X

XPS	X-ray photoelectron spectroscopy
XRD	X-ray diffraction
XRF	X-ray fluorescence
XRR	X-ray reflectometry

Nederlandse samenvatting –Summary in Dutch–

Atomic layer deposition (atomaire laagafzetting, ALD) is een techniek om nanometerdunne laagjes (films) af te zetten. ALD is gebaseerd op de opeenvolgende blootstelling van een substraat (dragermateriaal) aan een precursor en een reactief gas. Dit proces resulteert in zelfgesatureerde oppervlaktereacties[1]. Bovendien worden alle oppervlakken van het substraat die blootgesteld zijn aan de precursor en het reactief gas bedekt door de groeiende film. Deze gelijkvormigheid is een voordeel wanneer niet-vlakke substraten behandeld worden. Een belangrijke toepassing van ALD is de productie van geïntegreerde schakelingen. Door zijn uniformiteit werd ALD geaccepteerd in deze veeleisende sector.

Plasma versterkte atomaire laagafzetting (PE ALD) heeft een aantal voordelen in vergelijking met thermische ALD. Een lagedruk, niet-thermisch plasma levert energie aan het reactief gas. Hierdoor word filmgroei op warmtegevoelige dragers mogelijk. Meestal is ook de zuiverheid van PE ALD films hoger dan die van thermische ALD films, waarin soms sporen van de precursor worden teruggevonden.

Het doel van dit werk was een grondige studie te maken van de voor- en nadelen van thermische en plasma versterkte ALD. De depositieprocessen en de overeenkomstige filmeigenschappen van een reeks materialen (TiO_2, V_2O_5, ZnO, TiN en Ru) werden bestudeerd op vlakke substraten.

Om de conformaliteit van thermische en PE ALD te testen, werden deposities op een polyester non-woven gemodelleerd en experimenteel geverifieerd.

De volgende besluiten kunnen getrokken worden uit dit werk:

Titaandioxide werd afgezet met tetrakis(dimethyl)amido titanium (TDMAT) en titanium tetra(isopropoxide) TTIP en verschillende reactanten. ALD met water (zowel thermisch als plasma versterkt) geeft koolstofvrije films. Hoewel een thermisch proces met zuurstof niet in filmgroei resulteert, kunnen films verontreinigd met een weinig koolstof (3.5 % C van TTIP precursor bij een deposition temperature of 210 °C) afgezet worden met een zuurstof-argon plasma.

[1] Bedoeld wordt dat de reacties vanzelf stoppen eens een bepaalde hoeveelheid gas aan het oppervlak gebonden is.

De *as-deposited* films waren amorf. Ze kunnen gekristalliseerd worden door uitgloeien (annealen). In-situ XRD toonde aan dat zuiverdere films kristalliseren bij lagere temperaturen. Een 12 nm dikke film gegroeid met TDMAT en waterplasma bij 150 °C zonder koolstofverontreinigingen kristalliseerde bij 376 °C. Een gelijkaardige film met 2% koolstof, gegroeid met een zuurstof-argon plasma, kristalliseerde zelfs nog niet bij annealen tot 900 °C. Ook de dikte heeft een effect op kristallisatie: een 5 nm dikke, zuivere titania film kristalliseerde bij 472 °C, terwijl een 12 nm dikke zuivere film al bij 373°C kristalliseerde.

Een gedragen TiO_x/SiO_2 (SBA15) katalysator werd met ALD gemaakt. De poriën waren niet geblokkeerd na ALD. De selectiviteit voor de vorming van cyclohexeneoxide uit cyclohexene en tert-butylhydroperoxide was ongeveer 80 % met de TiO_x/SiO_2 katalysator, bijna vier keer hoger dan gebruik makende van een V_2O_5/SiO_2 katalysator.

Het thermisch ALD proces voor de depositie van **vanadiumpentoxide** met vanadyl triisopropoxide en water satureert zeer traag door de trage reactie van water met de groeiende film: bij een depositietemperatuur van 150 °C duurt het 30 s tot de halfreactie afgelopen is. Plasma versterkte processen heffen deze beperking op, doordat er meer reactieve OH en O radicalen op het oppervlak komen. Deze radicalen werden gemonitord met optische emissie spectroscopie (OES). OES detecteerde ook water en koolstofdioxide tijdens de plasmastap. Dit is bewijs van een verbrandingsachtige reactie tussen de gechemisorbeerde liganden en het plasma.

ALD met water als reactant geeft amorfe films verontreinigd met koolstof. Films met minder verontreinigingen kunnen gekristalliseerd worden bij lagere temperaturen: vanadium oxide gegroeid met thermische ALD (6.5 % C) werd kristallijn bij minder dan 450 °C, terwijl de film gegroeid met PE ALD (22 % C) tot boven 450 °C geanneald worden alvorens te kristalliseren. Een zuustofatmosfeer is nodig tijdens het uitgloeien om verlies van O uit de films te vermijden.

Plasma versterkte ALD met een zuurstofplasma geeft zuiver, kristallijn V_2O_5 met een (001) orientatie bij een depositietemperatuur van 150 °C.

Zinkoxide werd gegroeid met diethylzinkprecursor en H_2O (thermische ALD) of O_2 plasma. Nucleatie van de film is sterk afhankelijk van het substraat. Bij thermische ALD op 200 °C duurt het 25 ALD cycli tot de filmdikte lineair begint toe te nemen met het aantal cycli. Alle films waren kristallijn na afzetting. De kristalliniteit volgt een duidelijke trend: meer energie toevoegen aan de groeiende film (door een hogere depositietemperatuur of door plasma) leidt tot ZnO met een preferentiële (001) oriëntatie.

Zinkoxide afgezet met thermische ALD is elektrisch geleidend (0.01 Ωcm voor een film afgezet met 200 ALD cycli, 1 s DEZ en 1 s H_2O per cyclus), terwijl PE ALD ZnO niet geleidend is. Dit verschil kon niet toegeschreven worden aan onzuiverheden, waardoor we aannemen dat het komt door zuurstofvacatures in het thermisch ALD ZnO.

PE ALD van ZnO en zuurstof werd gemonitord met QMS en OES. Opnieuw kan het PE ALD proces beschreven worden met een verbrandingsachtige reactie.

De halfracties van het ALD proces zijn:
(a) OH + DEZ → O-Zn-C_2H_5 + C_2H_6
(b) O-Zn-C_2H_5 + 6 O → O-Zn-OH + CO_2 + CO + 2 H_2O

Titaannitride films werden afgezet met TDMAT. De stap met de TDMAT precursor is niet volledig zelfgesatureerd, maar de filmdikte neemt wel linear toe met het aantal ALD cycli.

De zuiverste films (met minder dan 6 % verontreiniging van C en O) werden afgezet met lange (30 s) blootstellingstijden aan het plasma gedurende iedere cyclus. TiN gegroeid met thermische ALD bij 200 °C was sterk gecontamineerd, met 37 % O en 9 % C. De onzuiverheden hebben een sterke invloed op de elektrische eigenschappen van de films: de zuiverste film had een resistiviteit van 180 $\mu\Omega$cm, terwijl de film afgezet met thermische ALD een resistiviteit van 52 900 $\mu\Omega$cm had.

De koperdiffusiebarriere-eigenschappen van 5 nm dik ALD TiN werd bepaald met in-situ XRD. De temperatuur waarbij de diffusiebarriere gegroeid met ammoniakplasma PE ALD doorbreekt (608 °C), is vergelijkbaar met die van een PVD TiN koperbarriere (594 °C). Rekening houdend met de lage resistiviteit en de goede diffusiebarriere-eigenschappen van de films, kan het beschreven proces bruikbaar zijn voor de productie van barrieres voor Cu interconnects.

Rutheen films werden afgezet met $Ru(EtCp)_2$ en NH_3 plasma op Si(100) en ALD TiN. De *as-deposited* films op Si(100) waren random georiënteerd, op TiN hadden ze een (002) oriëntatie. Na 60 s annealen op 800°C resulteerde korrelgroei in vlakke Ru films met een sterke (002) textuur. Electron backscatter diffraction (EBSD) en transmissie-elektronenmicroscopie (TEM) toonde aan dat de laterale korrelgrootte van de uitgegloeide films enkele honderden nanometer bedroeg, groot in vergelijking met de 10 nm filmdikte. Er werd geen rutheensilicide gevormd door de ALD films op Si(100) te annealen. Door te vergelijken met gesputterde films bleek dat een Si_xN_y reactiebarrierelaag gevormd werd door het ammoniakplasma voor de filmgroei.

Op basis van de bovenstaande processen konden een aantal algemene conclusies over thermische en plasma versterkte ALD getrokken worden. PE ALD maakt filmgroei mogelijk bij lage depositietemperaturen, waarbij thermische ALD reacties ofwel zeer traag ofwel helemaal niet doorgaan. Thermische ALD verloopt door ligandenuitwisseling van de precursoren aan het oppervlak, terwijl PE ALD gekarakteriseerd wordt door een verbrandingsachtige reactie van radicalen met de liganden. Films afgezet met PE ALD bevatten minder onzuiverheden in vergelijking met thermische ALD films.

De **conformaliteit van thermische en plasma versterkte ALD op niet-gewoven vezels** werd gemodelleerd en experimenteel bestudeerd.

Er werd een Monte Carlo gebaseerde simulatiecode ontwikkeld om het transport van de precursor in het vezelsubstraat te bestuderen. De beweging van de precursormolecules kon beschreven worden door ofwel transmissie of reflectie

door een deel van de non-woven, of als depositie op het oppervlak van de vezels. De fysische parameters van het substraat waarmee in het model rekening wordt gehouden zijn de totale oppervlakte van de vezels, de oppervlakdichtheid van de reactieve sites en de sticking coëfficiënt. De relevante eigenschap van het gas is het aantal molecules die op de buitenkant van de non-woven vallen.

Voor de experimenten werd een stuk non-woven in een houder van teflon gestopt. De precursor kon maar langs één kant binnenkomen, waardoor de conformaliteit van ALD op het substraat tot een ééndimensionaal probleem werd herleidt. De conformaliteit van de aluminafilms werd bepaald door de relatieve hoeveelheid Al te meten met EDX.

Er werd aangetoond dat langere precursorpulstijden per cyclus leidden tot een diepere bedekking van de non-woven (gemeten vanaf de opening). De afhankelijkheid tussen pulstijd en bedekking is sub-lineair: verdubbelen van de blootstellingstijd zorgt niet voor een verdubbelde penetratiediepte.

De reden hiervoor is dat molecules uit de non-woven kunnen diffunderen voor ze chemisorberen. Bij een TMA puls van 2 s tonen de simulaties dat 90 % van de precursor de teststructuur verlaat zonder afgezet te worden op de non-woven. Bij een TMA puls van 30 s komt 97 % van de precursor die de teststructuur binnenkwam weer buiten zonder te reageren. De stickingcoëfficiënt variëren van 1 naar 0.01 had weinig effect op het bedekkingsprofiel.

Voor PE ALD beperkt recombinatie van de zuurstofradicalen op het oppervlak van de vezels de bedekking van het substraat tot enkele millimeter vanaf de opening. Voor blootstelling aan 8 s O radicalen, bij aanname van een stickingcoëfficiënt van 0.1 en een recombinatiecoëfficiënt van 0.1, werd berekend dat ongeveer 40 % van de radicalen recombineren tot O_2. Slechts 1 % reageert met de precursorliganden op het oppervlak van de non-woven. De rest van de O radicalen verlaten de teststructuren zonder te reageren.

Na de studie van de conformaliteit van (PE) ALD op non-wovens werd ALD op een aantal andere vezelmaterialen gedemonstreerd. Alumina gedeponeerd op tissuepapier maakt het papier hydrofoob. Dezelfde coating op polyamide lussen maakt de lussen hydrofiel. TEM beelden illustreerden de conforme bedekking van de lussen.

Als mogelijke toepassing van ALD op textiel werd een geweven stuk polyester/katoen gecoat met ZnO. De coating verminderde de groei van Staphyllococcus Aureus bacteriën op de stof.

English summary

Atomic layer deposition (ALD) is a technique for growing nanometer thin films. ALD is based on the sequential exposure of the substrate to a precursor and a reactive gas. This process results in self-saturated surface reactions. Because of this intrinsic property, the film thickness can be controlled be the number of ALD cycles. Furthermore, all surfaces of the substrate that are exposed to the precursor and reactive gas are covered by the growing film. This conformality is an advantage for treating non-planar substrates. One important use of ALD is in the manufacture of integrated circuits. Because of its uniformity, ALD can be used in this highly demanding industry.

Plasma enhanced ALD (PE ALD) has a number of advantages over thermal ALD. A low pressure, non-thermal plasma provides energy to the reactive gas. This enables the growth of films on heat sensitive substrates. Also, the purity of PE ALD films is typically found to be higher than thermal ALD films, where traces of the precursor can sometimes be found.

The goal of this work was to make a thorough study of the benefits and disadvantages of thermal and plasma enhanced ALD. The deposition processes and corresponding film properties of a series of materials (TiO_2, V_2O_5, ZnO, TiN and Ru) were studied on planar substrates.

To test the conformality of thermal and PE ALD, depositions on a polyester non-woven were modeled and verified experimentally.

The work has resulted in the following conclusions:

Titanium dioxide was deposited from tetrakis(dimethyl)amido titanium (TDMAT) and titanium tetra(isopropoxide) TTIP with different reactants. ALD with water (both thermal and PE) leads to carbon free films. While a thermal oxygen process does not result in film growth, oxygen-argon plasma deposits films with some carbon contamination (3.5 % C from TTIP precursor at a deposition temperature of 210 °C).

The as deposited films were amorphous. They can be crystallized by annealing. In-situ XRD demonstrated that purer films crystallize at lower temperatures. A 12 nm thick film grown from TDMAT and water plasma at 150 °C with no carbon impurities crystallized at 376 °C. A similar film containing 2% carbon, grown with a mixed argon-oxygen plasma, did not crystallize even when annealed to 900 °C.

Also the thickness has an effect on crystallization: a 5 nm thick pure titania film crystallized at 472 °C, while a 12 nm thick pure titania film already crystallized at 373°C.

A supported TiO_x/SiO_2 (SBA15) catalyst was made by ALD. No pore blocking was observed. The selectivity towards cyclohexene oxide formation from cyclohexene and tert-butylhydroperoxide was about 80 % using the TiO_x/SiO_2 catalyst, almost 4 times higher than for a V_2O_5/SiO_2 catalyst.

The thermal ALD process for the deposition of **vanadium pentoxide** from vanadyl triisopropoxide and water saturates very slowly because of the slow reaction of water with the growing film: at a deposition temperature of 150 °C, reaching saturation takes 30 s. Plasma enhanced processes overcome this constraint, by offering more reactive species to the surface, such as OH and O radicals. These were monitored by optical emission spectroscopy (OES). OES also detected water and carbon dioxide produced during the plasma step, proof of a combustion-like reaction of the chemisorbed ligands with the plasma.

ALD with water as a reactive gas results in amorphous, carbon contaminated films. Films with less inpurities could be crystallized at lower temperatures: vanadium oxide grown with thermal ALD (6.5 % C) was crystallized below 450 °C while the film grown with PE ALD (22 % C) had to be annealed above 450 °C before crystallizing. An oxygen atmosphere is needed during the anneal to prevent loss of O from the films.

Plasma enhanced ALD with oxygen plasma results in pure, crystalline V_2O_5 with a (001) orientation as deposited at 150 °C.

Zinc oxide was grown from diethyl zinc precursor with either H_2O (thermal) or O_2 plasma. Nucleation of the film is strongly dependant on the substrate. For thermal ALD at a deposition temperature of 200 °C, it takes 25 ALD cycles before the film thickness starts increasing linearly with the number of cycles.

All films were crystalline as deposited. The crystallinity follows a clear trend: enhancing the energy of the growing film (by increasing the deposition temperature or using PE ALD) results in ZnO with a (001) preferential orientation.

Zinc oxide deposited by thermal ALD is electrically conductive (0.01 Ω cm for a film grown with 200 cycles, 1 s DEZ and 1 s H_2O per cycle), while PE ALD ZnO is not. This difference could not be attributed to impurities, so it is believed to stem from oxygen vacancies in the thermal ALD ZnO.

PE ALD of ZnO and oxygen was monitored by QMS and OES. Again, a combustion-like reaction describes the PE ALD process. The half-reactions are

(a) OH + DEZ $\rightarrow$ O-Zn-C_2H_5 + C_2H_6

(b) O-Zn-C_2H_5 + 6 O $\rightarrow$ O-Zn-OH + CO_2 + CO + 2 H_2O

Titanium nitride films were grown by atomic layer deposition from TDMAT. The TDMAT exposure step is not fully self-saturating, but the film thickness does increase linearly with the number of ALD cycles.

The purest films (less than 6 atom % C and O impurities) were grown with long (30 s) plasma exposure time during each cycle. TiN grown from thermal ALD at 200 °C was severely contaminated, containing 37 % O and 9 % C. The impurities strongly affect the electrical properties of the films: the purest film had a resistivity of 180 $\mu\Omega$cm, while the film grown with thermal ALD had a resistivity of 52 900 $\mu\Omega$cm.

The copper diffusion barrier properties of 5 nm thick ALD TiN was determined by in-situ XRD. The breakdown temperature of the ALD diffusion barrier grown by ammonia PE ALD (608 °C) is comparable to that of a PVD grown TiN copper barrier (594 °C). Taking into account the low resistivity and good diffusion barrier properties of the films, the described process can be useful for the production of Cu interconnect diffusion barrier layers.

Ruthenium films were grown from $Ru(EtCp)_2$ and NH_3 plasma on Si(100) and ALD TiN. The as-deposited films on Si(100) were randomly oriented, on TiN they were (002) oriented. After annealing at 800°C for 60 s, grain growth resulted in smooth Ru films with a strong (002) texture. Electron backscatter diffraction (EBSD) and transmission electron microscopy (TEM) demonstrated that the lateral grain size of the annealed films was several 100 nm, which was large compared to the 10 nm thickness of the films. No ruthenium silicide was formed by annealing the ALD Ru films on Si(100). Comparison with sputter deposited films learned that this occurred because the ammonia plasma created a SiO_xN_y reaction barrier layer prior to film growth.

Based on the various processes that were studied, a number of general conclusions regarding thermal and PE ALD could be drawn. PE ALD enables film growth at low deposition temperatures, for which thermal ALD reactions are either very slow or not occurring at all. Thermal ALD proceeds by ligand exchange of the precursors at the surface, while PE ALD is characterized by a combistion like reaction of radicals with the ligands. Films grown with PE ALD contain less impurities compared to films grown with thermal ALD.

The **conformality of thermal and plasma enhanced ALD on non-woven fibers** was modeled and studied experimentally.

A Monte Carlo based simulation code was developed to study the transport of the precursor in the fiber substrate. The motion of the precursor molecules could be described either as transmission or reflection through a part of the non-woven, or as deposition on the fiber surface. The physical parameters of the substrate taken into account in the model are the total fiber surface area, the surface density of reactive sites and the sticking coefficient. The relevant gas property is the number of particles impinging on the outside of the non-woven.

Experimentally, a piece of non-woven was confined in a Teflon holder. The precursor could only enter through one side, thus enabling us to study the conformality on the substrate in a one-dimensional way. The conformality of the alumina films was determined by measuring the relative Al concentration with EDX.

It was demonstrated that increasing the precursor pulse time per cycle led to a deeper and more homogeneous coverage of the nonwoven (measured from the opening). The dependence is sub-linear: doubling the exposure time does not result in a doubling of the penetration depth. The reason for this is that molecules can diffuse out of the non-woven before chemisorbing. For a TMA pulse time of 2 s, the simulations show that 90 % of the precursor escapes the test structure without being deposited on the non-woven. For a TMA pulse time of 30 s, 97 % of the precursor that enters the test structure leaves without reacting. Varying the sticking coefficient from 1 to 0.01 had little effect on the coverage profile.

For PE ALD, recombination of the oxygen radicals at the fiber surface limits the coverage of the substrate to a few millimeter from the opening. For 8 s of O radical exposure, assuming a sticking coefficient of 0.1 and a recombination coefficient of 0.1, it was calculated that about 40 % of the radicals recombine to O_2. Only 1 % reacts with the precursor ligands at the surface of the non-woven. The rest of the O radicals leave the test structure unreacted.

After the study of (PE) ALD conformality on non-wovens, ALD on a number of other fiber based materials was demonstrated. Alumina deposited on tissue paper makes the paper hydrophobic. The same coating on polyamide loops made the loops hydrophilic. The conformal coverage of the loops was illustrated by TEM images.

As a potential application of ALD on textiles, a woven polyester/cotton blend was coated with ZnO. The coating reduced the growth of Staphyllococcus Aureus bacteria on the fabric.

1 Introduction

1.1 Goals of this thesis

Atomic layer deposition is a technique for depositing very thin films. It has the advantages of precise thickness control and the ability to coat substrates conformally at modest deposition temperatures (<400 °C). After starting with a limited number of applications, interest in ALD for growing high-k gate oxides picked up in the 1990s. A second wave of researchers got involved after the year 2000, because ALD is increasingly being considered to be a generic coating technique for all sorts of nanostructures. The present work also fits into this framework: it is not focused at microelectronics, but rather takes a wider look at the possibilities of ALD.

When I started the research presented in this thesis in April 2007, I was the first Ph. D. student in the CoCooN (Coating and Contacting of Nanostructures) research group to work on ALD full time. At that moment, the group had one home-made PE ALD reactor. We needed ALD processes for growing different films. Therefore, **the first goal of this work was developing a set of ALD processes.** This work has a rather technological nature. The availability of these processes has enabled several interdisciplinary research projects in fields ranging from catalysis to sensors and microelectronics. The selected materials were oxides (TiO_2, V_2O_5, ZnO), TiN and Ru.

The second goal was to investigate the difference between thermal and plasma enhanced ALD. This was more fundamental science, relating film prop-

erties with (PE) ALD process parameters. For this study, a number of in-situ and ex-situ characterisation methods were used. Because of the importance of ALD conformality, we tested this property for both thermal and PE ALD on non-woven fibers. A fibrous material was chosen as substrate for the conformality study as a result of the collaboration we had with Centexbel and the textile department of HoGent. Both institutions participated in the 'Metacel' project, an SBO[1] project of the IWT[2], which funded this work.

1.2 Outline

The work consists of three major parts: an introduction to thermal and PE ALD, a description of ALD and PE ALD processes that were studied during this PhD, and ALD on textile substrates. Chapter 2 gives an introduction into the basics of ALD. In chapter 3, ALD applications and reactor designs discussed in literature are reviewed. The reactors and characterization methods used in this work are summarized in chapter 5. In chapters 6 to 10, different ALD processes are discussed. This thesis mainly focusses on the differences between thermal and PE ALD. For each material, a number of properties which are relevant for applications were measured. For ease of characterization, planar silicon wafer pieces were used. In chapter 11, ALD is done on textile fibers, as an illustration of the conformal film growth.

1.3 Publications and conference contributions

1.3.1 Publications related to this work

- "Growth kinetics and crystallization behavior of TiO_2 films prepared by plasma enhanced atomic layer deposition"
  J. Electrochem. Soc. **155** H688-H92 (2008)
  Q. Xie, J. Musschoot, D. Deduytsche, R. L. Van Meirhaeghe, C. Detavernier, S. Van den Berghe, Y.-L. Jiang, G.-P. Ru, B.-Z. Li and X.-P. Qu

- "Diffusion barrier properties of TaN_x films prepared by plasma enhanced atomic layer deposition from PDMAT with N_2 or NH_3 plasma"
  Microelectron. Eng. **85** 2059-2063 (2008)
  Q. Xie, J. Musschoot, C. Detavernier, D. Deduytsche, R. L. Van Meirhaeghe, S. Van den Berghe, Y.-L. Jiang, G.-P. Ru, B.-Z. Li and X.-P. Qu

[1] SBO: Strategisch Basisonderzoek (Eng: strategic fundamental research)
[2] IWT: agentschap voor Innovatie door Wetenschap en Technologie (Eng: agency for Innovation by Science and Technology)

- "Atomic layer deposition of titanium nitride from TDMAT precursor"
  Microelectron. Eng. **86** 72-77 (2009)
  J. Musschoot, Q. Xie, D. Deduytsche, S. Van den Berghe, R. L. Van Meirhaeghe and C. Detavernier

- "Modeling the conformality of atomic layer deposition: the effect of sticking probability"
  J. Electrochem. Soc. **156** P63-P67 (2009)
  J. Dendooven, D. Deduytsche, J. Musschoot, R. L. Van Meirhaeghe and C. Detavernier

- "Ru thin film grown on TaN by plasma enhanced atomic layer deposition"
  Thin Solid Films **517** 4689-4693 (2009)
  Q. Xie, Y.-L. Jiang, J. Musschoot, D. Deduytsche, C. Detavernier, R. L. Van Meirhaeghe, S. Van den Berghe, G.-P. Ru, B.-Z. Li and X.-P. Qu

- "Comparison of thermal and plasma-enhanced ALD/CVD of vanadium pentoxide"
  J. Electrochem. Soc. **156** P122-P126 (2009)
  J. Musschoot, D. Deduytsche, H. Poelman, J. Haemers, R. L. Van Meirhaeghe, S. Van den Berghe and C. Detavernier

- "Microencapsulation of moisture-sensitive CaS:Eu^{2+} particles with aluminum oxide"
  J. Electrochem. Soc. **156** J333-J337 (2009)
  N. Avci, J. Musschoot, P. F. Smet, K. Korthout, A. Avci, C. Detavernier and D. Poelman

- "Conformality of Al_2O_3 and AlN deposited by plasma-enhanced atomic layer deposition"
  J. Electrochem. Soc. **157** G111-G116 (2010)
  J. Dendooven, D. Deduytsche, J. Musschoot, R. L. Van Meirhaeghe and C. Detavernier

- "Texture of atomic layer deposited ruthenium"
  Microelectron. Eng. **87** 1879-1883 (2010)
  J. Musschoot, Q. Xie, D. Deduytsche, K. De Keyser, D. Longrie, J. Haemers, S. Van den Berghe, R. L. Van Meirhaeghe, J. D'Haen and C. Detavernier

- "Ultrathin GeO_xN_y interlayer formed by in situ NH_3 plasma pretreatment for passivation of germanium metal-oxide-semiconductor devices"
  Appl. Phys. Lett. **97** 222902 (2010)
  Q. Xie, J. Musschoot, M. Schaekers, M. Caymax, A. Delabie, X.-P. Qu, Y.-L. Jiang, S. Van den Berghe, J. Liu and C. Detavernier

- "TiO_2/HfO_2 bi-layer gate stacks grown by atomic layer deposition for germanium-based metal-oxide-semiconductor devices using GeO_xN_y passivation layer"
  Electrochem. Solid-State Lett. **14** G27-G30 (2011)
  Q. Xie, J. Musschoot, M. Schaekers, M. Caymax, A. Delabie, D. Lin, X.-P. Qu, Y.-L. Jiang, S. Van den Berghe and C. Detavernier

- "TaCN growth with PDMAT and H_2/Ar plasma by plasma enhanced atomic layer deposition"
  Microelectron. Eng. **88** 646-650 (2011)
  Q. Xie, D. Deduytsche, J. Musschoot, R. L. Van Meirhaeghe, C. Detavernier, S.-F. Ding and X.-P. Qu

- "Conformality of thermal and plasma enhanced atomic layer deposition on a non-woven fibrous substrate"
  in preparation (2011)
  J. Musschoot, J. Dendooven, D. Deduytsche, J. Haemers, G. Buyle and C. Detavernier

- "Atomic layer deposition of titanium and vanadium oxide on mesoporous silica and phenol/formaldehyde resins: the effect of the support in the liquid phase epoxidation of cyclohexene"
  submitted (2011)
  I. Muylaert, J. Musschoot, J. Dendooven, C. Detavernier and P. Van Der Voort

- "The coordinative saturated vanadium MIL-47 as a low leaching heterogeneous catalyst in the oxydation of cyclohexene"
  submitted (2011)
  K. Leus, M. Vandichel, Y.-Y. Liu, I. Muylaert, J. Musschoot, H. Vrielinck, F. Callens, G. B. Marin, C. Detavernier, Y. Z. Khimyak, M. Waroquier, V. Van Speybroeck and P. Van Der Voort

1.3.2 Other publications

- "Influence of the geometrical configuration on the plasma ionization distribution and target erosion profile of a rotating cylindrical magnetron: a Monte Carlo simulation"
  J. Phys. D: Appl. Phys. **39** 3989-3993 (2006)
  J. Musschoot, D. Depla, G. Buyle, J. Haemers and R. De Gryse

- "Investigation of the sustaining mechanisms of dc magnetron discharges and consequences for I-V characteristics"
  J. Phys. D: Appl. Phys. **41** 015209 (2008)
  J. Musschoot, D. Depla, G. Buyle, J. Haemers and R. De Gryse

- "Observation of hysteresis in a non-reactive magnetron discharge"
  Plasma Sources Sci. Technol. **17** 015010 (2008)
  J. Musschoot, D. Depla, J. Haemers and R. De Gryse

- "Qualitative model of the magnetron discharge"
  Vacuum **84** 488-493 (2010)
  J. Musschoot and J. Haemers

1.3.3 Conference contributions

- "A comparison of thermal and plasma enhanced ALD of TiO_2 and TiN with TDMAT" (poster)
  J. Musschoot, Q. Xie, D. Deduytsche, R. Van Meirhaeghe and C. Detavernier at E-MRS Fall Meeting, Warsaw, Poland (September 17-21, 2007)

- "Conformality of thermal and plasma enhanced ALD" (poster)
  J. Dendooven, J. Musschoot, D. Deduytsche, R. Van Meirhaeghe and C. Detavernier at ALD 2008, Bruges, Belgium (June 30 - July 1, 2008)

- "ALD of TaN, TiN and Ru for application as diffusion barrier" (poster)
  J. Musschoot, Q. Xie, D. Deduytsche, R. Van Meirhaeghe and C. Detavernier at ALD 2008, Bruges, Belgium (June 30 - July 1, 2008)

- "Thermal versus plasma-enhanced ALD: growth kinetics and conformality"
  C. Detavernier, J. Dendooven, D. Deduytsche and J. Musschoot at 214th Electrochemical Society Meeting, Honolulu, HI, USA (October 13-15, 2008)

- "Comparison of the Ru thin films grown on Si, TiN/Si and TaN/Si substrates by plasma enhanced atomic layer deposition"
  Q. Xie, J. Musschoot, C. Detavemier, D. Deduytsche, R. L. Van Meirhaeghe, Y. L. Jiang, G. P. Ru, B. Z. Li and X. P. Qu at 9th International Conference on Solid-State and Integrated-Circuit Technology, Beijing, China (October 20-23, 2008)

- "ALD of TiN and Ru"
  J. Musschoot, Q. Xie, D. Deduytsche, K. De Keyser, J. D'Haen, S. Van den Berghe, R. Van Meirhaeghe and C. Detavernier at ICTF14, Ghent, Belgium (November 20, 2008)

- "ALD of vanadium oxide"
  J. Musschoot, D. Deduytsche, R. L. Van Meirhaeghe and C. Detavernier at 216th Electrochemical Society Meeting, Vienna, Austria (October 5, 2009)

- "Conformality of Al_2O_3 deposited by thermal, plasma-enhanced and ozone-based atomic layer deposition"

J. Dendooven, D. Deduytsche, J. Musschoot and C. Detavernier at ALD 2010, Seoul, Korea (June 22, 2010)

- ”Conformality of atomic layer deposition on non-wovens” (poster)
  J. Musschoot, J. Dendooven, D. Deduytsche, C. Detavernier and G. Buyle at ALD 2010, Seoul, Korea (June 22, 2010)

2 What is (PE) ALD?

Atomic layer deposition (ALD) is a film deposition technique based on the sequential use of self-terminating gas-solid reactions [275].

The key features of ALD are its high film quality, low deposition temperature, sub-nanometer control of film thickness and the ability to conformally coat non-planar substrates. Because of these advantages, ALD complements or even rivals with other thin film deposition methods, such as sputtering, evaporation, chemical vapor deposition, sol-gel deposition or electroplating.

The fundamental concepts of ALD are briefly explained below. Interested readers can find more details in a number of review articles on ALD [229] [194] [147] [275] [172] [152] [87]. Because of the focus in this work on plasma enhanced (PE) ALD, PE ALD is discussed in a separate section.

2.1 Ideal ALD: self-limiting surface reactions

Some surface science needs to be introduced before we can discuss how ALD works.

2.1.1 Gas-surface interactions

A molecule close to a solid is attracted to the surface by van der Waals or dipole forces. When a particle colliding with the surface is not reflected back to the gas, it can be weakly bound or physisorbed to the surface. Physisorbed molecules can be desorbed by thermal energy, light or electrons. For ALD, the most important

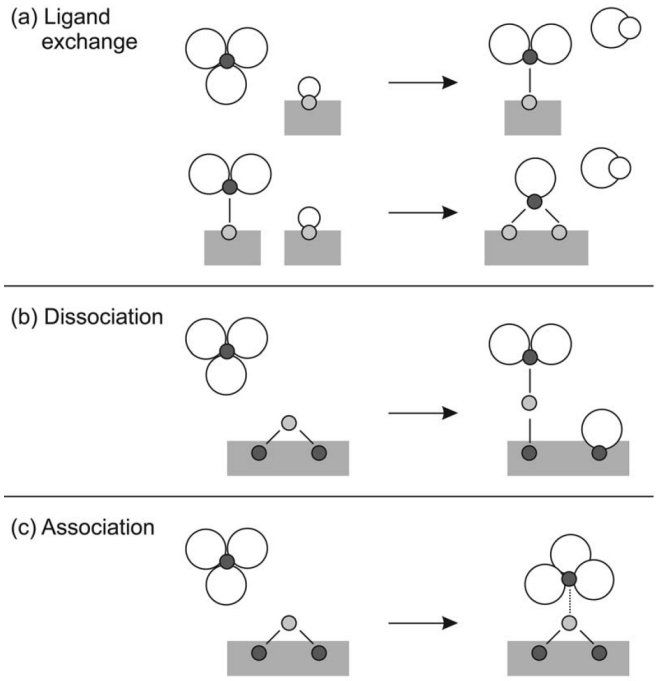

Figure 2.1: Three different mechanisms for chemisorption, illustrated by a molecule with 3 ligands. Taken from [275].

particle-surface interaction is chemisorption: molecules get chemically bound to the surface. Figure 2.1 shows three chemisorption mechanisms. A molecule impinging on a surface can get bound to it by exchanging part of the molecule with a chemical group of the surface (fig. 2.1(a)). The reaction product is shown to desorb from the surface. Alternatively, the molecule can dissociate into fractions, of which some or all stay at the surface (fig. 2.1(b)). Another possibility is association: the intact molecule is bound to the surface (fig. 2.1(c)).

For completeness, it should be mentioned that molecules can diffuse over the surface if there are no significant energy barriers between adsorption sites.

2.1.2 Limitations of chemisorption

When chemisorption is only possible at reactive sites such as OH groups, no molecules will bind to the surface when the reactive sites are not available. ALD uses molecules that, when chemisorbed, do not offer reactive sites to identical molecules. Otherwise, film growth would continue as long as there is exposure to the gas. In the ideal case, perfect self-saturated chemisorption means that a sin-

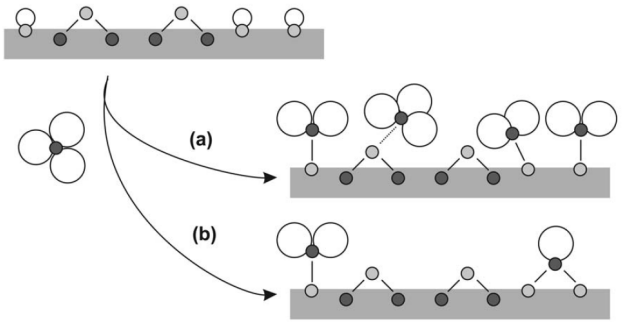

Figure 2.2: Chemisorbtion on the surface limited by (a) steric hindrance, (b) nature of surface groups. Taken from [275].

gle chemisorption eventually occurs on all reactive sites. In reality, there are two limiting factors for chemisorption.

Firstly, assume that the molecule can chemisorb on each site of the uncovered surface. After chemisorption of a (sub)monolayer of molecules, the adsorbed molecules block access of the remaining reactive sites to the gas preventing saturation of all reactive sites during 1 cycle. This is called steric hindrance (fig 2.2(a)).

Secondly, it could be that molecules can only chemisorb on specific sites at the surface, as shown in figure 2.2(b).

The surface density and nature of the reactive sites depends on the substrate material and on the chemical/thermal pretreatment. For crystalline substrates, the surface density is a function of the orientation. This is important for the first cycles of HfO_2 ALD gate on silicon in a FinFET (a 3D structure which larger gate area) [242], for example.

2.1.3 Atomic layer deposition: film growth by self-limiting half-reactions

Films are deposited by repeating ALD cycles, and every cycle consists of 4 steps (figure 2.3):

1. Exposing the substrate to a precursor vapor
2. Purging/evacuating the reactor
3. Exposing the substrate to a reactive gas
4. Purging/evacuating the reactor

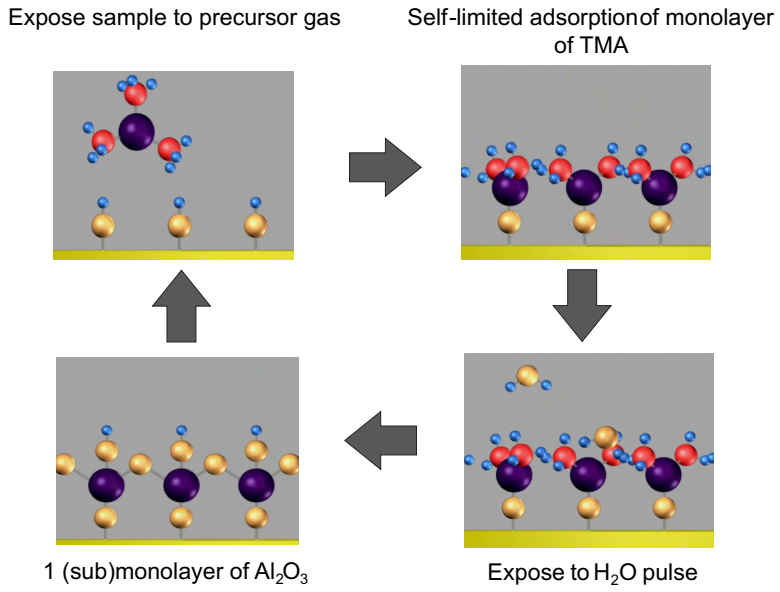

Figure 2.3: Schematic representation of one ALD cycle in the TMA-H_2O ALD process for growing Al_2O_3. Figures taken from [30].

In the first step, the substrate surface is exposed to a precursor. The precursor is a volatile compound[1] consisting of a metal atom and ligands. These ligands are typically halides (e. g. Cl, F) or organic groups (e. g. methyl, isopropoxide or dimethylamido groups)[2]. The precursor chemisorps in a self-limiting way onto the surface. Once the surface is covered with a (sub)monolayer of precursor, no further reactions occur. In the next step, excess precursors molecules are removed by pumping or purging the reactor. During the third step, a second reactant (called the 'reactive gas') reacts self-limitingly with the ligands of the chemisorbed precursor. For the deposition of oxide films, water is a typical reactant. H_2S can be used for the deposition of sulfides. Finally, the second reactant that did not react with the surface is removed and another ALD cycle can begin.

Because the precursor and reactive gas are not in the reactor at the same time and place, no gas phase reactions occur. This should be contrasted with chemical vapor deposition (CVD), where reactants are typically mixed in the gas phase. The self-limiting reactions guarantee that ALD is insensitive to differences in precursor flux on the substrate in the reactor. Excess precursor simply does not react. The self-limiting nature of the half-reactions have the additional advantage that ALD

[1] Rarely, atomic precursors like Zn have been used , see [361]
[2] A summary of different ligands used in literature can be found in figure 4 of [275].

films closely follow the shape of their substrate, i.e. they are conformal. Think of a deep pore with a gas above it. For deposition techniques where the deposition rate is proportional to the flux of incoming material (e. g. sputter deposition), material is mainly deposited at the top of the pore and not deeper at the walls of the pore. In ALD however, once the surface near the entrance of the pore is covered, no further deposition takes place there. The precursor molecules can diffuse into the structure until they are chemisorbed on a reactive site. As a result, films with a uniform thickness are grown, even on objects with complex 3D structures and clogging of the pore entrance is avoided. One ALD pulse results in the increase of the film thickness with a constant amount. Therefore, it is customary to speak of the growth per cycle (GPC, the increase in film thickness per cycle), rather than a growth rate (in nm/s). With a constant GPC, the film thickness can easily be controlled by the number of ALD cycles.

The most popular and best studied ALD reaction [275] is thermal ALD of Al_2O_3 with trimethylaluminum (TMA) and H_2O (figure 2.3). The half reactions are

(a) $Al(OH)_x$ (surf) + $Al(CH_3)_3 \rightarrow AlOAl(CH_3)_{3-x}$ + x CH_4
and
(b) $Al(CH_3)_x$ (surf) + x $H_2O \rightarrow Al(OH)_x$ (surf) + x CH_4,

where (surf) indicates surface species. The TMA molecule is chemisorbed by ligand exchange with one or several hydroxyl groups at the surface[3]. The methane (CH_4) that is formed desorps from the surface. During the water pulse, H_2O reacts with the methyl (CH_3) ligands to form CH_4 and surface hydroxyl groups.

It should be noted that the half-reactions can be rather complex. For example, an ALD process for tungsten [347] proceeds by

(a) WSiH (surf) + $WF_6 \rightarrow WWF_3$ (surf) + $SiHF_3$
(b) WF_3 (surf) + $Si_2H_6 \rightarrow$ WSiH (surf) + $SiHF_3$ + 2 H_2.

Some ALD reactions are catalysed, e. g. by ammonia during the growth of SiO_2 from tetraethoxysilane (TEOS) and water [75]. FTIR indicated that a strong hydrogen bond between NH_3 and SiOH at the surface activates the oxygen in SiOH for nucleophilic attack of TEOS. During the water pulse, ammonia makes oxygen in H_2O more reactive. The catalytic process enables thermal ALD of silica at room temperature [75].

Another remarkable ALD process is the growth of Ru with O_2. Combining mass spectroscopy and QCM measurements, Aaltonen et al. have shown that

[3]Hydroxyl groups that do not react during the precursor pulse are embedded in the films, leading to oxygen rich metal oxides with OH impurities [261].

oxygen dissociates at the surface, and the O atoms can diffuse into the growing film [1]. During the Ru precursor pulse, these subsurface atoms react with the ligands of the adsorbed precursor[4]. The reaction chemistry of noble metal ALD has been discussed in detail by Elliott [67]. A general discussion on the surface chemistry of ALD for electronic devices can be found in [365].

2.1.4 Relation between process parameters and film growth

For each half-reaction, we call the surface density of chemisorbed molecules σ and the saturated surface density σ_{sat}. To model the self-limiting nature of ALD, a sticking coefficient S is introduced. This is the probability that a precursor impinging on the surface is chemisorped. S is modeled by the Langmuir equation [94] [51]:

$$S = S_0(1-\theta),$$

where $\theta = \frac{\sigma}{\sigma_{sat}}$ is the relative surface coverage of the chemisorbed reactant. S_0 is the sticking coefficient at zero coverage. Because chemisorption is a thermally activated process, $S_0 \propto exp^{\frac{-E_A}{k_B T}}$ [297], with E_A the energy barrier, k_B the Boltzman constant and T the deposition temperature[5].

The flux, i.e. the number of particles impinging on a surface per time unit and surface area is called J. The change of the surface coverage as a function of time is

$$\frac{d\theta}{dt} = S_0(1-\theta)J(t)$$

For a constant flux, integrating the equation gives

$$\theta = 1 - exp(\frac{-JS_0t}{\sigma_{sat}})$$

For an ideal gas of particles with mass m, pressure P and temperature T, the flux is given by [94]

$$J = \frac{P}{\sqrt{2\pi m k_B T}}.$$

This shows that a increasing the precursor pressure reduces the precursor pulse time needed to saturate the half-reaction.

[4] A similar reaction mechanism was proposed for vapor liquid solid growth of nanowires [172]

[5] The surface chemistry can in principle be modeled by density functional theory (DFT) calculations, e. g. [66] [288].

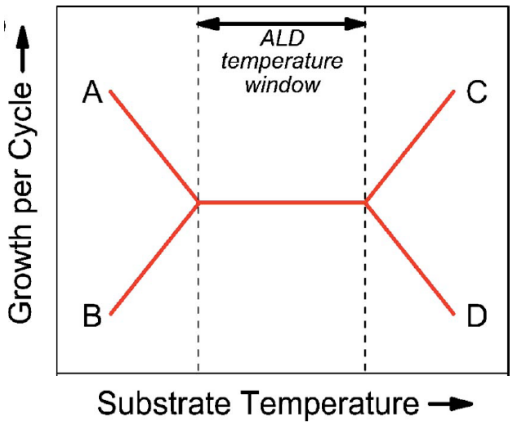

Figure 2.4: Different scenarios of GPC as a function of deposition temperature. For ideal ALD, the GPC is constant in a certain temperature range, called the ALD window. At low temperatures, the GPC can rise due to precursor condensation (a) or fall because of incomplete reactions (b). At temperatures above the ALD window, a rising GPC (c) indicates precursor decomposition while a lower GPC (d) is a consequence of precursor desorption or loss of surface species. Taken from [261].

2.2 Non-ideal ALD

2.2.1 ALD temperature window

When the ALD process is ideal (self-saturating half-reactions, resulting in a constant GPC) for a range in the deposition temperature, this range is called the ALD window. However, real ALD processes do not always proceed like this. Figure 2.4 illustrates different mechanisms resulting in non-ideal growth.

At low temperatures, it is possible that the precursor condenses. Multiple molecular layers are physisorbed on the substrate. During the purge step, the non-chemisorbed precursors do not all desorp. They react with the reactive gas during the third step in the ALD cycle. The resulting film is thicker than it would be when only a chemisorbed layer had been at the surface.

Another possibility at low deposition temperature is that the reaction occurs so slowly (S_0 is small), that the reaction of the precursor with the substrate has not terminated. The GPC is lower than it could be at longer exposure times.

At high deposition temperatures, the precursor molecules can decompose. Chemisorption does not need specific surface sites and the reaction does not saturate. The film thickness increases with the exposure to the precursor. Growth occurs by thermal decomposition, i.e. in a CVD mode, which limits the conformality. Moreover, the film is usually quite severely contaminated by elements from the ligands.

Finally, the equilibrium surface density of reactive sites depends on the tem-

perature [275] [261]. For example, at high temperatures, silica loses silanol (OH) groups [370]. This leads to a reduced GPC at high temperatures.

2.2.2 Nucleation effects

In the beginning of ALD film growth, the number and nature of the reactive sites at the substrate can differ from the reactive sites on a growing film that fully covers the substrate. Figure 2.5 shows four possible evolutions of GPC during the initial stages of growth.

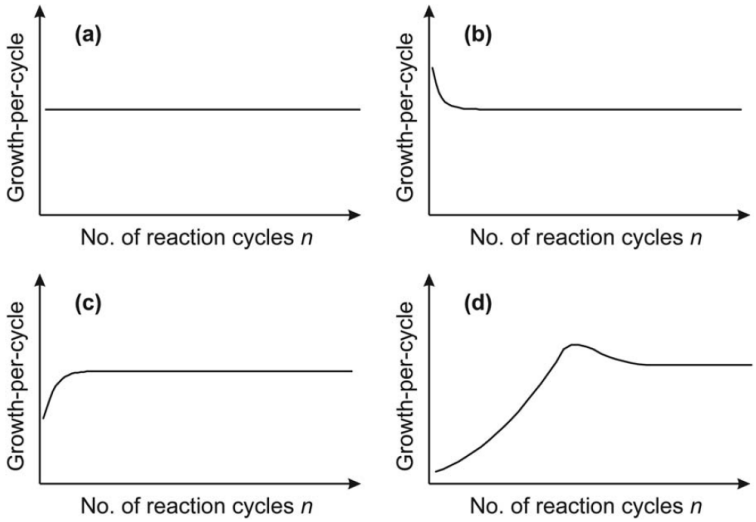

Figure 2.5: GPC as a function of the number of cycles. The different possible regimes are (a) constant, (b) surface enhanced, (c) type 1 surface inhibited and (d) type 2 surface inhibited growth. Taken from [275].

A constant GPC as in figure 2.5(a) indicates that the reactive site density on the substrate and film are equal. Surface enhanced (fig 2.5(b)) or type 1 surface inhibited [274] (fig 2.5(c)) growth indicate that the density of reactive sites on the substrate is higher or lower than on the ALD film, respectively. For some ALD processes the GPC starts low, reaches a maximum and then declines to a constant value (figure 2.5(d)). This type 2 surface inhibited growth has been modeled as follows. Deposition starts at a limited number of nucleation sites. More material is deposited on these nuclei during the next cycles. The nuclei grow into islands on the substrate and a discontinuous, rough coating is formed. The combined surface area of the islands exceeds the surface area of the original substrate. Once the islands start coalescing, the film roughness and the GPC decrease. A more thorough discussion can be found in [275] [274]. Nilssen et al. have simulated the effect

of island formation for amorphous [230] and crystalline [231] [232] ALD films. The absence of ALD at surfaces lacking reactive sites is exploited in area selective ALD (e. g. [224] [172]). This enables the patterned growth of films, rather than a homogeneous coverage of the substrate. A polymer or a self assembled monolayer (SAM) covers the substrate on places where no film is desired. After deposition, the sacrificial layer is removed. Unlike in conventional lithography where film is deposited on a photoresist, no ALD film grows on the polymer or SAM.

2.3 Plasma enhanced (PE) ALD

2.3.1 Plasmas and materials processing

Plasmas are partially or fully ionized gases. Gases can be ionized by thermal energy, electric fields, beams of energetic particles or by electromagnetic radiation. The sun, earth's ionosphere and lightning are examples of natural plasmas. Man made plasmas are used in very diverse technologies such as neon lights, gas lasers, waste disposal [81] and even as a tool for dentists [323]. Arc welding and plasma spraying are examples of material processing technologies based on high temperature plasmas. In thin film processing, low pressure, non-thermal plasmas are frequently used. Magnetron sputter deposition and reactive ion etching (RIE) both rely on a plasma to grow and remove films, respectively.

Low pressure plasmas are usually not in thermal equilibrium. Free electrons have much higher energies (several electron volt, with 1 eV corresponding to more than 10^4 K) than the atoms which are approximately at reactor temperature (typically 500 K in this work). Since chemistry is determined by the valence electrons, the plasma species are very reactive. The free electrons excite or ionize molecules in the plasma. For example, oxygen (O_2) can dissociate in two oxygen radicals. These O radicals are very aggressive oxidants[6]. The high reactivity of PE ALD enables ALD at low deposition temperatures.

2.3.2 Plasma - surface interactions

In addition to the earlier described physisorption and chemisorption, some other phenomena occur at surfaces exposed to a plasma. When a plasma is in contact to a wall, a bias voltage develops between the quasi-neutral plasma and the wall. This voltage accelerates ions to the substrate. When the ions have sufficient energy, they can result in the removal of substrate atoms, a process called sputtering. The energetic ions could also be implanted in the substrate, or create defects in it. Ions, electrons and photons impinging on a surface can stimulate the emission of

[6] Alternative strong oxidizers used in ALD include hydrogen peroxide (H_2O_2) and ozone (O_3).

electrons. Energetic particles that fall on the surface cause localized heating. Radicals from the plasma that recombine on a surface heat the substrate as well [133]. The recombination of radicals near the entrance of high aspect ratio substrates can severely limit the flux of reactive species deeper into the structures [52] [174]. The effect of plasma ions and UV photons on the ALD process has been investigated very recently by Profijt et al. [263].

2.3.3 Typical plasma parameters during PE ALD

In a remote H_2-N_2 plasma used for PE ALD of TiN, an ion density of 10^9 cm^{-3} has been measured [107]. The plasma was generated by an RF coil injecting 100 W into the discharge. The pressure of the gas mixture (90 % H_2, 10 % N_2) was about 0.7 Pa. This corresponds to a H_2 density in the order of 10^{14} cm^{-3}. Clearly, the ionization degree in the ALD plasma is low. The electron temperature in the H_2-N_2 plasma above the substrate was 3.5 eV. The energy of ions impinging on the substrate was ≈15 eV.

For O_2 plasma enhanced ALD, ion energies up to 35 eV have been measured [263]. The ion flux towards the surface was 10^{12}-10^{14} cm^{-2} s^{-1}.

2.3.4 Reactions typical for PE ALD

A number of pure metallic films (e. g. Ta [148] [299], Ti [299], Cu [151], Ni [34], Pd [163]) have been atomic layer deposited with a hydrogen plasma to reduce the metal. It was proposed [146] that H_2 PE ALD works by a Eley-Rideal mechanism: hydrogen radicals from the plasma hit chemisorbed ligands, react with them and the formed molecule desorps from the surface. This is in contrast to thermal ALD, where H_2 is adsorbed on the substrate before reacting with the ligands [146]. Unlike ligand exchange reactions (fig. 2.1(a)), no ligands stay at the surface after the hydrogen half-reaction.

Oxides with high purity and density can be grown at low deposition temperatures by oxygen plasma ALD [261]. Heil et al. have shown that during the plasma step, O radicals react with organic ligands on the growing film to form CO_2, CO and H_2O [109]. Infrared studies have demonstrated that CO and CO_2 result in the formation of carbonate (CO_3), bicarbonate (HCO_3) and formate (HCOO) groups at the surface of ALD TiO_2 [283] and Al_2O_3 [284]. Similar chemical groups had been observed during ALD with ozone [93] [282]. Furthermore, OH groups were detected following the O_2 plasma step, probably a result of H_2O activated in the plasma [283].

However, it was further shown that a prolonged exposure of the carbon containing surface groups to oxygen plasma breaks them into CO_2 or CO [284]. As a result, OH groups are the dominant reactive site, just as in thermal ALD. This

contrasts to ALD with ozone, where it was found that carbonate groups only decompose at high temperatures (>300°C) [93], and carbonate has been found in O_3 ALD films [245].

2.4 History, trends and developments

Atomic layer deposition (formely known as atomic layer epitaxy, ALE) was developed independently by V. B. Aleskovskii in the Soviet Union in the late 1960s and T. Suntola in Finland in the early 1970s. Figure 2.6 illustrates the annual number of ALD[7] publications, indexed in the ISI Web of Knowledge. From 1990 onwards, ALD research intensified due to the need for thinner films in microelectronics. The number of ALD papers is booming since 2002. Although ALD has been done for more than 40 years already, the graph explains why it is still relatively new to many researchers.

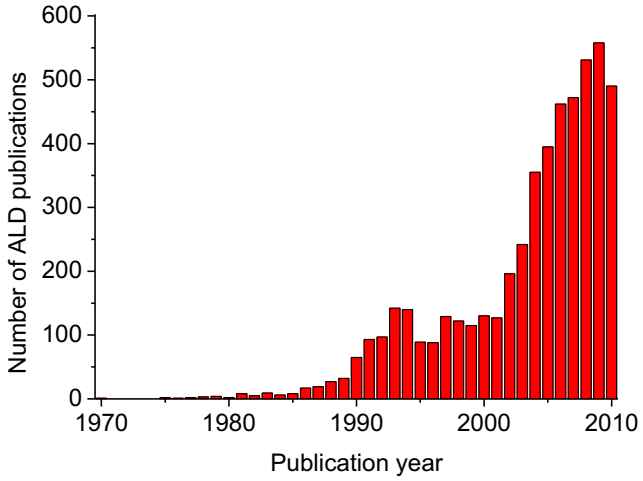

Figure 2.6: Number of ALD publications per year.

Figure 2.7 illustrates the number of publications on PE ALD[8]. Since 2004, PE ALD is good for about 8 % of all ALD papers.

[7] Search made on October 10, 2010. ALD has been known under a number of names, with ALD being the most popular. The search was performed for the same criteria as [275]: "atomic layer deposition", "atomic layer epitaxy", "molecular stratification", "molecular layering", "molecular layer epitaxy", "molecular lamination" or "atomic layer chemical vapo*r deposition"

[8] Search made on October 10, 2010. Searched with "plasma enhanced ald", "plasma enhanced atomic layer deposition", "plasma assisted ald", "plasma assisted atomic layer deposition", "radical enhanced ald", "radical enhanced atomic layer deposition", "plasma ald", "plasma atomic layer deposition" or ("radical enhanced chemical vapor deposition" and "atomic layer epitaxy"), excluding publications where ALD is a medical term.

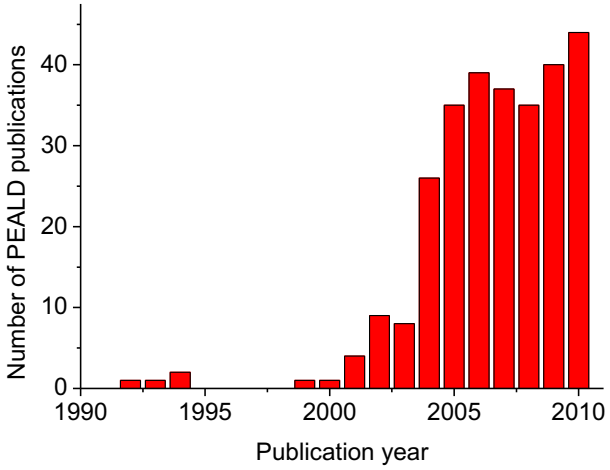

Figure 2.7: Number of PE ALD publications per year.

Figure 2.8 shows which films had been deposited by ALD in 2005. It is clear that ALD processes already exist for depositing a wide variety of elements and compounds[9]. In addition to binary compounds, more complex ones (e. g. hydroxyapatite [270] and $La_{1-x}Ca_xMnO_3$ [233]) have been reported. Furthermore, new precursors are being developed to deposit new elements (e. g. silver [35]), compounds (e. g. $Ge_2Sb_2Te_5$ [295]) or to have better behaved ALD - ideal saturation, higher GPC, lower deposition temperature or faster nucleation - compared to existing processes (e. g. for the deposition of TaN [292]).

[9]Fluorides and chlorides have also been grown [361], but are not included in figure 2.8

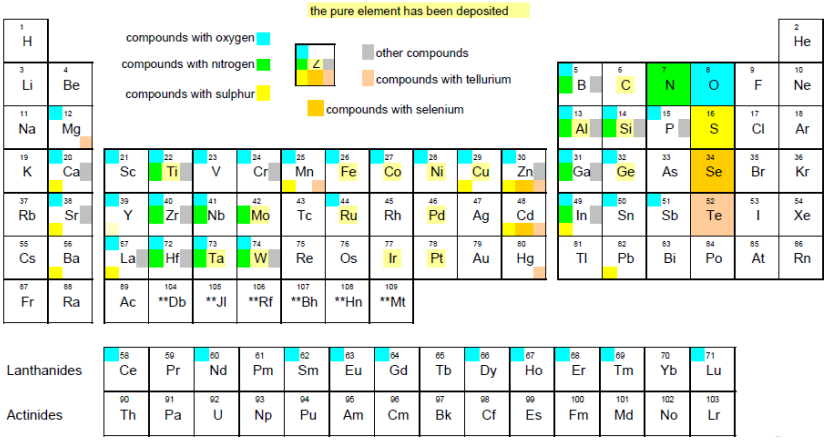

Figure 2.8: Review of elements deposited by ALD as of 2005. Taken from [275].

3
Applications of ALD

This chapter gives a bird's eye view on ALD applications published in the scientific literature. Some of the ALD enabled products have already been commercialized, while others are still in the laboratory phase. However, I hope it will help the reader to appreciate the practical side of ALD, a true nanotechnology at the interface of materials science, semiconductor technology, optics, heterogeneous catalysis, biology and many more fields.

3.1 Microelectronics

Electronic devices are pervasive in consumer products like TVs, digital cameras, GPS, cell phones and even cars. These devices work by electronic components connected together in circuits.

The signal processing of integrated circuits (ICs, chips) relies on transistors, which act like on-off switches for currents. Transistors were invented in 1947 at Bell labs. They quickly replaced the large, power hungry and unreliable vacuum tubes used in the first electric computers. After a series of innovations in transistor design and manufacturing, by 1960 it became possible to make an entire circuit on a single piece of silicon. Hence the name integrated circuit. Advances in lithography enabled the continuous miniaturization described by 'Moore's law': the density of transistors on the most advanced chips doubles every 18 to 24 months. This miniaturization however has physical limits. It is illustrated below how ALD pushes the end to Moore's law farther in the future.

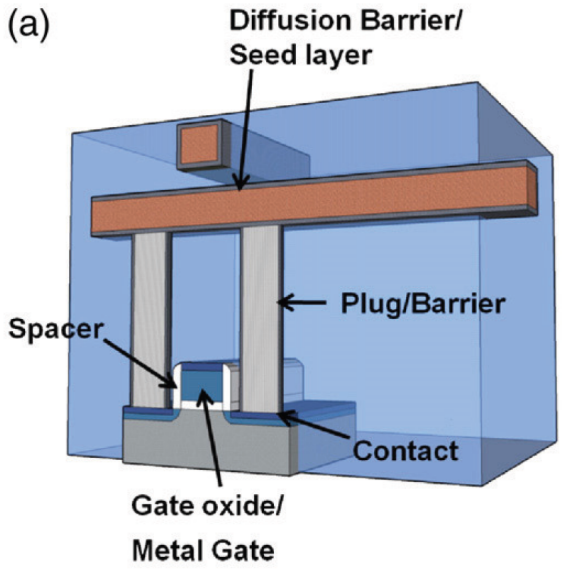

Figure 3.1: Schematic drawing of a MOSFET transistor and interconnects. Taken from [152].

3.1.1 High-k oxides

Silicon dioxide (SiO_2) has been the gate dielectric in silicon metal oxide semiconductor field effect transistors (MOSFET) (figure 3.1) for nearly half a century [291]. Although silicon dioxide is a good electric insulator, charge tunnels through it when it is scaled into a very thin gate oxide. This current causes unwanted power dissipation, even when the transistor is not switching. The tunnel current can be reduced by increasing the physical thickness of the oxide layer. To obtain the same field effect, SiO_2 should be replaced by an insulator with a high dielectric constant (a 'high k')[1]. Because of the high demands on thickness control and film uniformity over the wafer on which transistors are grown, ALD is a suitable method to grow the high-k oxide. Indeed, Intel shipped devices with hafnium oxide based gates in 2005 [25]. This was a large step for an industry which has extreme demands on manufacturing reliability, and where new materials and deposition techniques are only adopted when absolutely necessary [301].

Other than chips for logic, there are also memory chips. One way to store data on a chip is dynamic random access memory (DRAM). An electric charge on a capacitor represents one bit of information. The capacitance depends on the geometry of the capacitor, and on the thickness and dielectric constant of its di-

[1] A review of all requirements for MOSFET gate oxides can be found in [296].

electric. The capacitors should not consume too much area (sometimes dubbed 'real estate') on the silicon surface. The surface density can be increased by making the metal-insulator-metal capacitors (MIMCaps) in holes or 'vias' rather than as flat devices on the Si. 3D capacitors combine a large electrode area with a small footprint on the silicon surface. The leakage current through the high-k oxide should be very low and the processing temperature of the material must stay below 650°C [167]. One interesting material for the high k of MIMCaps is strontium titanate ($SrTiO_3$), which has a k-value of more than 100. Because of the high aspect ratio (ratio of depth and opening diameter) of the vias in which MIMCaps are deposited, ALD is an attractive deposition technique.

3.1.2 Copper diffusion barrier

Transistors are connected by low resistivity copper lines. Cu reduces the signal delay time between transistors compared to the Al lines that were used before. Furthermore, Cu is less susceptible to electromigration than Al [147]. However, using copper results in a problem: Cu easily diffuses into silicon and silicon oxide. To prevent the Cu from spreading into its environment, a diffusion barrier has to encapsulate it (see also Chapter 9). Cu barriers are usually refractory metal nitrides, such as TaN and TiN [299].

The resistivity of the diffusion barriers is higher than that of Cu. Therefore, the thickness of the barrier should be kept to a minimum.

Because it is difficult to etch copper, the interconnects are deposited by the dual damascene process. After copper is electroplated in trenches, the surface above the pattern is removed by chemical mechanical planarization (CMP) [7]. As a result, the copper diffusion barrier must be conformally applied to the bottom and walls of the trenches (figure 3.2).

So the diffusion barriers need to be (a) very thin and (b) conformal. This explains the interest in ALD Cu diffusion barriers.

3.1.3 Metals for electrodes or plating

Copper diffusion barriers like TiN or TaN are usually not conductive enough for direct electroplating of Cu interconnects in dual damascene (see previous section). A conductive seed layer of Ru or Cu has to be grown on the diffusion barrier first (see figure 3.2) [147] [150]. Again, because deposition is needed in trenches and a good control is needed over thickness, ALD offers an interesting alternative to traditional deposition methods.

Polycrystalline silicon, traditionally used as the gate electrode, reacts with high-k oxides like HfO_2 [296]. Therefore, it has to be replaced by a metal that is stable when contacted to the oxide. The metal contacts have the further advantage of being more conductive than poly-silicon.

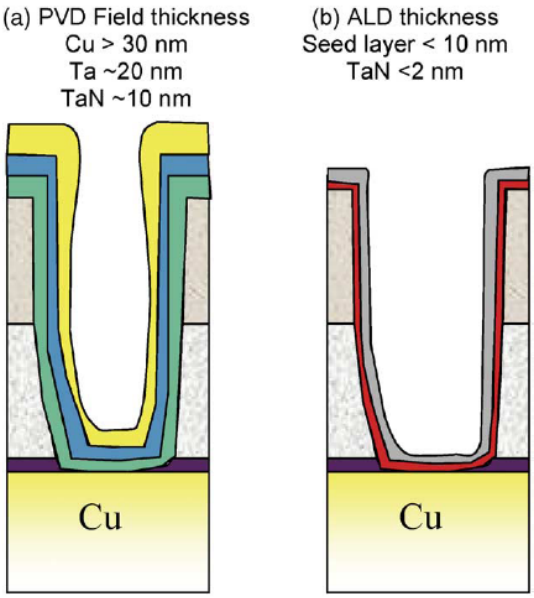

Figure 3.2: Comparison of PVD and ALD Cu diffusion barriers. Taken from [150].

For DRAM, high work function metals like Pt, Ru, Ni or TiN (a conductive nitride, see chapter 9) should be used as electrodes to achieve low leakage currents [167].

3.1.4 Beyond silicon

Semiconductors such as germanium or gallium arsenide have higher carrier (electron or hole) mobilities than silicon. A high mobility is preferred for processing high frequency signals (e. g. for telecom applications) and also for power transistors. Unfortunately, the chemistry of these materials is harder to handle than that of silicon where silicon dioxide forms a stable passivating layer. A number of recent papers have shown how ALD can be used to grow high k dielectrics on Ge with low trap density at the interface [49] [356]. It has also been reported that GaAs was successfully passivated prior to ALD of the gate oxide [369]. These are promising developments for enabling CMOS scaling on high mobility substrates.

Another research direction is carbon electronics, based on carbon nanotubes (CNTs) or graphene. Graphene is a monolayer of crystalline hexagonal carbon, a single slice of graphite. Novoselov and Geim discovered a method to make graphene in 2004 [240], and were awarded the 2010 Nobel Prize in Physics for their work. Graphene has several scientifically interesting properties. For example,

its charge carriers behave as relativistic particles [241]. Furthermore, by applying a gate voltage to films composed of a few graphene monolayers [240], a high density of carriers with a large room temperature mobility can be induced. This finding has generated a lot of enthusiasm to make graphene relevant for the semiconductor industry. With the goal of making field effect devices, high k oxides have been deposited on few-layer graphene [357] [340]. Because graphene lacks dangling bonds that act as nucleation sites, ALD films only grow on the step edges between two graphene layers ('terraces'). Nanoribbons are formed along the step edges. Remarkably, the ALD film grows much faster in the lateral direction than it does perpendicular to the surface [357]. Continuous oxides can be grown by covering the graphene with strongly physisorbed TMA and NO_2 [357]. These molecules then offer nucleation sites for the high k dielectric. The same method has to be applied to enable ALD on CNTs due to their inertness [33]. ALD is also very well suited for conformal coating of other nanowires. Kim et al. recently reviewed the literature on ALD for nanodevices [152].

In summary, the semiconductor industry is constantly innovating to develop faster, smaller devices while minimizing power consumption. To continue this trend, new materials need to be grown on three dimensional substrates. This has led to an evolution in deposition techniques from PVD to CVD to ALD [301]. ALD can meet the stringent demands of thickness control, conformality and process reliability, even as wafer diameters increase to 450 mm.

3.2 Protective coating

Coatings are deposited on a wide range of objects to protect the substrate from its environment or to enhance its functionality. For example, steel is coated with zinc to avoid corrosion, the painting of the hull of ships prevents biofouling (growth of marine organisms, which enhances drag and hence fuel consumption) and hard coatings are deposited on metal working tools. The use of ALD films as protection against moisture, wear or corrosion is illustrated here.

3.2.1 Gas diffusion barriers

Quite a number of papers have been published describing ALD moisture barrier layers. For example, organic light emitting diodes (OLEDs) have a very limited lifetime when subject to water vapor. By covering them with a 50 nm thick ALD film, the water vapor transmission rate (WVTR) has been reduced almost a thousandfold [249] [90]. The transparent films are pinhole free, which explains their good performance[2]. Replacing the simple ALD film with a nanolaminate can fur-

[2]The residual diffusion can be explained by H diffusion through the oxide film, which recombines with OH surface groups at the other side of the barrier [46].

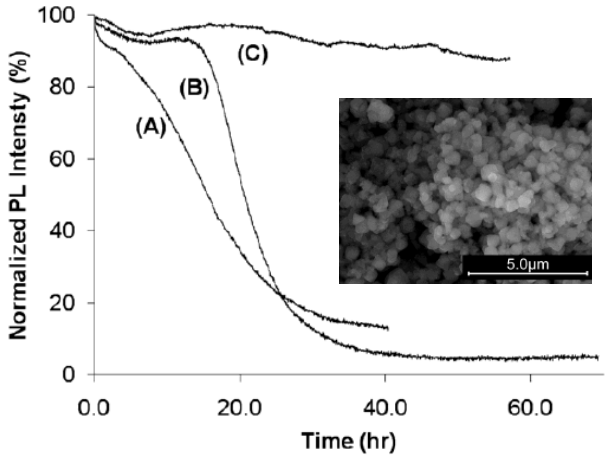

Figure 3.3: Normalized PL intensity of CaS:Eu particles (a) without ALD film, (b) with 10 nm Al_2O_3 and (c) 20 nm Al_2O_3. Inset shows SEM picture of the coated CaS:Eu particles. Adapted from [10].

ther reduce the WVTR [217]. Similarly, organic solar cells were encapsulated to prevent degradation by water vapor [260].

The group of Steven George has reported ALD on different polymers [348] [95] [96] [46] with the goal of making diffusion barriers. The flexible substrate can result in cracks in the inorganic ALD film [368]. Plasma enhanced ALD on polymers was done by Langereis et al. [184].

Hirvikorpi et al. have investigated the barrier properties of ALD alumina on polymer coated board, used for food packaging [111] [112]. They showed that the water and oxygen transmission rates improved significantly compared to uncoated substrates. Furthermore, ALD barriers outperformed those grown with a sol-gel technique or PVD [112]. Groner et al. have even shown that ALD on PET bottles can reduce the loss of CO_2, enabling a longer shelf life of soda drinks [95]. Beneq has commercialized a process to coat silver objects like coins and jewels with transparent alumina ALD to prevent them from tarnishing due to airborne sulfur. Hence, the silver keeps shining [268].

In a collaboration with the Lumilab research group at our department, ALD protection of photoluminescent (PL) phosphors was studied [10]. Water sensitive calcium sulfide particles doped with europium were coated with thermal ALD (TMA + H_2O). Although the deposition process used water as reactive gas, the particles were not significantly degraded by it. Figure 3.3 shows that a 20 nm thick alumina proved to be a good water diffusion barrier. The thin ALD films are much more transparent than the sol-gel alternative water barrier.

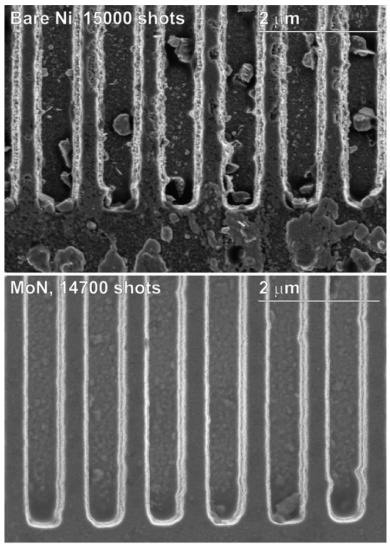

Figure 3.4: Comparison of a bare Ni mold, and a mold coated with ALD MoN after 15000 and 14700 injection molding shots, respectively. The coated mold is cleaner, resulting in better features after many cycles. Figure taken from [218].

3.2.2 Wear or corrosion resistant coatings

Plastic parts with (sub) micrometer textures can be produced by micro-injection molding [218]. A molten polymer is shaped by injecting it into a cooler mold. During production runs, the mold is gradually contaminated by the polymer. The mold shape deteriorates, and the features on later produced plastic parts are less sharp (figure 3.4). In an effort to reduce this deterioration, Miikkulainen and coworkers compared untreated nickel molds with molds coated with ALD molybdenum nitride. They found that the MoN was conformal, smooth and well adhered to the Ni mold. The SEM figure of a bare and a MoN coated Ni mold shows that the coated mold is less contaminated. So the ALD coating is a promising method to reduce maintenance costs in micro-injection molding.

In addition, tribological testing demonstrated that the nitride adhered well to the substrate. For polycarbonate injection molding, the coefficient of friction of the coated mold was lower (0.68 ± 0.01) than that of the bare Ni (0.81 ± 0.07).

Wear resistant ALD coatings (ZrO_2, TiO_2) have also been shown to reduce friction on micro electromechanical structures (MEMS) [237].

The pinhole free films grown by ALD also enable the protection of steels from corrosion. For example, the corrosion current of stainless steel (SS) covered with 50 nm ALD TiO_2 in a NaCl solution was more than 10 times lower than for bare stainless steel [316]. Wear and corrosion resistant bilayers of TiO_2 (ALD)/CrN

(PVD) [315] and Al_2O_3 (ALD)/TiAlN (PVD) [212] on SS also improved corrosion resistance compared to samples without the ALD films. It should be realized that traditional PVD corrosion barriers are several micrometers thick, compared to the nanometer scale ALD films. ALD alumina was further shown to improve the corrosion resistance of steel fibers against H_2SO_4 and thermal oxidation [142]. Carbon fibers were protected against oxidation by an ALD alumina coating [303], as were polymers [44].

3.3 Optics

This section considers applications of ALD for the generation, manipulation and capture of light.

3.3.1 Electroluminescent displays

Zinc sulfide based thin film electroluminescent (TFEL) displays were the first industrial application of ALD, in production since 1983 [194] [268]. The combination of yellow light emitting ZnS:Mn^{2+} (manganese doped ZnS) with SrS:Ce^{3+} (blue-green) for a broadband light emission was already achieved in the 1990s [229]. By applying appropriate filters, all colors can be achieved by such a display. Other ALD phosphors are CaS:Pb [363] and BaS and SrS doped with Cu, Ce, Pb, Mn and Eu [127].

3.3.2 Optical components

Photonic crystals are materials with a periodically modulated dielectric constant. As a result, they alter the dispersion properties of light. This modulation results in optical bandgaps: wavelengths at which light cannot propagate through the photonic crystal. These bandgaps are optic analogues to the energy bands of semiconductors. In this manner, devices like all-optical switches or lossless waveguides could be constructed. In order to control the periodic modulation of the refractory index (dielectric constant), photonic crystals made from stacked spheres have been coated with materials with another dielectric constant. Figure 3.5 shows an opal photonic crystal, consisting of silica spheres. It is clear that only a highly conformal deposition method like ALD can achieve uniformal coating of all spheres. This is the reason a number of groups have investigated ALD on photonic crystals [166] [313] [262].

The reflectance of a photonic crystal as a function of wavelength changes for different ALD coating thicknesses (figure 3.6).

Other optical devices like arrays of nanolenses [339], antireflection coatings [326] [120], waveguides [9], color filter arrays [83] and erbium doped optical fibers [238] have been made by ALD.

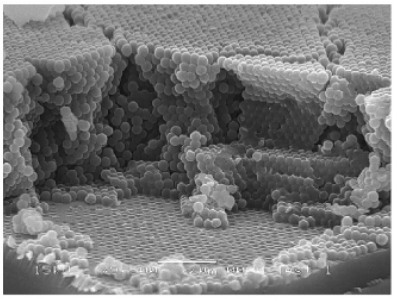

Figure 3.5: SEM of cleaved photonic crystal, coated with ALD VO_2. Taken from [262].

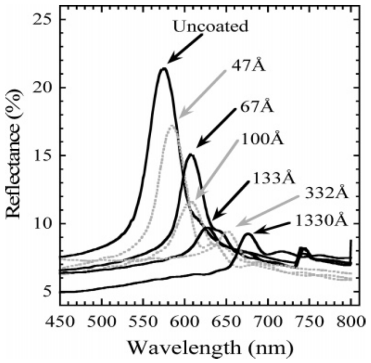

Figure 3.6: Reflectance as a function of wavelength of photonic crystals coated with ALD alumina. Taken from [313].

3.3.3 X-ray optics

Due to their short wavelengths, X-rays are interesting to image nanometer scale objects, e. g. nanomagnetic structures [336]. However, this radiation cannot be controlled by conventional lenses. In order to make X-ray microscopes, they have to be focused in other ways. ALD made Fresnel zone plate lenses which focus X-rays by diffraction have been reported [130]. These 'lenses' consist of a periodic arrangement of materials with a high (Ir) and low (Si) refractive index. Iridium was grown on the walls of the silicon template. A resolution of 15 nm was achieved for 1 keV X-rays. The ALD made Fresnel zone lenses require only a single lithography step. It could replace other methods, which suffer from low fabrication yields and require complicated alignment.

The same idea of combining a high and low refractive material was used by Fabreguette and George to make X-ray mirrors [70][3]. They fabricated a laminate of nanometer scale alumina and tungsten ALD films on a flexible Kapton substrate. The structure had a reflectivity of 78% for copper radiation (λ = 1.54 $\mathring{A}$). This is very high, considering that Kapton is transparent for X-rays. Because the substrate is flexible, the shape of the X-ray mirror can be adapted during use. The flexible and light-weight X-ray mirrors could enable space borne X-ray observatories [70].

3.3.4 Photovoltaic applications

In solar cells, photons produce electron-hole pairs. These pairs are separated by internal electric fields in the photovoltaic (PV) cell, and result in a voltage at the electrodes. Relatively efficient solar cells can be produced from crystalline silicon (c-Si). Because c-Si is expensive, thin wafers are necessary. Recombination of the electron-hole pairs however, especially at the surface of these thin wafers, reduces the cell's efficiency. Alumina coatings grown with thermal and plasma enhanced ALD passivate the cell better than silicon nitride (SiN_x) and amorphous silicon (a-Si) [114]. The passivating effect has been attributed to the built-in negative space charge in the alumina layer [113] [6]. Alumina deposited by thermal ALD has been shown to reduce the surface recombination velocity more than PECVD or reactive sputter deposited alumina [311].

Some radically different PV designs are not based on silicon. One promising alternative to Si are thin films made of copper indium gallium selenide (CIGS). These films need buffer layers to stabilize the PV structure. The buffer improves charge collection and reduces recombination. Usually the buffer layer is CdSe, which containes the toxic element cadmium. $Cd_xZn_{x-1}S$ [16] and Cd free buffer layers [334] have been grown by ALD.

[3] Less efficient X-ray mirrors had been made by ALE a decade earlier [128].

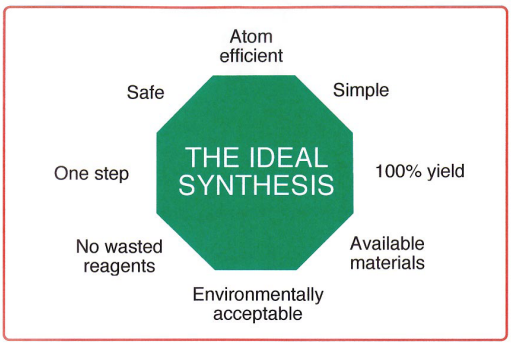

Figure 3.7: Catalysts are used to approach the ideal synthesis: a simple, safe process from cheap reagents which does not generate waste. Taken from [42].

3.4 Catalysis and energy storage

3.4.1 Catalysis

Catalysts are materials which influence the reaction rate of a chemical reaction, without being consumed in the process. They are used to lower energy barriers, enhance selectivity for a certain reaction product, or increase the reaction rate. This shortens process time and lowers energy costs and waste. Catalysts are an important element in the quest for the ideal synthesis of chemicals, shown in figure 3.7.

Over 90 percent of all industrial chemical products involve a catalyst in some production step [312]. For example, petroleum refineries use zeolite (nanoporous silica-alumina materials) catalysts to crack hydrocarbons with long chains into shorter chains. Noble metal catalysts are used in vehicles to reduce the emission of NO_x and other harmful gases.

Heterogeneous catalysts are solids, while their reaction products are gases or liquids. This makes it easy to separate them. A good catalyst is stable, has well dispersed active sites and a large surface area per mass.

One or multiple ALD cycles can grow catalytic sites on a high surface area support. Chemists might be more familiar with the term grafting, which describes the same phenomenon: a self-limiting surface reaction results in the chemisorption of functional groups at the support.

Table 3.1 shows a selected number of supported metal (oxide) catalysts made by ALD (ALE in older publications [105]) and the test reactions for these catalysts. More examples can be found in Table 2.1 in the Ph. D. thesis of Puurunen [271].

A number of papers studied the catalytic activity in depth. Keränen et al. [144] showed that the acidic character of a titania/silica support was significantly en-

catalyst/support	reaction	reference
CoO_x/SiO_2	hydrogenation of toluene	[11] [12]
TaO_x/(SiO_2 or Al_2O_3 or ZrO_2)	oxidation of methane	[18]
AlO_x/zeolite	cracking	[328]
Cr/AlN/Al_2O_3	dehydrogenation of isobutane	[273]
FeO_x/ZrO_2	(reduction of sulfates or use in SOFC[a])	[335]
Ti-O-Si$(CH_3)_2/SiO_2$	epoxidation of EBHP to PO and MPC[b]	[27]
TiO_2[c]/SiO_2	photocatalytic degradation of salicylic acid	[338]
WO_x/SiO_2[d]	2-butanol dehydration	[110]
WO_x/SiO_2[d] and VO_x/SiO_2[d]	partial oxidation of ethanol	[110]
VO_x/Al_2O_3[e]	oxidative dehydrogenation of cyclohexane	[73]
VO_x/SiO_2 and VO_x/Al_2O_3	dehydrogenation of propane	[143]
Ru[f]/Al_2O_3/C[g]	(Haber-Bosch synthesis of ammonia)	[24]
Ir[f]/(Al_2O_3 or $SiAlO_x$)	hydrogenation of toluene	[321]
Pt[f]/SiO_2	oxidation of CO	[198]

Table 3.1: List of ALD made catalysts and tested reactions. Reactions between brackets were proposed by the authors of the papers, but not performed. (a) SOFC: solid oxide fuel cell, (b) EBHP: ethyl benzene hydroperoxide; PO: propylene oxide; MPC: methyl phenyl carbinol, (c) titania film, (d) MCM-41 and SBA-15, (e) AAO, (f) noble metal nanoparticles, (g) aerogel, (h) mesoporous gel.

hanced by ALD of V_2O_5. The vanadia species were highly dispersed. The number and relative strength of the ALD vanadia was higher than for impregnated vanadia.

Stair and coworkers from Argonne National Laboratory have published a series of papers [253] [329] [73] on their effort to make catalysts in anodized alumina (AAO). The center of an aluminum disk was anodized, resulting in a membrane with long parallel mesopores. This structure with its deep, hexagonally spaced pores was dubbed a 'nanolith', analogous to the monoliths in catalytic converters. The aluminum ring makes a good support, and the structure was placed in a VCR fitting to make a small reactor.

Besides loading supports with catalytically active species, ALD has also been used to modify the support. For example, porous oxides were covered with aluminum nitride [272]. This was done because the combination of the catalytic site and its substrate determine the catalytic activity.

3.4.2 Batteries, fuel cells and capacitors

Batteries and fuel cells are electrochemical cells which convert chemical energy into an electric current by redox (reduction-oxidation) reactions. The anode and cathode are separated by an electrolyte. This electrolyte conducts ions but not electrons. The electrons move through an external circuit where the current can do useful work.

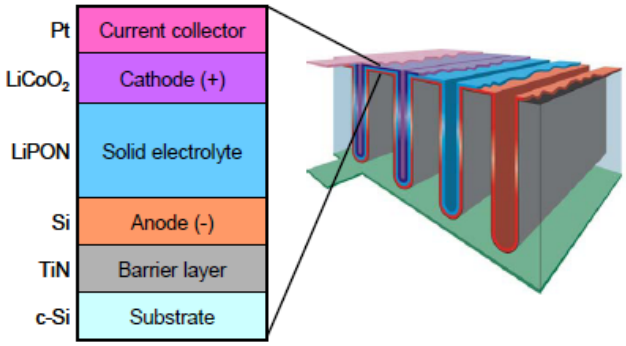

Figure 3.8: Proposed all solid state battery on chip. Taken from [173].

In lithium ion batteries, the chemical energy is stored in the electrodes. Lithium ions are intercalated in oxides of cobalt, nickel or manganese because these transition metals can easily change their oxidation number. The reactants for fuel cells, e. g. H_2 and O_2, are stored externally. Batteries and fuel cells are critical for applications like portable electronic devices, the storage of non-continous renewable energy[4] and for electric vehicles.

Electrodes composed of nanoparticles have a high surface area per mass. The high surface area is needed in order to achieve large charge and discharge currents in lithium ion batteries [138] [134]. When a battery discharges however, the electrodes undergo chemical and physical changes. One problem is that the transition metal ions can dissolve into the electrolyte. This degrades the performance of the battery. Coating the nanoparticles with an ALD film of Al_2O_3 can block this loss of transition metal ions, while Li can still diffuse through it [138].

Notten et al. are developing all solid state 3D batteries on chips (figure 3.8), for future wireless devices [239] [173]. Evidently, the Li ions should not contaminate the silicon substrate. Therefore, TiN diffusion barriers were grown with ALD [173]. Pt was deposited as charge collecting electrode [173]. Furthermore, ALD processes are being developed to grow Li containing materials [269].

Solid oxide fuel cells (SOFCs) work at high temperatures. This has the advantage that multiple reactants (other than H_2) can be used. Oxygen is conducted through solid electrolytes which work best at these high temperatures. ALD of such electrolyte materials like yttria stabilized zirconia [317] and yttrium doped CeO_2 [17] and $BaZrO_3$ [319] have been reported by Prinz et al., as well as $La_xSr_{1-x}MnO_3$ electrodes. Platinum [132] and Ru/Pt alloy [318] catalysts which enhance redox reactions in fuel cells have also been obtained by ALD.

Capacitors offer a physical method to store energy. We already encountered

[4] Like solar or wind energy

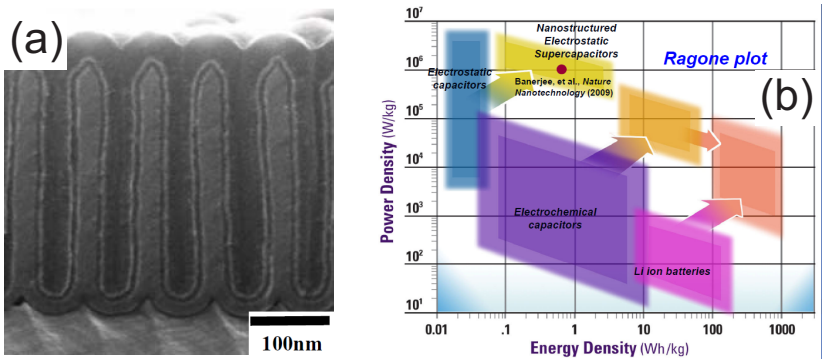

Figure 3.9: MIM capacitors in AAO (a) and comparison of the tradeoff between energy density and power density for different energy storage technologies (b). Taken from [20] (a) and [304] (b).

ALD capacitors for DRAM (see section 3.1). Rubloff and coworkers have made metal-insulator-metal (MIM) capacitors in AAO (figure 3.9(a)). The TiN electrodes and Al_2O_3 dielectric were grown with ALD [19]. Unlike DRAM structures which need lithography and etching, the AAO is self-assembled. This results in a cheap, yet highly reliable method to make supercapacitors. The supercapacitors combine a large energy density with a high power density per mass. In comparison, electrochemical devices have a smaller power density (figure 3.9(b)).

3.5 Biological materials

ALD has been demonstrated on a number of biological materials. Either the substrates are synthesized by biological organisms, or else the film is deposited to change the interaction of the substrate with certain cells.

3.5.1 Templates

Nature produces many 'nanostructures' with complex shapes. The tobacco mozaic virus (TMZ) consists of proteins which form a hollow tube with a diameter of 18 nm and a length of 300 nm around its RNA. Knez and coworkers have demonstrated that metallorganic tubes can be made by coating the TMV with ALD [170] [171].

The wings of certain butterflies behave as natural photonic crystals which produce their colors. Butterfly wings have been used as templates to duplicate their shape [175] [84]. The compound eye of a fly has also been used as a natural template [120]. ALD alumina was used to change the anti-wetting property of butterfly

wings and water strider legs [55].

Lee et al. have atomic layer deposited TiO_2 and ZnO on egg shell membranes [191]. When these coatings were irradiated by UV light, photocatalytic breakdown of Escherichia coli bacteria was demonstrated[5]. Furthermore, the mechanical stability of the dried collagen membranes was found to be improved after ALD of Al_2O_3, TiO_2 or ZnO, because of metal infiltration in the structure [193].

The same group has also done ALD on spider silk [192]. The toughness of the fibers was significantly increased by the ALD. The authors attributed this behavior to the replacement of hydrogen bonds in the silk proteins by covalent bonds.

None of these examples has an immediate application, but they do illustrate several advantages of ALD such as conformal coating and low deposition temperatures.

3.5.2 Biocompatibility

Growth of specific cell types on implants is necessary.

Hyde et al. have coated cellulose fiber substrates with titanium oxynitride using ALD in order to enhance their biocompatibility [124]. Various thicknesses were tried to optimize the adhesion of human adipose-derived adult stem cells (hADSC).

Hydroxyapatite is a calcium phosphate compound which resembles bone tissue. Mouse MC3T3-E1 cells were shown to adhere better to annealed (crystallized) ALD hydroxyapatite than on as-deposited amorphous hydroxyapatite films [270]. Another biocompatible ALD coating was presented in [201].

3.6 And many more...

The above list of applications of atomic layer deposition is far from complete. Several other potential applications have been reported in literature.

George and Weimer at the University of Colorado have explored a range of applications for ALD on **powders**.

- Varistors (resistors where the resistance depends on the voltage over them) were produced from particles coated with an ALD film [346].
- ALD SnO_2 on Al nanoparticles produced a thermite with a very fast reaction velocity [76]. Thermites are powders where a fuel and oxidizer are in close contact. Upon reaction, they release a large amount of energy per volume.
- The photoactivity of UV blocking TiO_2 particles was reduced by coating them with alumina [165].

[5] UV light on ALD TiO_2 was also shown to result in photocatalytic breakdown of Deinococcus geothermalis bacteria biofilm [287].

A variety of **sensors** has been demonstrated in literature.

- Pores through which DNA is passed for sequencing have been modified with ALD [39].
- A microresonator 'bridge' structure was grown with Al_2O_3 [38]. Such resonators can be used as mass or pressure sensors.
- SnO_2 based gas sensors have been reported, both as thin films [298] [60] and as nanotubes [162].
- Gold nanoparticles were covered with an alumina film to improve Raman spectroscopy [199].
- Secondary electron emissive layers for microchannel plates (used in night vision goggles) were grown with ALD [21].

ALD has been done on **fibers** for a number of reasons (more examples in chapter 11).

- The wettability of cotton can be engineered by a thin alumina coating [123]
- Hollow tubes can be made by using a fiber as template and then removing it [286] [254].

Some unrelated technologies incorporating ALD films are given below.

- ALD has replaced reactive sputtering to grow the alumina coating on read-write heads in hard drives [246].
- High temperature superconductor films and their buffer layers have been deposited [359] [252].
- W/Al_2O_3 nanolaminates have proved to be good thermal barriers, but unfortunately these nanolaminates are unstable at high temperatures [45].
- Ultrathin $Ge_2Sb_2Te_5$ phase change memory layers were developed by the University of Helsinki and IBM [295] [196].
- Glass was reinforced by filling the microcracks in its surface with ALD [267].

Undoubtedly, the list of ALD applications will continue to expand in the coming years.

4 ALD reactors

To have an ALD process, all that is required is that the precursor and reactive gas are separated in the gas phase and that they react at consecutive steps with the substrate surface. Depending on the application, a different reactor design could be preferred. Several companies offer ALD reactors, mainly for the semiconductor industry (see Appendix A).

4.1 Precursor, pressure and throughput

4.1.1 Reactant delivery and flow

In our reactors (see chapter 5), all of the precursor is heated in a bubbler and delivered by opening a valve. For thermally unstable precursors, the reactant is best stored cold, and only heated prior to entering the chamber. This can be accomplished with liquid injection systems. The fraction that is injected is vaporized just before entering the reaction chamber [342] [161]. Solid precursors can be dissolved in a solvent. Liquid injection also has the advantage that the amount of precursor can be controlled more accurately.

Figure 4.1 shows the motion of reactants (and carrier gas) for two frequently used ALD systems in literature. In a flow over configuration, reactants enter the reactor at one side, pass over the substrate and are pumped at the opposite side. The volume of the reactor is minimized. However, the film thickness on substrates coated with this reactor design is sometimes not uniform. Some reactants, like ozone, can break down by wall collisions. This leads to a lower ozone concentra-

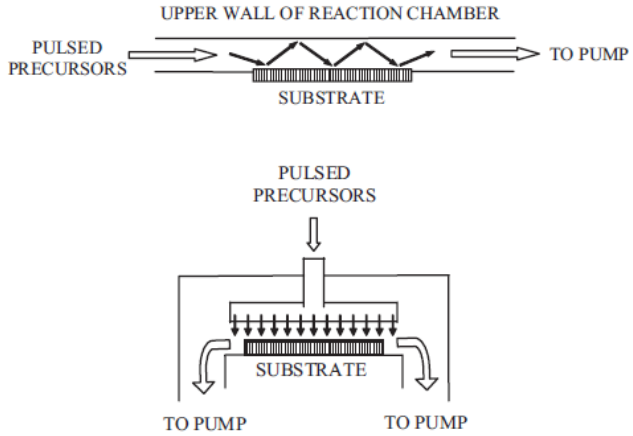

Figure 4.1: Flow over reactor (top) and showerhead precursor delivery system (bottom). Taken from [294].

tion at the end of the reactor. Another possible complication is when HCl is formed and desorbs during ALD. The acid etches the film downstream of the reaction. As a result, there is a thickness gradient along the flow direction.

Such non-uniformity due to non-ideal ALD is avoided when reactants are delivered through a showerhead (figure 4.1 (bottom)). This configuration is standard for CVD, where a homogeneous flux to the substrate is crucial.

4.1.2 Working pressure

Three pressure ranges for ALD have been reported. Advantages, disadvantages and the possibility to use a plasma are briefly considered.

A first pressure regime is in the order of 10^{-3} mbar (0.1 Pa). A high vacuum pump (usually a turbomolecular pump) is needed to reach this pressure. Reactors working in this regime usually have a load lock to load the substrate. The reactor can then be kept vacuum at all times, because it takes a while to reach the needed vacuum level. At this low pressure, inductively coupled plasmas (see figure in plasma section) can be ignited.

According to literature [87], ALD at medium pressure is used most frequently. This corresponds to pressures in the order of 1 mbar = 100 Pa. The precursor is introduced in the viscous flow [62] of a continuously flowing inert carrier gas such as nitrogen. The carrier gas flows from the inlet to the pump, dragging the precursor with it. When no precursor is in the carrier gas, it purges reaction products and unreacted precursor from the reactor. This type of reactor still allows the use of plasma, mostly indirectly (radical enhanced).

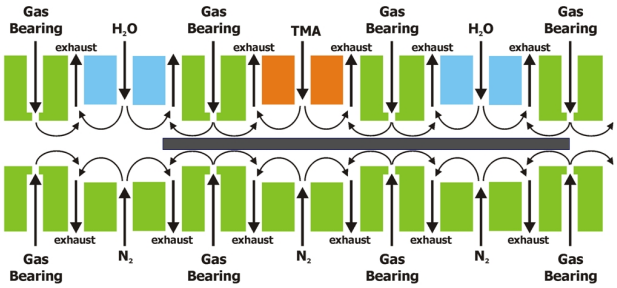

Figure 4.2: 'Spatial' ALD concept for high throughput. Courtesy of Solaytec [325].

A promising method that does not need high vacuum pumps is atmospheric pressure ALD, working at 1 bar (100 000 Pa). When precursors are used that do not react with O_2, dry air can be used as a carrier gas in open air ALD. In principle, corona discharges can generate oxygen plasma at atmospheric pressure. Because of the very short mean free path of molecules at atmospheric pressure, a moving inert gas like N_2 can separate cells with different ALD precursors/reactive gases. Since the diffusion time to cross the N_2 separation is much longer than the time it takes to refresh the purge gas, there is no risk of unwanted CVD reactions caused by overlapping precursor and gas. The reactor of Levy et al. [197], as well as the reactor of Solaytec (figure 4.2) are based on this concept. The shielding effect of a flowing inert gas is also used in TIG (tungsten inert gas) welding, preventing the weld from oxidizing during the process.

4.1.3 Throughput and process time

In our research reactor, we use a *job process*: deposition is done on one (piece of) wafer at a time and the substrate has to be unloaded afterwards. Industrial reactors are typically designed to maximize the total throughput, while maintaining film quality. One way to increase throughput is by doing ALD in a *batch process*, where multiple substrates are loaded in the reactor during one deposition run. Other factors taken into account in the reactor design include minimizing the consumption of (expensive) precursors, avoiding downtime for maintenance, satisfying the need for a small footprint in clean rooms and ease of integration in the production line.

Two Dutch companies (Solaytec and Levitech, see also [259]) have commercialized high-throughput reactors that can perform ALD on up to 3000 wafers per hour. Such volumes are needed to make ALD on photovoltaic cells commercially viable. The wafers pass cells with the different reactants that are separated by an inert gas. Kodak [197] has developed a comparable system. These systems enable

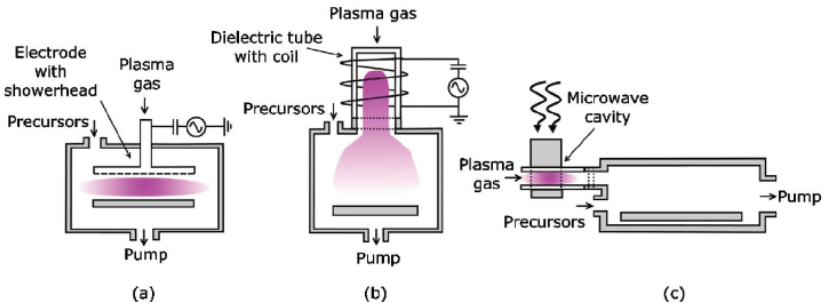

Figure 4.3: Direct plasma (a), remote plasma (b) and radical enhanced (c) ALD reactors. Taken from [108].

continuous ALD processing. No stacks of substrates waiting for deposition pile up at the factory, as is the case in batch processes. On top of the smoother workflow and flexibility, there is no risk of losing an entire batch when the deposition process fails. An ALD web coater for roll to roll processing is being developed, enabling the continuous growth of thin films on flexible plastic foils [31].

4.2 Plasma sources

Figure 4.3 illustrates three types of plasma sources for PE ALD at low pressures. A first design is a modification of a traditional system for reactive ion etching (RIE). An RF generator powers an electrode, while the substrate acts as the counter electrode. This configuration is called the 'direct plasma', because the substrate is exposed to high energy ions. The bombardment of the substrate by accelerated ions can lead to sputtering of the deposited film, and electric defects. A second plasma source has no electrodes contacting the plasma. A coil attached to a radio frequent (RF) generator surrounds a glass or quartz tube. When a low pressure gas is present in the tube, the RF field of the antenna coil generates an inductively coupled plasma (ICP) discharge. The amount of charged particles that reach the substrate is small. This configuration is known as a remote plasma system. Finally, there is 'radical enhanced' or 'radical assisted' ALD. A plasma is excited in the flowing reactive gas, outside of the reactor. Although the picture shows a microwave plasma source, RF sources have also been used. Ions and electrons recombine before they enter the ALD chamber. Radicals have longer lifetimes and they can reach the substrate, hence the name of the setup. Radical enhanced ALD has the advantage that the substrate or growing film are not damaged by energetic plasma species.

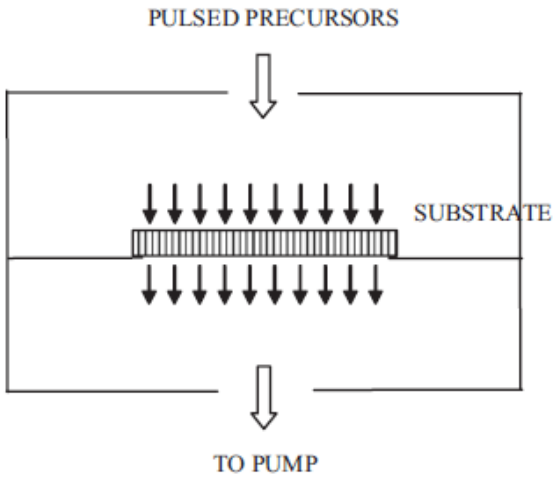

Figure 4.4: Schematic drawing of a flow through reactor. Taken from [294].

4.3 Reactors for non-planar substrates

Most commercial ALD reactors are optimized for silicon wafers. In order to expand the use of ALD and coat non planar substrates, a number of special designs have been described in literature.

4.3.1 Flow through reactor

Ritala and coworkers [294] have developed an adapted viscous reactor for coating the inside of porous or fibrous substrates. Instead of flowing the gas over the substrate, the carrier gas and reactants are forced through it, as shown in figure 4.4. This ensures that the precursor is used efficiently, as it cannot be pumped away without passing and reacting with the substrate. Chapter 11 contains a more detailed discussion of the operating mechanism and advantages of this reactor type.

4.3.2 Rotary reactor

For a number of applications, ALD on high surface area particles is needed. When the precursor is delivered over a stationary bed of particles, diffusional transport results in impractically long exposure times to coat the particles at the bottom of the bed [216]. This problem can be overcome by agitating the particles, so they do not have a fixed position, and come into contact with the reactants more easily.

One way to do this is by rotary reactors, an example of which is shown in figure 4.5. Particles are loaded in a porous tube mounted in an ALD reactor. The tube

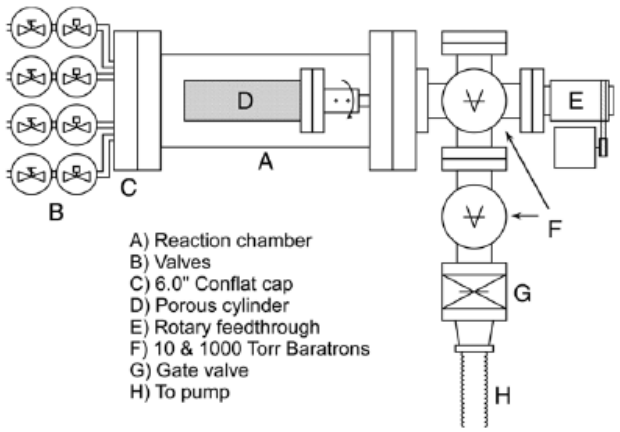

Figure 4.5: Rotary reactor used for carbon nanotubes. Taken from [33].

is pumped to a lower pressure than the reactor, and the reactants and carrier gas are sucked into the rotating tube. The combination of drag and centrifugal forces mixes the particles [33].

4.3.3 Fluidized bed reactor

Another way to agitate the powders is with a fluidized bed reactor (FBR) (figure 4.6). The powder rests on a porous membrane. The nitrogen carrier gas and reactants move through the bed, resulting in a motion (fluidization) of the powder. To enhance the mixing, there is a fan in the powder bed. The reactor can also be mounted on a vibrating plate. Fluid catalytic cracking for producing gasoline and industrial combustion installations rely on continuously operating FBRs. This is promising for the prospects of continuous, high volume powder ALD. The group of Weimer in Colorado has developed an ALD FBR [341] [164]. A system for coating battery particles has been developed at TU Delft [138], and even one of the early Soviet papers already considered FBR for ALD [358]. King et al. have monitored the gases above the powder bed with mass spectroscopy [165]. They reported that for highly reactive reactants, the 'breakthrough' of precursor (e. g. TMA) coincides with absence of reaction products (e. g. CH_4). This indicates that the ALD half-reactions have saturated. Furthermore, this also means that the precursor is used very efficiently, limiting waste and enabling a good control over the deposition process.

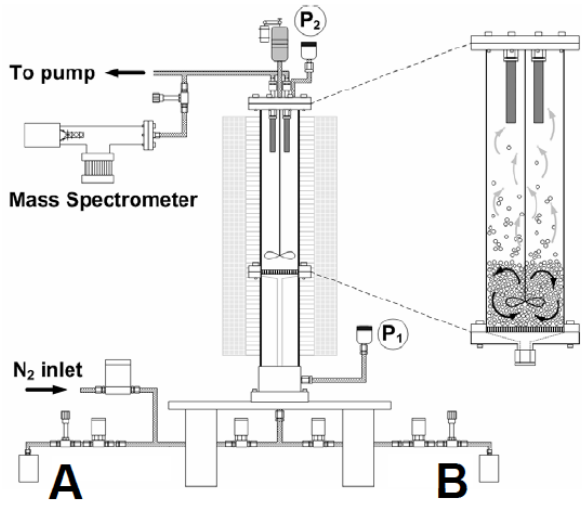

Figure 4.6: Fluidized bed ALD reactor for nanopowders. Taken from [165]

5 Experimental

5.1 Film deposition

5.1.1 Standard reactor

All reactors in our lab have been developed in-house. The reactors in Ghent are based on the design used by the group of Rossnagel at IBM [299] [145]. The group of Kessels at Eindhoven University has reactors with a comparable design [107] [109].

The standard reactor (figure 5.1) consists of a stainless steel vacuum chamber. Underneath it, a turbo molecular pump backed by a rotary vane pump continuously evacuates the chamber. The reactor is connected to a load lock via a sliding valve. The use of a load lock enables us to maintain the reactor vacuum at all times. The transfer stick can also move the sample to a PVD chamber, equipped with magnetrons or evaporators. This allows the deposition of ALD/PVD stacks without breaking the vacuum. The vacuum chamber has multiple flanges for connecting in-situ characterization instruments. Deposition on the windows on which the ellipsometer is mounted is prevented by closing computer controlled valves during ALD.

The reactor, precursor lines and bubblers are surrounded by heating wires. Thermocouples (NiCr) are fixed between the heating wires and the surfaces that are to be heated. A PID regulator provides the feedback of the wires to the thermocouple input and thus keep the components at constant temperature.

The top of the reactor is connected by a sliding valve to a quartz tube. The

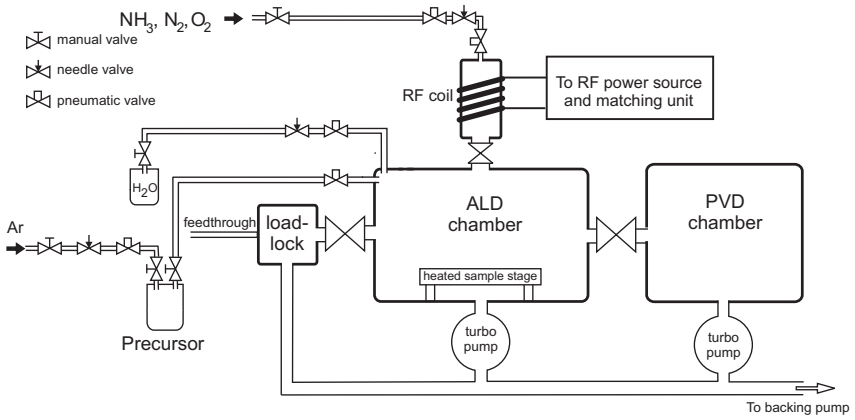

Figure 5.1: Schematic setup of the combined ALD/PVD system.

center of the tube is surrounded by a copper coil. The hollow coil is cooled by water flowing inside it and acts as an antenna. The antenna is connected to an RF generator and matching unit by a coax cable. The generator works at a frequency of 13.56 MHz.

The sample stage in the ALD reactor holds a resistive heater. The substrate temperature is calibrated by mounting a thermocouple on the substrate holder, and varying the power to the heating element. The substrate temperature is correlated with the heater temperature, which can easily be determined at all times by measuring the resistance of a Pt100 thermocouple built in the sample stage.

Precursors enter the chamber through stainless steel tubes. The flow is regulated by pneumatic valves. Most valves in the setup are controlled by LabView software developed in-house. For precursors with a low vapor pressure (i.e. all but TMA and DEZ), argon is used as a carrier gas.

5.1.2 Loading procedure

The samples are fastened onto a molybdenum substrate holder by clips. The holder is placed on a transfer stick in the load lock. After the lock is closed and pumped from atmospheric pressure to about 10^{-3} mbar with a rotary vane pump, the sliding valve is opened and the samples are transferred into the reactor. Using a z-stage, the sample holder is lifted from the transfer stick, the stick is retracted and the holder is lowered onto the heater.

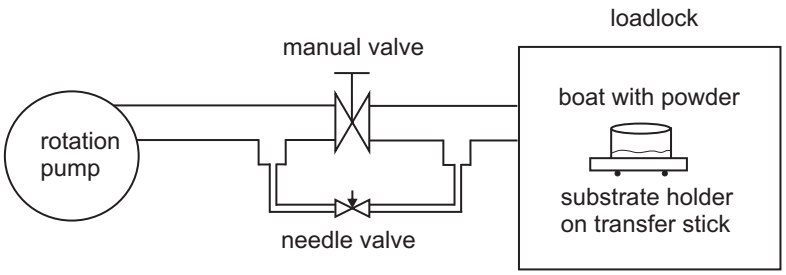

Figure 5.2: Modification of loadlock for slow purging of powder substrates.

5.1.3 Modification for powders

Collaboration with the groups of Prof J. Martens (Catholic University of Leuven) and Prof P. Van Der Voort (Ghent University) resulted in a need to perform ALD on very fine powders. The sudden pressure difference in the load lock during pumping and venting resulted in the loss of powder from the holder. To decrease the pressure more slowly, a bypass system (figure 5.2) was constructed between the rotation pump and the load lock. A needle valve enables the controlled pumping of the load lock. When the pressure is below 10^{-2} mbar, a manual valve can be opened to pump the load lock in a reasonable time.

5.1.4 Sample preparation

For depositions on flat substrates, silicon wafers were used, either with or without oxide. The silicon wafers with native oxide were cleaned using an RCA process. They were subsequently submerged in three cups of boiling water with hydrogen peroxide and an acid or base, for eight minutes each. The volume composition in the three cups was (a) 5 parts H_2O/1 part H_2O_2/1 part H_2SO_4, (b) 5 parts H_2O/1 part H_2O_2/1 part NH_4OH and (c) 3 parts H_2O/1 part H_2O_2/1 part HCl. The remaining oxide layer was removed by a short dip in a 5 $\%$ solution of HF in water at room temperature.

Samples with 100 nm thermal oxide were cleaned in the ALD reactor by exposing them to 15 s oxygen plasma before deposition.

5.2 Characterization methods

A range of tools are available for studying the ALD process and resulting films. Some can be used to monitor parameters during ALD, hence they are labeled 'in-situ' methods. Other instruments can only be used outside of the reactor in our

experimental setup, after deposition. Therefore they are considered 'ex-situ' methods.

5.2.1 In-situ

5.2.1.1 Ellipsometry

Spectroscopic ellipsometry (SE) is based on the interaction of a polarized light beam with a surface. The detector measures the amplitude and rotation of the polarization vector of the reflected light as a function of the wavelength. By modeling the substrate and film[1], film thicknesses can be determined. A recent review article discusses the application of SE to ALD [185]. A Woollam M-2000 ellipsometer was used in this work.

5.2.1.2 OES

Optical emission spectroscopy measures the intensity of light emitted by a plasma as a function of wavelength. When electrons fall back to lower energy levels in excited plasma species, light is emitted at characteristic spectral lines. These energies allow the identification of the ions, atoms and molecules in the plasma. A review of OES for ALD can be found in [210]. I monitored optical emission from the plasma with a QE65000 spectrometer (Ocean Optics) via an optical fiber attached to a lens at the plasma source. The spectrometer has a spectral range of 200 to 1000 nm.

5.2.1.3 QMS

A filament at the entrance of the quadropole mass spectrometer (QMS) emits electrons, which ionize atoms and molecules. These ions pass a quadropole electric field (RF field on 4 rods). The field separates particles according to their mass-to-charge ratio. Mass spectrometry was performed with a HPR-30 / HAL 201 RC (Hiden Analytical) QMS using a Faraday cup detector.

[1] The imaginary part of the dielectric function of the ALD films, ϵ_2, has been modeled by one or more Tauc-Lorentz oscillators in chapters 6, 7 and 8. $\epsilon_2 = \sum_{j=1}^{n} \frac{A_j E_{0j} \Gamma_j (E-E_{gj})^2}{(E^2-E_{gj}^2)^2+\Gamma_j^2 E^2} \cdot \frac{1}{E}$ for E $> E_{gj}$ and ϵ_2 = 0 for E $\leq E_{gj}$. E_{gj} represents the band gap, E_{0j} is the peak transition energy, Γ_j is a broadening parameter and A_j is an optical transition matrix element [185]. The sum goes over n oscillators. The oscillator parameters in chapters 6, 7 and 8 are given in eV. The real part of the dielectric function can be calculated by the Kramers-Kronig relation.

5.2.2 Ex-situ

5.2.2.1 SEM/EDX

In a scanning electron microscope (SEM), a beam of electrons emitted by a filament irradiates a sample. A detector captures secondary electrons emitted from the surface region. Furthermore, the impinging electrons can excite deep shells of substrate atoms. The characteristic X-rays that are emitted can be detected by an EDX (energy dispersive X-ray spectroscopy) detector, enabling the identification of elements in a specific region of the sample. SEM/EDX was carried out with a FEI Quanta 200 FEG-SEM.

5.2.2.2 TEM

The transmission electron microscope (TEM) works by irradiating the sample with high energy (order 100 keV) electrons and imaging the transmitted electrons by electric and magnetic lenses. TEM was done with a FEI Tecnai G^2 Spirit Twin scanning TEM at Hasselt University.

5.2.2.3 XPS

In X-ray photoelectron spectroscopy, monochromatic X-rays cause the emission of electrons from deep shells of atoms in a sample. The difference of the energy of an X-ray photon and photoelectron gives the binding energy of the elements, which is determined by the element and its chemical state. Although X-rays can penetrate a substrate for several micrometers, the mean free path of electrons in solids is of the order of nanometers. XPS is a surface sensitive technique, since scattered electrons do not contribute to the resonance peaks. Most XPS measurements were done with a Thermo VG Scientific ESCALAB 220i-XL with monochromatic Al Kα X-ray source at the LHMA lab of SCK-CEN. Some measurements were performed with a Surface Science Instruments (VG) S-Probe instrument, also with a monochromized Al Kα X-ray source (1486.6 eV).

5.2.2.4 XRD/XRR

X-ray diffraction (XRD) and X-ray reflectivity (XRR) are based on the constructive interference of X-rays scattering from parallel planes. For angles θ between X-rays and planes that satisfy the Bragg condition ($2 \sin(\theta)\, d = n\lambda$, where d is the distance between the planes, n an integer number and λ the X-ray wavelength), the waves interfere constructively. Crystalline films have a number of typical lattice distances, enabling the identification of the crystalline phase and its orientation by XRD. Low angles are needed for XRR. XRD and XRR were performed on a Bruker D8 Discover diffractometer with Cu Kα radiation (α = 1.54 $\AA$). For in-situ

XRD, where the diffraction lines are studied as a function of the anneal temperature, a system designed and built by Dr. Werner Knaepen was used [169]. Flowing He ensures thermal contact with a resistive heater. X-rays pass Kapton windows and are measured with a linear detector.

5.2.2.5 XRF

X-ray fluorescence is a spectroscopic technique where a sample is irradiated by X-rays. The substrate emits element specific X-rays. Because of the long mean free path of X-rays, the information depth of XRF is much higher (several 10s of μm) than for XPS. From a practical point of view, XRF is fast and non destructive. An ARTAX (Bruker) silicon drift detector was used, with a Mo or Cu X-ray source.

6 Titanium dioxide

6.1 Introduction

Titanium dioxide powder is used in pigments due to its chemical stability, non-toxicity and low cost [40]. The main application for thin TiO_2 films is as a photocatalyst [32] [69] [40]. TiO_2 has a bandgap of about 3.3 eV. When titania is illuminated with ultraviolet (UV) light, OH radicals are formed at its surface when the surface contacts water. These can break down organic materials. When a voltage is applied over the TiO_2 film, it can act as a photoelectrocatalyst [106] [41]. Related to the photocatalytic effect is the fact that TiO_2 becomes superhydrophilic upon UV exposure [320]. This effect has been exploited to create self-cleaning surfaces [228]. The high refractive index of TiO_2 is useful for optical coatings. In microelectronics, TiO_2 is interesting because it has a high k value ($\approx$100 for rutile) [156] compared to other oxides as SiO_2 (3.9), Al_2O_3 (9) or HfO_2 (25) [1]. TiO_2 ALD cycles can be combined with ALD of another element like Zr to grow complex oxides with a very high dielectric constant [280]. ALD TiO_2 has also been studied as a nonvolatile resistive random access memory (ReRAM) material [342]. In ReRAM, the resistance of the titanium oxide is switched from high to low values and vice versa by applying a certain voltage across the film. Some of the work in this chapter was done together with Dr. Qi Xie.

[1] Static k values, taken from [296]

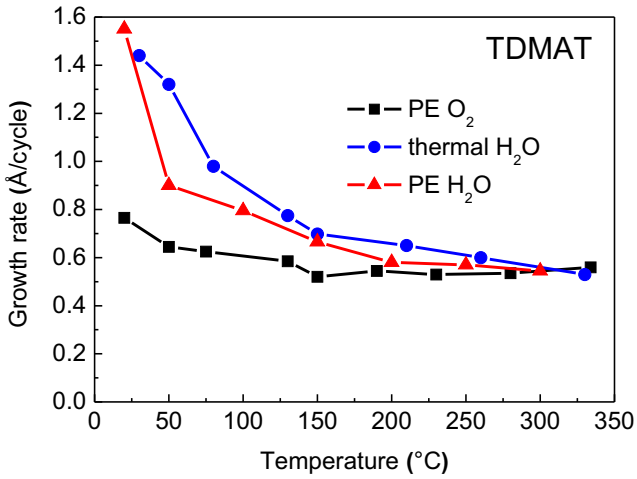

Figure 6.1: GPC of TiO_2 from TDMAT as a function of deposition temperature

6.2 Growth kinetics

TiO_2 has been grown from a number of halide and organic ALD precursors [275]. Here, the organic precursors tetrakis(dimethyl)amido titanium (TDMAT, $Ti(N(CH_3)_2)_4$) [256] and titanium tetra(isopropoxide) (TTIP, $Ti(OCH(CH_3)_2)_4$) [293] [156] were used as precursors. The precursors were purchased from Sigma Aldrich. Both were 99.999 % pure. TDMAT was heated to 30°C, TTIP to 45°C. Argon-oxygen plasma (Ar to O_2 volume ratio of 4:1) and water (both thermal and plasma) were used as reactive gases. Unless mentioned otherwise, one ALD cycle was composed of 2 s precursor, 8 s evacuation, 3 s H_2O (thermal) or 5 s plasma, and 10 s evacuation. Thermal ALD with O_2 did not lead to film growth, because molecular oxygen does not react with the chemisorbed ligands at the substrate surface.

6.2.1 TDMAT

Figure 6.1 shows the growth per cycle as a function of temperature for titanium dioxide growth with TDMAT. There is a trend that the GPC at low temperatures is higher than for high temperatures. This is consistent with other reports [100]. Although there is no ALD window with a constant GPC for ALD with water, the different ALD processes were found to be self-limiting. Above 260°C, a slow thermal decomposition of the precursor was observed by increasing the TDMAT pulse time.

The thermal ALD process can be described by the separate half-reactions [353]

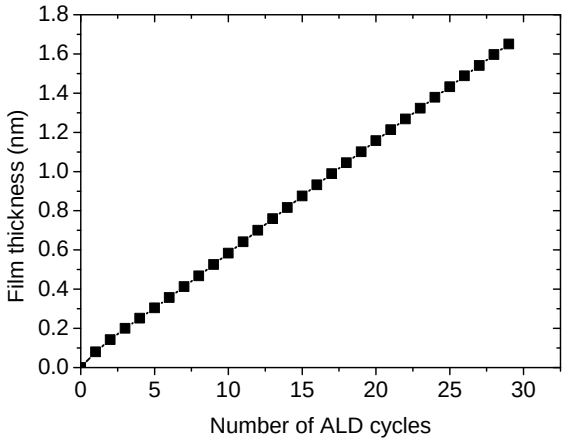

Figure 6.2: Demonstration of linearity of thermal ALD of TiO_2 with TDMAT and water at 150°C. The film thickness was measured in-situ using ellipsometry.

(a) TiO_2-OH* + $Ti(N(CH_3)_2)_4$ → TiO_2-O-$Ti(N(CH_3)_2)_3$ + $NH(CH_3)_2$
(b) TiO_2-O-$Ti(N(CH_3)_2)_3$* +2 H_2O → TiO_2-TiO_2-OH* + 3 $NH(CH_3)_2$

Even at 50°C, physisorption of TDMAT and H_2O could be excluded as possible reason for the high GPC [353]. Furthermore, the surface density of hydroxyl groups after the water pulse is constant between 50°C and 150°C [97]. Therefore, the number of reactive sites does not explain the increased GPC at low temperature for TDMAT + H_2O.

Another possible mechanism for the lower GPC at high deposition temperatures could be TDMAT desorption. Pheamhom et al. did not observe an increased GPC for TiO_2 with TDMAT/H_2O_2 with 1 s TDMAT and 10 s purge time at low temperatures [256]. This suggests that the high GPC is caused by non-desorbed intermediate products in our experiments.

Figure 6.2 shows that there is no nucleation delay for thermal TiO_2 from TDMAT/H_2O on SiO_2. Film growth is linear from the first cycle. The ellipsometer data of the titania film were fitted by a Tauc-Lorentz oscillator (A = 250, Γ = 1.85, E_0 = 4.15, E_g = 3.37).

6.2.2 TTIP

Thermal ALD from TTIP and H_2O is described by the typical half-reactions [281]
(a) 2 -OH* + $Ti(OCH(CH_3)_2)_4$ → $(O)_2$-$Ti(OCH(CH_3)_2)_3$ + 2 $HOCH(CH_3)_2$

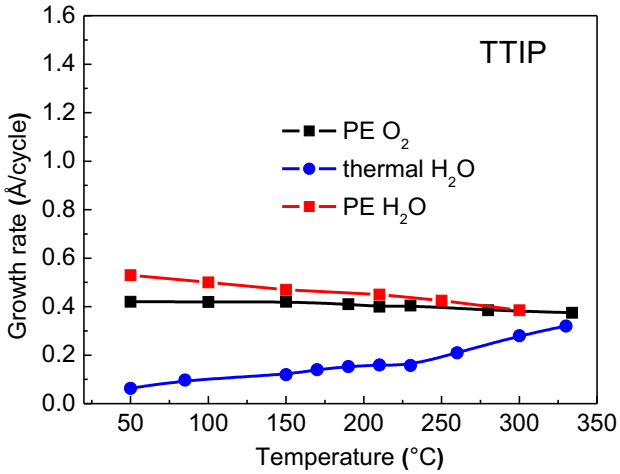

Figure 6.3: GPC as a function of deposition temperature for TiO_2 from TTIP.

(b) $(O)_2$-Ti$(OCH(CH_3)_2)_2$ +2 $H_2O \rightarrow (O)_2Ti(-OH_2)$ + 2 $HOCH(CH_3)_2$

Isopropanol ($HOCH(CH_3)_2$) is released during the TTIP and the water pulse. It is also possible that one ligand is removed during one half-reaction, and the three others during the next half reaction. At temperatures higher than 250°C, the TTIP precursor decomposes into TiO_2 and isopropanol or acetone, propene and water [281].

Figure 6.3 shows the GPC of TiO_2 from TTIP and the different reactive gases as a function of deposition temperature. For the thermal water process, the GPC rises with temperature. This indicates a slow reactivity of H_2O with TTIP [5]. Indeed, a longer water pulse time per cycle led to a higher GPC [50]. Matero et al. investigated the effect of water exposure during the ALD of different oxides, including TiO_2 from TTIP [215]. They found that a long water pulse almost doubled the GPC from 0.33 Å/cycle to 0.6 Å/cycle at 300°C. Little carbon was detected in the films. A possible mechanism for the increased GPC is that water results in OH groups necessary for binding the precursor [215]. It could also be that the ligands are not all removed during a short water pulse, and only get hydrolyzed by the next H_2O pulse. The higher reactivity of plasmas (O_2 and H_2O) results in a higher GPC compared to thermal H_2O. The GPC for the PE ALD is almost constant as a function of temperature. Rai et al. showed that TTIP chemisorption during PE O_2 ALD involves carbonates and hydroxyl groups as reactive sites [283]. During the plasma step, the isopropyl ligands are oxidized into water and carbon oxides. The H_2O is activated in the plasma and results in hydroxyl groups at the surface.

Figure 6.4 shows that the thickness of TTIP ALD TiO_2 films is linear with the

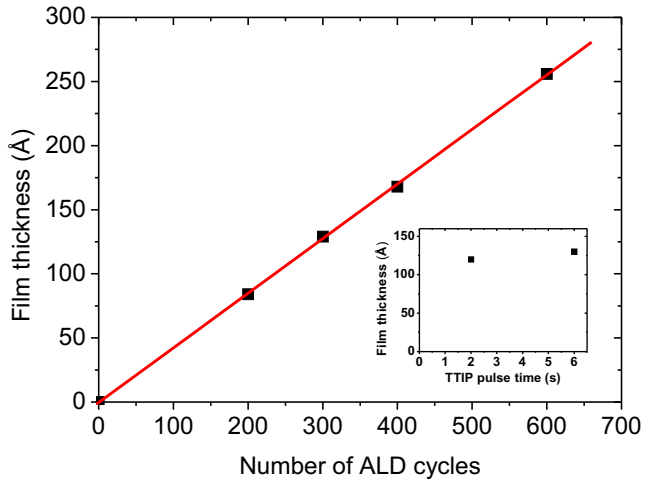

Figure 6.4: Linear film growth as a function of the number of ALD cycles for PE O_2 with TTIP at 50°C. The inset shows the saturated growth as a function of TTIP exposure during the ALD cycle for films grown with 300 cycles.

number of cycles. The thickness was measured with XRR. Furthermore, the TTIP half-reaction quickly saturates.

6.3 Crystallization and composition

Titanium dioxide has several crystalline phases at normal pressure: anatase, rutile and brookite [310]. Anatase and rutile are more photocatalytically active than amorphous titania [69] [200]. The dielectric constant of crystalline titania exceeds that of amorphous films [160]. Therefore, the crystallization behavior of the ALD films was studied.

Figure 6.5 shows the in-situ XRD data of 12 nm thick titania films grown with the different processes. TiO_2 films grown with water plasma crystallize first, for both Ti-precursors. Thermal ALD films also crystallize into anatase, but at a higher temperature. The films deposited with Ar/O_2 plasma remained amorphous, even when annealed to 900°C. In-situ XRD was also done on similar films, all grown at 50°C. The chemical composition of the films was measured to reveal the origin of the different crystallization behavior. Figure 6.6 shows the C1s peak of a 12 nm thick TiO_2 film grown with TTIP and water plasma. The peak near 284.6 eV is due to adsorbed hydrocarbons (C-C bonds). Furthermore, a small peak near 289 eV was observed on the surface of all metal oxides deposited during this Ph.D. work. This peak indicates carbonates, which form spontaneously as a result of ambient

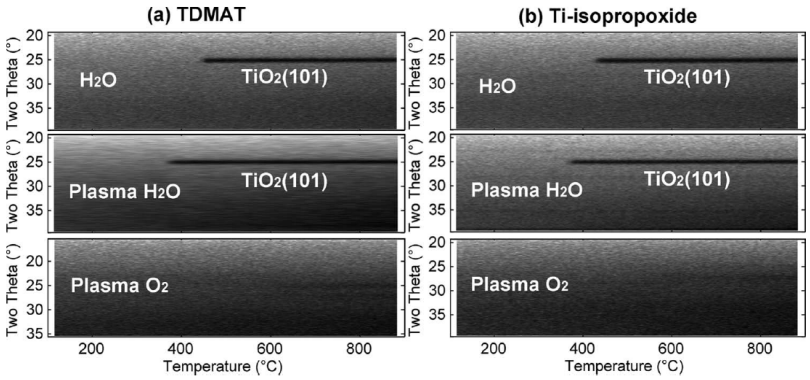

Figure 6.5: In-situ XRD of 12 nm thick TiO_2 films deposited with different processes at (a) 150°C with TDMAT and (b) at 210°C with TTIP.

		thermal H_2O		PE H_2O		PE O_2	
precursor	T_{dep}(°C)	[C]	T_{cryst}(°C)	[C]	T_{cryst}(°C)	[C]	T_{cryst}(°C)
TDMAT	50	0	532	0	411	3.5	no
TDMAT	150	0	452	0	376	2	no
TTIP	50	4.5	no	0	392	3.5	no
TTIP	210	0	431	0	373	3.5	no

Table 6.1: Carbon concentration (in atom%) and crystallization temperatures for 12 nm thick ALD films grown with different processes. 'no' means that the films did not crystallize in the temperature range studied.

CO_2.

After sputtering away the surface contamination, no carbon could be detected inside the film. Table 6.1 summarizes the levels of carbon in the titania films grown with different processes. All the films grown with oxygen plasma contain at least 2 % carbon. This could be because a mixture of oxygen with argon was used [354]. A plasma with a similar Ar/O_2 ratio was also reported to be poor at removing methyl ligands [26]. When a pure O_2 plasma is used, the deposited metal oxides are usually free of contaminants, see e. g. [261].

Figure 6.7 shows the Ti2p peak of the film grown with TTIP and water plasma as in figure 6.6. At the surface, all Ti is in the 4+ state. After the sputter step, lower oxidation numbers are observed together with Ti^{4+}. Rahtu et al. reported that ALD TiO_2 generally has a lower resistivity than expected from bulk values, due to oxygen deficiency in the films [281]. The resistivity was not measured here. However, it should be mentioned that the presence of Ti^{3+} and lower valence numbers observed in the XPS measurement is not the result of these oxygen vacancies. Low concentrations of oxygen vacancies would not be measurable with XPS, be-

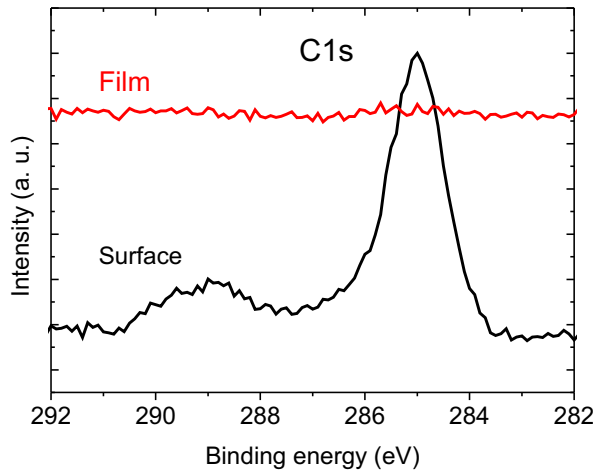

Figure 6.6: XPS signal of C1s on surface and in film grown with PE H_2O ALD from TTIP at 50° C.

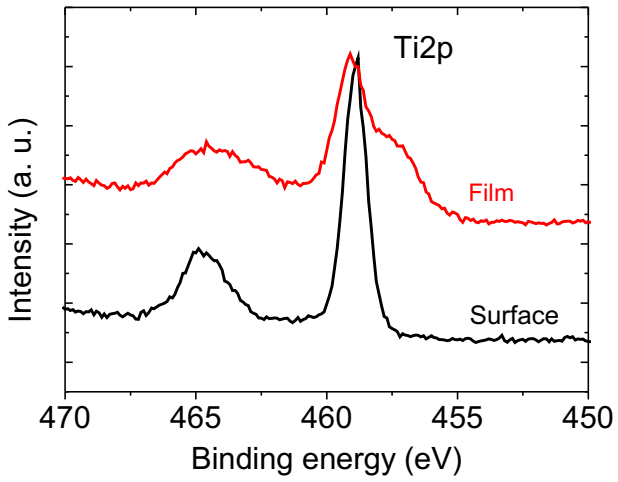

Figure 6.7: Ti2p XPS signal of TiO2 grown with PE H_2O ALD from TTIP at 50° C before (surface) and after (film) argon sputtering. Oxygen is preferentially removed, resulting in reduction of Ti.

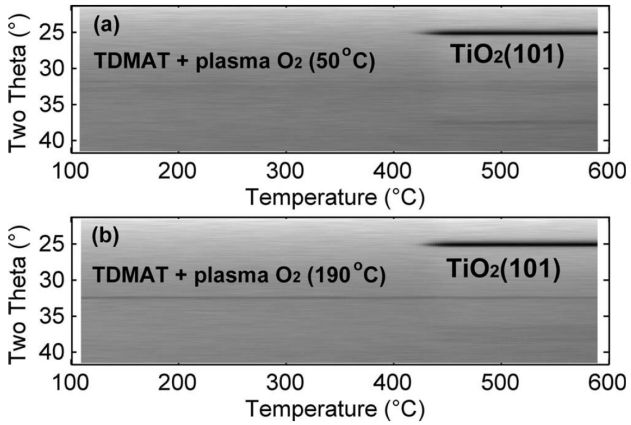

Figure 6.8: Influence of deposition temperature on PE O_2 ALD TiO_2 films grown from TDMAT. The films were (a) 32 nm and (b) 38 nm thick.

cause the accuracy is limited to about 1 atomic percent. Furthermore, because the information depth is 1 to 2 nm, some of the Ti^{3+} would be detected already in the XPS measurement of the surface. The reduction of Ti^{4+} is a result of the argon ion bombardment which preferentially removes oxygen from TiO_2 [104].

The crystallization temperatures for the 12 nm thick TiO_2 films grown with different ALD recipes are compared to the carbon impurities in Table 6.1. There is a clear correlation: C contaminated films could not be crystallized by a ramp anneal of 1°C/s to 900°C.

Next, the influence of the film thickness on the crystallization was investigated. Figure 6.8 shows the in-situ XRD of TiO_2 films thicker than 30 nm, grown with oxygen plasma. In spite of the carbon impurities, these films do crystallize.

The thickness dependence of the crystallization was further explored in pure titania grown from TTIP and water plasma (figure 6.9). Indeed, the thickness at which the film crystallizes decreases as a function of film thickness. This can be explained qualitatively by a difference in nucleation energy barrier for spherical and cylindrical crystallites [353] [352]. For the same reduction in volume free energy (by changing amorphous TiO_2 into a crystal), a sphere has less surface area than a cylinder. However, in very thin films, crystallites with sufficient volume cannot be spherical. Because the interface energy (proportional to the surface area) presents an energy barrier to crystallization, it is expected that thinner films crystallize at higher temperatures.

Many other authors have reported the crystallinity of their as deposited ALD TiO_2 films, grown with different precursors. A selection of these results taken from literature is shown in Table 6.2.

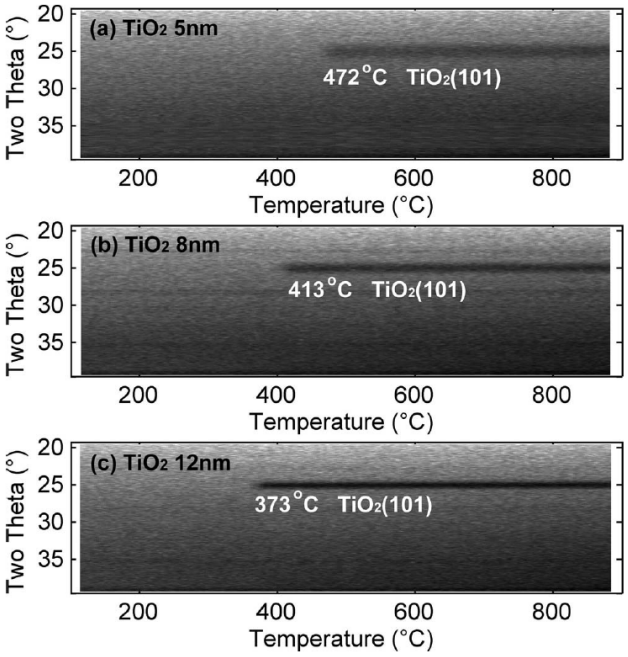

Figure 6.9: Influence of the thickness on the crystallization of TiO_2 films.

precursor	reactant	T_{dep} (°C)	plasma	thickness (nm)	substrate	phase	reference
TDMAT	O_2	200	60 W	40	SiO_2	amorphous	[207]
TDMAT	O_2	200	300 W	90	kapton	amorphous	[186]
TDMAT	O_2	250	300 W	90	kapton	anatase	[186]
TDMAT	H_2O_2	125	no	65	Si	amorphous	[256]
TDMAT	H_2O_2	200	no	65	Si	anatase	[256]
TTIP	H_2O	240	no	22	Pt(111)	amorphous	[342]
TTIP	O_2	300	100 W[a]	<10	Si	amorphous	[185]
TTIP	O_2	300	100 W[a]	>10	Si	anatase	[185]
TTIP	O_3	250	no	30	Ru[b]	rutile	[156]
$TiCl_4$	H_2O	125	no	180	SiO_2	amorphous	[4]
$TiCl_4$	H_2O	225	no	230	SiO_2	anatase	[4]
$TiCl_4$	H_2O	200	no	50	Ni, Ta, Ti	anatase	[40]
$TiCl_4$	H_2O	400	no	50	Ni, Ta, Ti	anatase/rutile	[40]
$TiCl_4$	H_2O	425	no	61	SiO_2	anatase	[137]
$TiCl_4$	H_2O	425	no	153	SiO_2	rutile	[137]
TiI_4	H_2O_2	275	no	77	glass	amorphous	[309]
TiI_4	H_2O_2	275	no	77	MgO(001)	anatase(100)	[309]
TiI_4	H_2O_2	275	no	77	αAl_2O_3(012)	rutile(101)	[309]

Table 6.2: Crystallinity of TiO_2 films as a function of precursor, reactant, deposition temperature, thickness and substrate as reported in literature. (a) Plasma power estimated based on papers by the same authors. (b) Ozone forms RuO_2 on the surface of the Ru substrate, on which the rutile TiO_2 grows epitaxially [156].

A general trend for ALD TiO_2 is that films start growing amorphously at low deposition temperatures. When the film grows to a certain thickness, it crystallizes first to anatase and next to rutile at high temperatures [137]. Furthermore, atomic layer epitaxy of anatase or rutile is observed on a number of substrates. Based on our experiments, we can add that purer films generally also lead to faster crystallization. Atomic force microscope (AFM) measurements demonstrated that the surface of amorphous ALD TiO_2 films is smooth (root mean square roughness $<$1 nm) [4] [185]. After the crystallization, a rough surface (root mean square roughness $>$5 nm) was observed. Ellipsometry showed that the GPC after crystallization was higher than before [185]. This is consistent with the discussion in section 'non-ideal ALD': although the growth is still self-limiting, more surface area is presented to the precursor molecules. A mechanism for the crystallization of the amorphous films was proposed by Aarik et al. [4]. The intermediate species formed during the Ti-precursor pulse are believed to be mobile. These particles migrate to form crystalline nuclei, thereby lowering their free energy. Literature seems to indicate that the underlying film stays amorphous [185].

Mitchell and coworkers [220] attributed the crystallization of ALD TiO_2 to growth stress: crystallization would reduce compressive stress in the films. The possibility that films crystallized due to extended time in the heated reactor was ruled out experimentally. They do not explain why the existing film remains amorphous, and only the film grown after crystallization is rough. In the same article [220], it was observed that the grain size decreases with increasing temperature. The density of nucleation sites is thus found to increase with temperature, but also depended on the stress level in the films. According to a very recent article [158], the higher GPC for crystalline films is a consequence of a higher density of hydroxyl groups at the crystalline surface. This was determined by hydrophilic testing of the films. The contact angle of crystalline films (6.5°) is smaller than for amorphous ALD titania (14°). This means that the crystalline phase has a higher wettability, indicating that more OH groups are present. The crystallization of thicker films is a boon for photocatalytic applications. TiO_2 is more photoactive when the film thickness increases, because more UV light is absorbed [69]. It was already mentioned that crystalline films are more active than amorphous ones. Furthermore, the rough surface offers a larger contact area for catalytic reactions.

6.4 Supported TiO_x/SiO_2 catalyst

In collaboration with the research group of Prof. Pascal Van Der Voort, supported titania catalysts were grown. The atomic layer deposition and XRF measurements were performed at the Department of Solid State Sciences. Ilke Muylaert synthesized the mesoporous supports, performed the catalytic reactions and the chemical and physical characterization of the supports and reaction products.

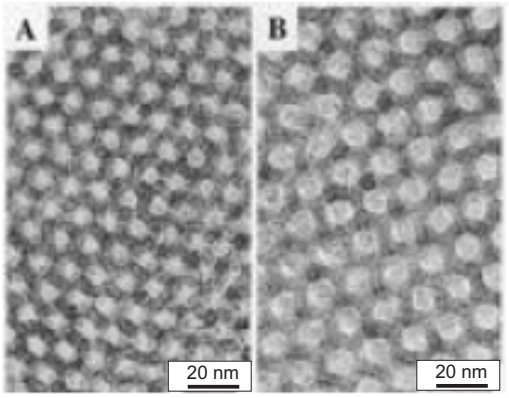

Figure 6.10: TEM of SBA15 powders with different pore sizes. Taken from [129].

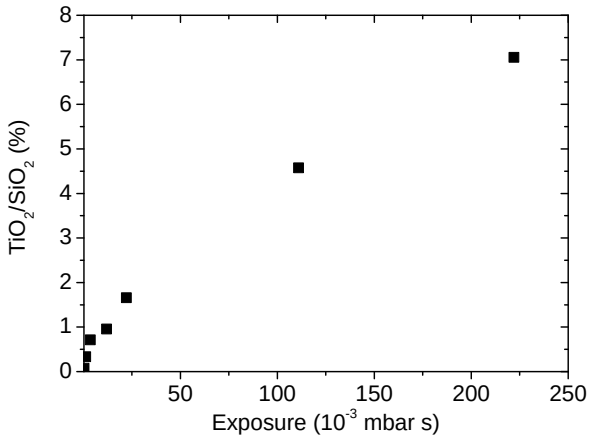

Figure 6.11: Relative amount of Ti on SBA15 as a function of TDMAT exposure.

6.4.1 Catalyst preparation

SBA15 is a mesoporous silica powder with regular pores. Figure 6.10 shows TEM images of SBA15 with different pore sizes. About 100 mg SBA15 was stored in the vacuum of the ALD reactor at 200°C to outgas the powder. At a deposition temperature of 150°C, TDMAT was pulsed into the reactor, followed by a water pulse. Figure 6.11 shows the loading of the powder for different pulse times. The X axis shows the product of TDMAT pressure and exposure time. The loading was determined by XRF. The amount of Ti on SiO_2 increased with precursor exposure.

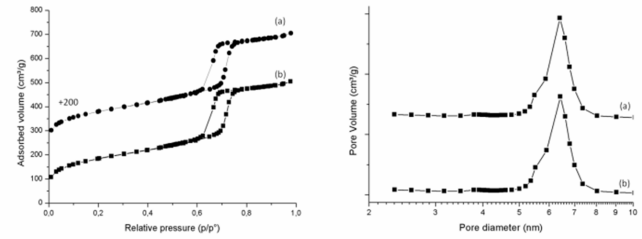

Figure 6.12: Nitrogen isotherms and and pore size distribution of the mesoporous SBA-15 materials before and after 180 s titanium deposition.

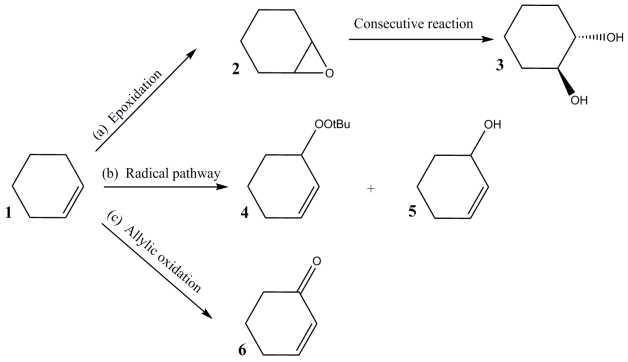

Figure 6.13: Reaction products of cyclohexene (1) + TBHP: cyclohexene oxide (2), tert-butyl-2-cyclohex-enyl-1-peroxide (4) and 2-cyclohexene-1-one (6).

Low angle XRD (not shown) and nitrogen adsorption on the SBA15 (figure 6.12) showed that ALD does not change the pore size, volume or access significantly. No TiO_2 crystallites were observed. Therefore, it can be concluded that ALD results in the growth of dispersed TiO_x sites on the silica surface.

6.4.2 Catalytic reaction, reactivity and selectivity

The liquid phase epoxidation of cyclohexene to cyclohexene oxide was studied, using tert-butylhydroperoxide (TBHP) as oxidizing agens (figure 6.13). Cyclohexene oxide is an intermediate in the synthesis of nylon.

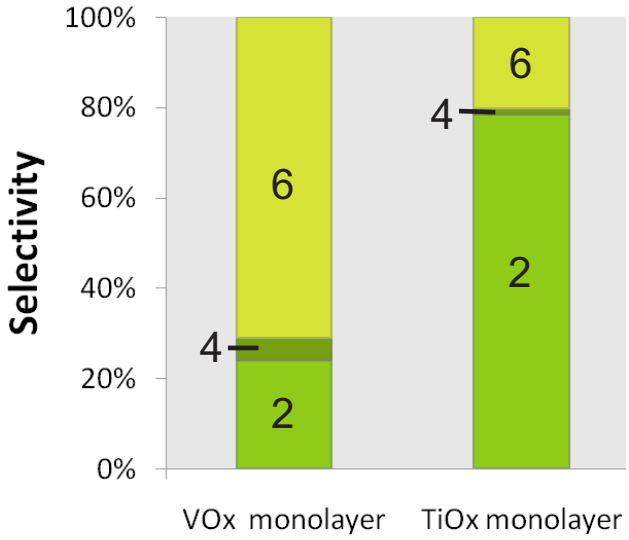

Figure 6.14: Selectivity of supported VO_x and TiO_x catalysts prepared by ALD.

#Ti/nm^2	Cyclohexene conversion (%)	(2)	(4)	(6)
(no catalyst)	18.3	2.1	84.4	13.1
0.00	23.9	3.1	84.3	12.6
0.01	20.9	8.1	73.6	18.2
0.05	17.4	27.0	61.3	11.7
0.11	24.7	44.9	41.2	13.8
0.15	28.4	49.6	36.7	13.7
0.70	43.9	78.3	20.3	1.4
1.08	53.8	71.2	27.8	1.0

Table 6.3: Catalytic properties of TiO2/SBA-15 with different Ti-loading in the liquid phase oxidation of cyclohexene. (2), (4) and (6) refer to the products in figure 6.13.

A catalyst is typically used to increase the turnover of a chemical reaction. Indeed, figure 6.15 shows that the SBA15 powder was made catalytically active by the ALD treatment. Without exposure of the plasma to TDMAT, almost no cyclohexene oxide was produced even after 7 hours.

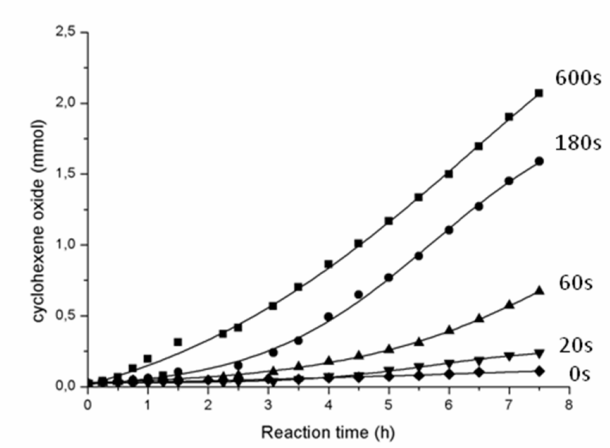

Figure 6.15: Reactivity of SBA15 exposed to different pulses of TDMAT for the synthesis of cyclohexene oxide.

As shown in figure 6.13, cyclohexene can also be converted into other, unwanted byproducts. Table 6.3 shows that at high Ti loading, more than half of the cyclohexene is converted after 7 hours. However, almost 30% of the reaction products is not cyclohexene oxide but unwanted byproducts.

The presence of other metal oxides can strongly influence the activity and the selectivity of the catalyst. Hence, vanadium/titanium mixed oxides catalysts were synthesized and evaluated for their catalytic activity.

Figure 6.14 compares the selectivity of an SBA15 support loaded with VO_x or TiO_x by a single ALD cycle[2]. The numbers on the bar graphs indicate the reaction products shown in figure 6.13. Vanadium oxide typically has a higher conversion rate. However, TiO_2 is much more selective towards cyclohexene oxide. Mixed TiO_x-VO_x catalysts supported on SBA15 combined the benefits of a high conversion rate with a high selectivity [226].

6.5 Conclusions

Titanium dioxide was deposited from TDMAT and TTIP with different reactants. ALD with water (both thermal and PE) leads to carbon free films. While a thermal oxygen process does not result in film growth, oxygen-argon plasma deposits films with some carbon contamination. The as deposited films were amorphous. They can be crystallized by annealing. Thicker and purer films crystallize at lower temperatures. Crystalline TiO_2 is more photoactive and has a higher dielectric con-

[2]VTIP was used for the VO_x, see chapter 7.

stant than amorphous films. A supported TiO_x/SiO_2 (SBA15) catalyst was made by ALD. No pore blocking was observed. The selectivity towards cyclohexene oxide formation from cyclohexene and TBHP was about 80 $\%$, almost 4 times higher than for a V_2O_5/SiO_2 catalyst.

7

Vanadium pentoxide

7.1 Introduction

Vanadium oxides are scientifically interesting materials with correlated electrons[1]. For example, vanadium dioxide (VO_2) is known to exhibit a Mott metal-insulator transition [223] near room temperature [276]. This effect can be exploited in intelligent window coatings [266] or in memory devices [59]. Vanadium pentoxide (V_2O_5) is used as a supported catalyst in a large number of oxidation reactions [258] [143] [209] [159]. For example, the oxidation of sulfur dioxide into SO_3 by vanadia [343] is an important step in the production of H_2SO_4. Thin films of V_2O_5 also find applications as electrode in lithium ion batteries [13], as optical switches [205] or even as a solid lubricant [72]. As a historical note, vanadium oxide has been studied by several generations of scientists in our department [92] [102] [43] [257] [322].

[1] Correlated electron materials [177] are solids where the electrons cannot be described as Bloch waves. The electron correlations make the materials susceptible to strong changes in resistivity or volume as a function of control parameters like temperature, chemical potential or magnetic fields. This behavior can be used in coatings and sensors.

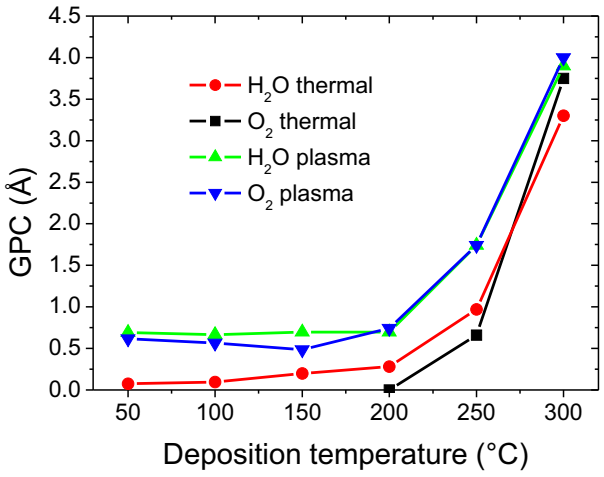

Figure 7.1: Growth per cycle as a function of deposition temperature for four different processes.

7.2 Growth kinetics

ALD precursors reported in the scientific literature are limited to $VOCl_3$, $VO(O(C_3H_7))_3$ and $VO(acac)_2$ [275][2]. Thermal ALD of V_2O_5 from vanadyl triisopropoxide ($VO(O(C_3H_7))_3$, VTIP) precursor with water was reported by Badot et al. [13]. The process has some drawbacks, including carbon contamination in the film and slow saturation during the water pulse. I studied thermal and PE ALD of V_2O_5 from VTIP with water and oxygen as reactive gases. VTIP was obtained from Sigma Aldrich and stored in a bubbler at 40°C. One ALD cycle typically consisted of 2 s VTIP, 5 s pumping, 5 s reactive gas and 5 s pumping.

Four different possible combinations of process conditions and reactive gas were tried: thermal/water (TW), thermal/oxygen (TO), plasma/water (PW) and plasma/oxygen (PO). 'Thermal' means that the reactive gas enters the reactor without being excited in the plasma source. The GPC as a function of deposition temperature for the different processes is shown in figure 7.1. Above 200°C, the deposition rate steeply increases for all processes. This signals a chemical vapor deposition-like thermal decomposition of the VTIP precursor. No deposition occurred below 200°C for the TO process. The plasma based processes (PW and PO) have a wide ALD 'temperature window' from 50 to 200°C. In this temperature range, the GPC is nearly constant, in the order of 0.07 nm/cycle. For thermal ALD with H_2O as reactive gas (TW), the GPC is much smaller compared to the

[2] A tetrakis dimethylamido vanadium (TDMAV) precursor - similar to TDMAT - has recently been developed by Air Liquide [285].

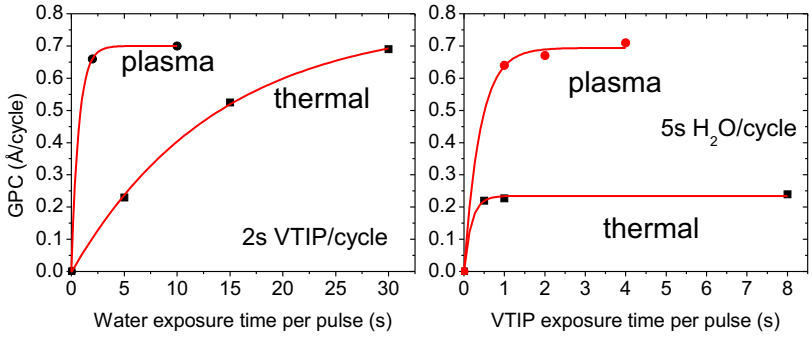

Figure 7.2: Growth per cycle as a function of precursor exposure time in the ALD of vanadia from VTIP and H_2O at 150° C. Note the different time scales on the X-axes.

plasma enhanced processes. The GPC of TW is found to increase monotonically with temperature.

The self-limiting behavior was tested for both water and VTIP in processes TW and PW at 150°C (figure 7.2).

It is clear that the film growth during the metalorganic VTIP precursor pulse saturates very quickly. Water on the other hand reacts slowly with the growing film in the thermal process. It takes over 30 seconds of H_2O pulse per cycle to complete the self-limiting film growth. When water plasma is used instead of the thermal process, the maximum film thickness is reached after a few seconds of plasma pulse. The origin of the slow water halfreaction is likely the bulky isopropoxide ligands which shield the probable reaction site of water at the vanadium-oxygen bond. After the water halfreaction, one can image the surface being covered with V-OH groups, easily binding with the vanadyl group in the VTIP precursors.

All the thicknesses reported above were determined by XRR. Figure 7.3 shows an ellipsometer measurement of a 20 nm V_2O_5 film on 110 nm thick SiO_2. The ellipsometer model, composed of two Tauc-Lorentz oscillators (A_1 = 39.8, Γ_1 = 0.64, $E_{0,1}$ = 2.96, $E_{g,1}$ = 2.08, A_2 = 77.9, Γ_2 = 5.98, $E_{0,2}$ = 6.70, $E_{g,2}$ = 1.82), fits the experimental data very well.

Figure 7.4 shows the in-situ measurement of PO grown vanadia on SiO_2 at 150°C. Contrary to the results in figure 7.2, the growth per cycle is lower than 0.7 Angstrom. We have not been able to determine the reason for this discrepancy. Increasing the precursor pressure and pulse time did not improve GPC, so limited exposure was ruled out as explanation. The in-situ data further demonstrates that there is no nucleation delay for V_2O_5 ALD on silica.

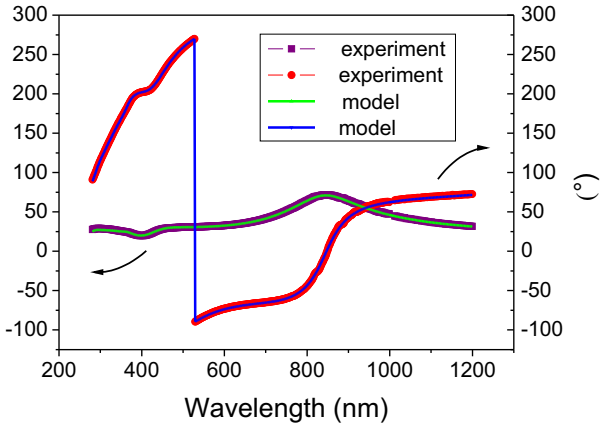

Figure 7.3: Ellipsometry data of V_2O_5 on SiO_2. The fitted model consists of two Tauc-Lorentz oscillators (see text).

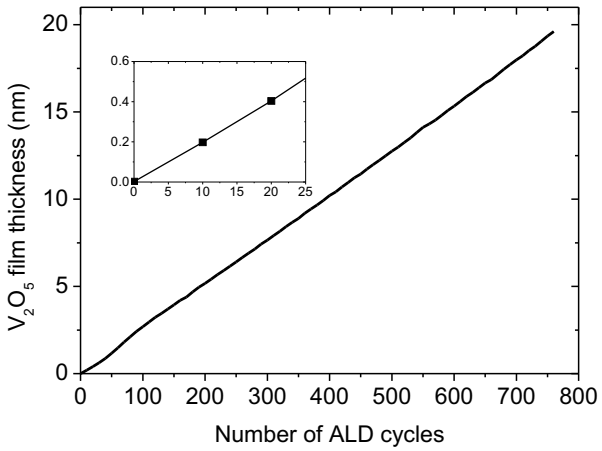

Figure 7.4: Film thickness determined by ellipsometry. O_2 PE ALD was used at a deposition temperature of 150°C. The inset shows the film thickness during the first 25 ALD cycles.

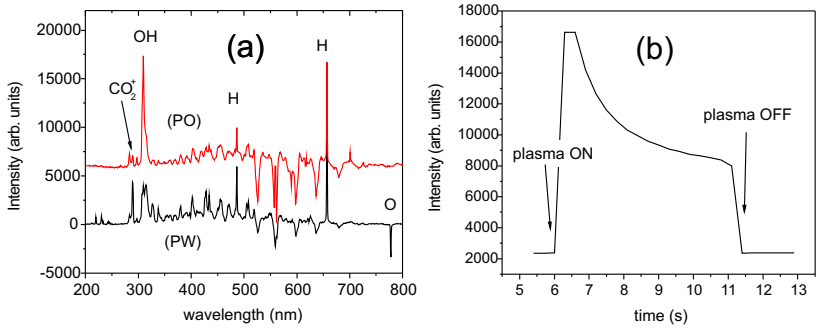

Figure 7.5: (a) Difference of optical emission spectra at the beginning and end of the oxygen (PO) and water (PW) plasma pulse during film deposition at 150°C. (b) Evolution of the Hα line (656 nm) during 5 s O_2 plasma pulse. Data were collected every 300 ms.

7.2.1 Plasma emission

The plasma was studied with optical emission spectroscopy (OES), as introduced by Heil et al. for ALD [109]. During the plasma pulse, the reactive gas reacts with the precursor molecules chemisorbed on the substrate and reactor walls. The volatile reaction products can go to the plasma source, where they are dissociated and/or excited by the electrons in the RF plasma. The fact that each species emits light with characteristic wavelengths enables the identification of the reaction products. The emission lines of the reaction products are much weaker than the lines of the reactive gas plasma, because of the lower concentration of the former. For this reason, figure 6(a) shows the difference spectra between the beginning and the end of the plasma pulse. This procedure eliminates the background of the reactive gas.

During the oxygen plasma pulse, CO_2, OH and H are present. The minima in the spectra indicate the consumption of the reactive gas during the film growth. The global reaction of VTIP with O_2 plasma during an ALD cycle can be written as

$2VO(O(C_3H_7)i)_3 + 54\ O \rightarrow V_2O_5 + 18\ CO_2 + 21\ H_2O$ (*)

showing the consumption of highly reactive oxygen radicals, combustion of the organic ligands to CO_2 and H_2O and the deposition of V_2O_5. Water is dissociated:

$H_2O \rightarrow OH + H$

and the OH and H radicals are detected with OES.

The combustion-like reaction (*) should be contrasted with the selective chemical reaction during the thermal water process [13]

$2VO(O(C_3H_7)^i)_3 + 3\ H_2O \rightarrow V_2O_5 + 6\ (C_3H_7)^iOH$

The evolution of the OES signal at 656 nm as a function of time during the oxy-

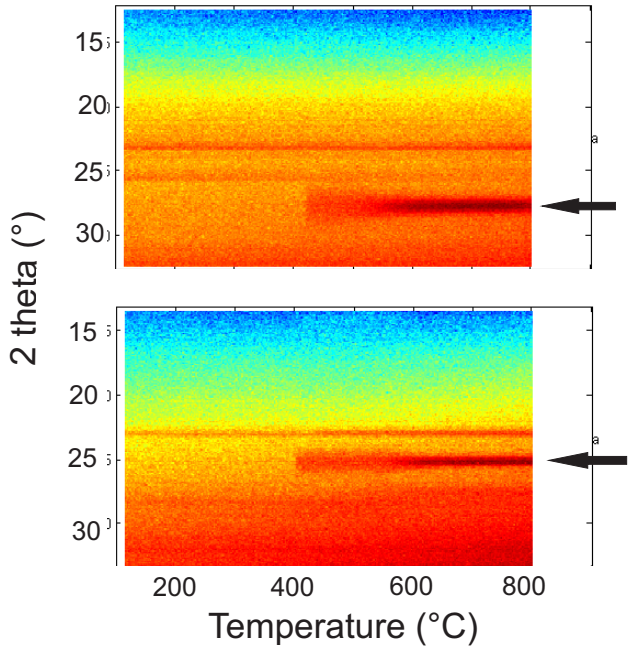

Figure 7.6: In-situ XRD of two different films deposited from VTIP and water in the thermal process at 150°C. Arrows indicate the final XRD peak. Other lines are artifacts of the detector.

gen plasma enhanced deposition of V_2O_5 is shown in figure 6(b). This wavelength corresponds to the Hα line of hydrogen. When the plasma ignites, the Hα emission increases rapidly. Less than a second after the start of the plasma, the emission peaks and decays approximately exponentially to a background OES level. This background signal is found across all wavelengths if the plasma is on. The rapid rise and fall of the H signal is further evidence of the fast reactions during PE ALD.

7.3 Crystallinity and composition

To study the crystallization as a function of temperature, selected films were first annealed under helium atmosphere in-situ, i.e. while performing XRD, cfr. the chapter on TiO_2. Two in-situ crystallization spectra of TW films deposited at 150°C are shown in figure 7.6. Darker colors represent higher XRD intensity.

Unfortunately, the XRD measurement shows that the annealing in helium is not reproducible. Furthermore, it was hard to determine the resulting phase from the peaks. Figure 7.7 shows the different crystalline phases of the V-O system. There

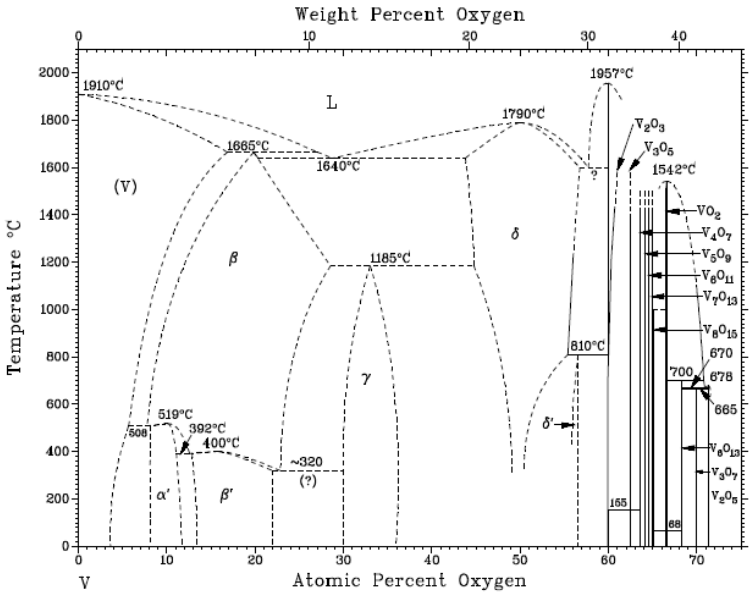

Figure 7.7: Phase diagram of vanadium and oxygen. Taken from [214].

are a large number of suboxides, containing less oxygen than the fully oxidized vanadium pentoxide.

On a 20 nm thick CVD film, we could unambiguously demonstrate that the V_2O_5 film reduced to V_6O_{13} during the in-situ XRD under helium, as shown in figure 7.8.

In order to avoid oxygen loss from the films during annealing, ALD films deposited at 150°C with the TW, PW and PO processes were annealed for 60 seconds under O_2 atmosphere in a rapid thermal anneal (RTA) machine. The combination of RTA and ex-situ XRD was chosen instead of in-situ XRD, because the latter was not yet capable of handling an oxidizing atmosphere at the time the experiments were performed.

The XRD spectra of the as-deposited films and the films annealed to 700°C are shown in figure 7.9. In all XRD spectra, the peak of Si(200) at 33° from the substrate is removed for clarity.

The ALD films deposited with water as reactive gas (TW, PW) were amorphous as deposited. These films do not crystallize at temperatures lower than 450°C under O_2. Remarkably, the TW film was found to crystallize in a V_3O_7 phase before oxidizing to V_2O_5 at higher temperatures. The film deposited with the oxygen plasma enhanced process was (001) oriented V_2O_5 as deposited. The intensity of the XRD peaks increases after annealing to higher temperatures, a re-

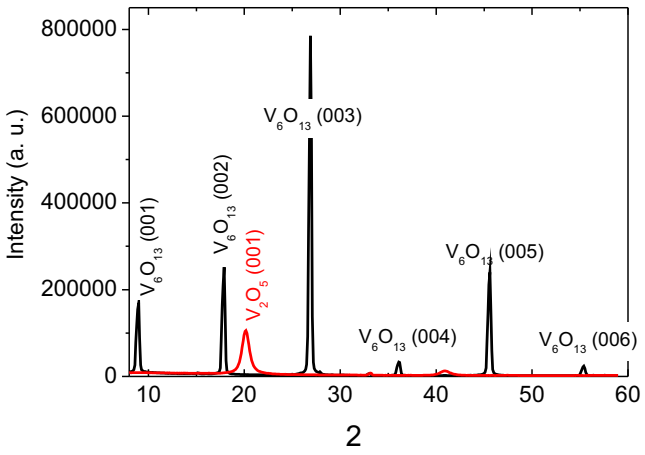

Figure 7.8: XRD of ALD vanadia film before (V_2O_5) and after (V_6O_{13}) anneal under helium atmosphere.

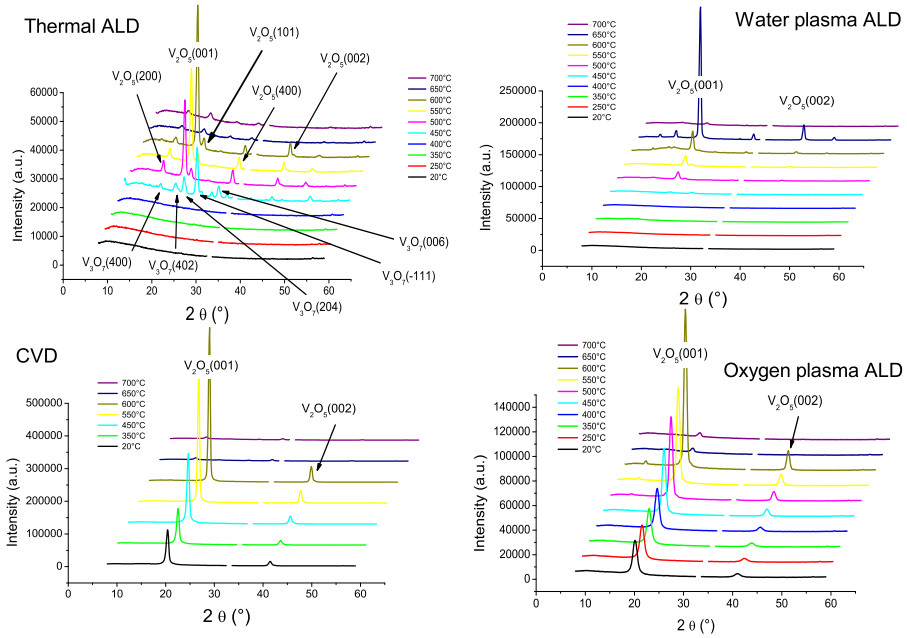

Figure 7.9: XRD spectra of 20 nm thick films annealed under oxygen. All films were deposited at 150°C. The spectra are shifted for enhanced clarity.

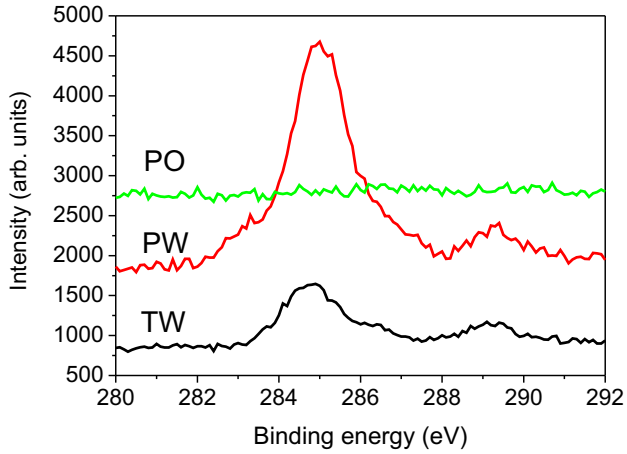

Figure 7.10: XPS scan of the carbon C1s peak in films deposited with the thermal (TW) and plasma enhanced water (PW) and oxygen plasma enhanced (PO) processes at 150°C.

sult of grain growth. When the deposition temperature was 100°C, the XRD signal of the as-deposited V_2O_5(001) film was weaker. Even thin PO films (8 nm) grown at 150°C were found to be V_2O_5(001). These observations indicate that V_2O_5 the (001) orientation minimizes interfacial energy between film and substrate. It is likely that the extra energy of the plasma enhances the formation of crystal nuclei.

The CVD film is also V_2O_5 (001) as deposited. The high substrate temperature gives the film enough energy to crystallize.

To explore the origin of the difference in as-deposited crystallinity between films deposited with different processes further, the carbon content was determined with XPS. The C1s spectra are shown in figure 7.10.

The vanadium pentoxide film deposited in the oxygen plasma enhanced process (PO) is carbon-free. The films grown from VTIP with H_2O as a reactive gas are contaminated with carbon. Paradoxically, the water plasma enhanced process (PW) resulted in a higher amount of carbon in the film than the thermal process (TW). The atomic concentration of the elements in the four samples prior to annealing is summarized in Table 7.1. The CVD film, although crystalline as deposited has a very significant 25% C contamination. When no water pulse is applied, i.e., for a purely thermal decomposition of the VTIP precursor, the carbon content in CVD is only 8%.

This behavior of thermal vs PE ALD is contrary to our previous results on the PE ALD of TiO_2 from titanium isopropoxide (Chapter 6). In that process, carbon contamination also delayed or prevented crystallization of the film. But the films deposited from H_2O PE ALD had the lower amount of carbon, O_2 PE ALD films

sample	V (%)	O (%)	C (%)	crystallization temperature (°C)
TW	30	63.5	6.5	400-450
PW	21	57	22	450-500
PO	35.5	64.5	0	(as deposited)
CW	18	57	25	(as deposited)

Table 7.1: Atomic concentration determined by XPS and crystallization temperature of vanadium oxide films.

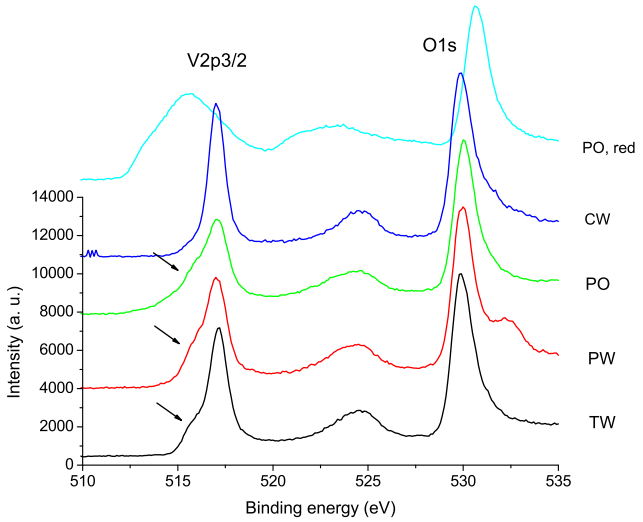

Figure 7.11: XPS spectra of the surfaces of the different films. The spectrum at the top (PO, red) shows the XPS of sample PO after 300 s Ar ion bombardment.

contained more of it. As suggested, the use of an Ar/O_2 mixture may have left some carbon contamination in the PE ALD films.

Figure 7.11 shows XPS of the V and O peaks of the different samples. For ease of comparison, the data were scaled in such a way that the O maxima coincide. These results have to be interpreted carefully. An argon sputter bombardment reduces vanadia films [322] as can be seen in the top spectrum of Fig. 7.11. Therefore, it can for example not be concluded from Table 7.1 that the stoichiometry of sample PO is VO_2, as the XRD result in Fig. 7.11 clearly indicates that the film must be V_2O_5. For all samples, the V $2p_{3/2}$ peak has a maximum at 517.2 eV, confirming mainly V_2O_5 stoichiometry (V^{5+}). However, all ALD samples - but not the CVD film - also have a "shoulder" in the V $2p_{3/2}$ peak, indicating the presence of some V^{4+} ions as well. The second, smaller maximum at a binding energy of 532.5 eV in the O 1s peak in sample PW can be assigned to H_2O contamination [322].

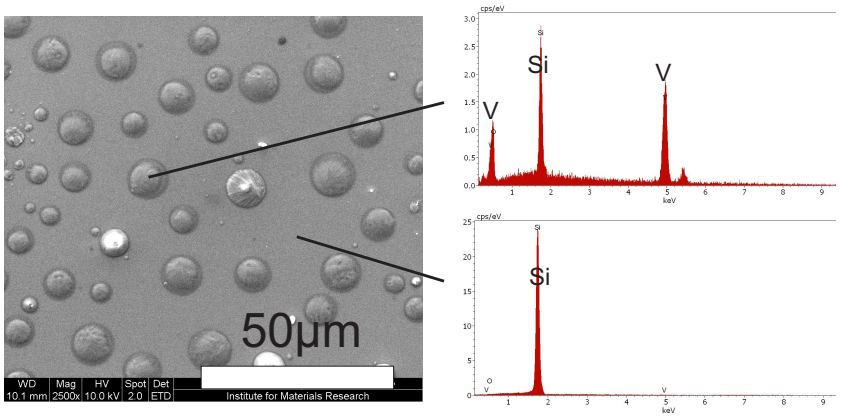

Figure 7.12: SEM of a film annealed to 700C under oxygen (left). Droplets with diameters under 10 m are visible. On the right, EDX spectra of a droplet and of the substrate are shown, indicating that the droplets are vanadia and no film remains on the rest of the silica substrate.

The XRD spectra of films annealed under O_2 to 700°C in figure 7.9 have very small peaks. The intensity of the peaks is greatly reduced compared to the films annealed to 600°C. Furthermore, the color of the samples changed from blue/purple to the grayish appearance of the silicon substrates. Therefore, a scanning electron microscopy (SEM) picture of one of the samples annealed to 700°C was made (figure 7.12).

XPS on the as deposited samples did not detect any Si, indicating a continuous coverage of the silicon substrates. After annealing to 700°C, the surface was covered with small solid droplets with a diameter of under 10 micron. Energy dispersive X-ray spectroscopy (EDX) indicated that the droplets consisted of V and O. The surface was Si. This means that the V_2O_5 films melted between 600°C and 700°C and solidified when cooling down. This agrees with the phase diagram (figure 7.7) of V_2O_5, the melting point of bulk vanadium pentoxide is 665°C, see figure 7.7.

The preferential orientation of the V_2O_5(001) films deposited by CVD or PE ALD from VTIP is as good as reactive r.f. sputtered [23] and sol-gel made vanadia [234]. Pulsed laser deposited [22], dc sputtered [72] or thermal ALD [14] vanadium(V)oxide layers reported in literature have XRD spectra which indicate some (200) oriented grains as well. A number of material properties, such as the conductivity, depend on the crystal orientation [103]. Remarkably, Mantoux et al. [211] found that films deposited in a CVD process with VTIP and O_2 at a deposition temperature of 300°C were oxygen-poor V_4O_7 and V_3O_7 [211] whereas our CVD films were V_2O_5. This discrepancy might be a result of the use of a titanium

substrate in their study. It is likely that a TiO_2 interface is formed, which consumes a fraction of the oxygen of the vanadia film. It is interesting to compare the properties of the vanadium oxide films in this work to titanium dioxide deposited by ALD from titanium tetraisopropoxide (TTIP) (see Chapter 6). Seen the similar chemistries of VTIP and TTIP, it would seem likely that the behavior is similar to the results reported in this work. Xie et al. [354] observed a very wide window for plasma ALD of TiO_2 (see Chapter 6). Thermal decomposition for TTIP only started around 300 °C. Thermal ALD of TTIP and H_2O has a GPC that increases with temperature. However, titanium dioxide is much more stable against heating under Ar, as the films remained TiO_2. V_2O_5 is much less stable against high temperatures when not under oxygen. Also the effect of the plasma pulse is very different for VTIP and TTIP. While the oxygen plasma ALD in this work resulted in carbon free, crystalline films, it left C contamination in TiO_2, preventing the films to crystallize when annealed. Although titanium and vanadium are next to each other in the periodic table and the isopropoxide precursors are alike, the only resemblence is in the growth kinetics of the ALD processes.

7.4 Conclusions

The thermal ALD process for the deposition of V_2O_5 from VTIP and water saturates very slowly because of the slow reaction of water with the growing film. Plasma enhanced processes overcome this constraint, by offering more reactive species to the surface, such as OH and O radicals. These were monitored by optical emission spectroscopy. ALD with water as a reactive gas (both thermal and plasma enhanced) results in amorphous, carbon contaminated films. ALD with oxygen plasma on the other hand results in pure, crystalline V_2O_5 with a (001) orientation as deposited.

8

Zinc oxide

8.1 Introduction

Zinc oxide (ZnO) is a semiconductor with a direct bandgap of 3.3 eV and a high exciton binding energy (60 meV). ZnO can easily be etched and it has a low cost - unlike other wide bandgap optoelectronic materials like GaN [122].These properties make it a candidate material for UV lasers or LEDs and photodetectors [122]. To make these devices possible, p-doped ZnO is developed in addition to the more common n-type ZnO. ZnO can be made in a number of shapes other than thin films. For example, ZnO nanowires (NWs) were grown as oxygen sensors of which the sensitivity can be modulated by a gate voltage [71]. The compound has a hexagonal crystal structure. This makes it attractive for piezoelectric applications [206] [264]. Furthermore, doped ZnO has several interesting applications. For example, aluminum doped ZnO (AZO) can be used as a transparent conductive oxide (TCO) electrode [176]. Such TCO has applications in solar cells and displays. Cobalt doped ZnO is a ferromagnetic semiconductor.

The electrical properties of the ALD ZnO films were investigated in collaboration with Dr. Michiel Blauw at Holst Centre (Netherlands). I did the depositions and all other measurements shown in this chapter.

8.2 Growth kinetics and reaction mechanisms

Of the precursors for ZnO ALD, diethyl zinc (DEZ) is reported most frequently (e. g. [250] [204] [202] [310] [99]). $ZnCl_2$ [136], dimethyl zinc (DMZ) [305] and elemental Zn [28] have also been used. Here, we use DEZ with water [310] [99] and oxygen plasma [250]. Ozone as reactive gas has also been described in literature [155].

Figure 8.1 shows the thickness of ZnO films grown with thermal ALD (1 s DEZ, 3 s pump, 1 s H_2O, 5 s pump) and PE ALD (1 s DEZ, 3 s pump, 2 s O_2 - 1 x 10^{-3} mbar; after 1 s a 1 s plasma pulse of 300 W, 5 s pump). The ellipsometry data were fitted with a model of the ZnO film consisting of a single Tauc-Lorentz oscillator (A = 224, Γ = 5.98, E_0 = 2.60, E_g = 3.10). XRR was not useful because of the film roughness. As figure 1 shows, there is a nucleation delay for all processes. The delay is shorter at higher temperatures and for the plasma enhanced process. The sensitivity to the initial surface conditions was also observed when the SiO_2 substrate were not exposed to O_2 plasma pretreatment. After thermal ALD, macroscopic spots were visible on the sample where no film was deposited.

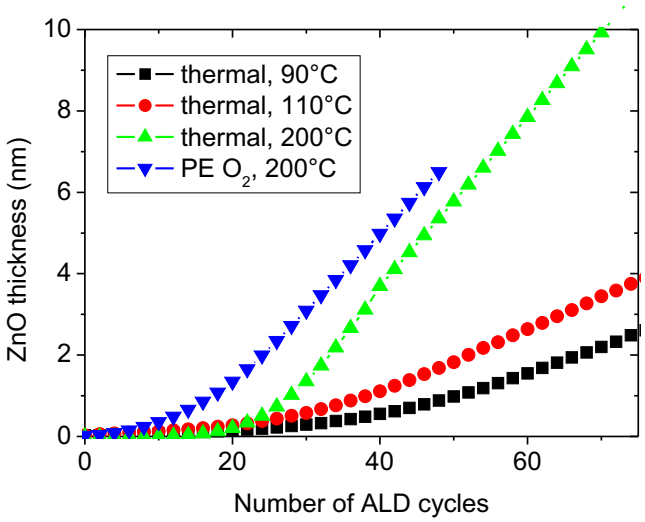

Figure 8.1: ZnO thickness as a function of the number of ALD cycles, for different process conditions.

Ferguson et al. studied the growth behavior with FTIR [78]. They found non-saturated growth at 177°C. However, for flat substrates where exposure times are relatively short, we did not find this to be a great effect. For example, the thermal process at 200°C with 1 s DEZ/cycle resulted in a ZnO film thickness of 16 nm. When the DEZ pulse per pulse was increased to 5 s (all other parameters constant),

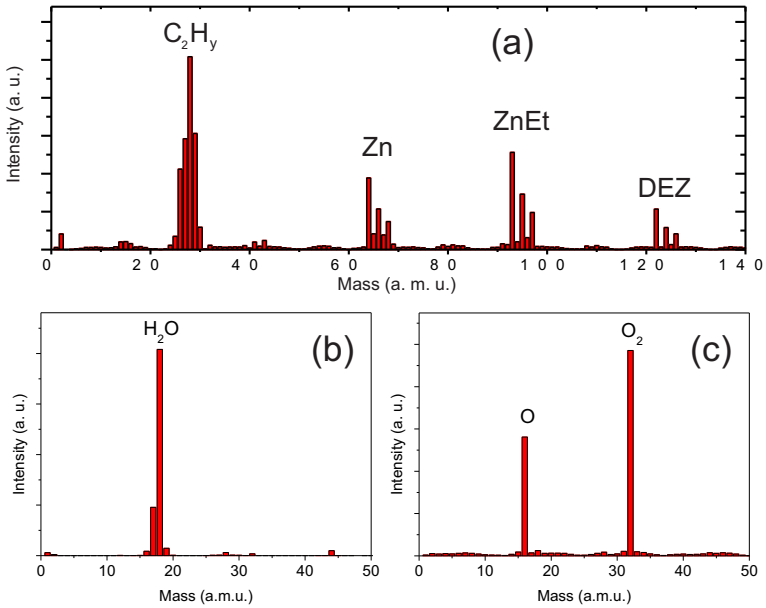

Figure 8.2: QMS bar scans of DEZ (a), H_2O (b) and O_2 plasma (c).

the film thickness was 18 nm.

The reaction products were studied with QMS. Figure 8.2 shows bar scans of the reagents used to grow ZnO. For DEZ (figure 8.2(a)), the ionized precursor is detected at a mass of 122, 124 and 126 atomic mass units (a. m. u.). Because zinc has three main isotopes (Zn^{64}, Zn^{66} and Zn^{68}), there are three lines. However, most of the lines in the mass spectrum are cracking products generated by the electron beam in the ionizer. At mass 93 (and 95, 97), Zn with a single ethyl group (ZnEt) is observed. Elementary zinc is also detected. The lines around mass 28 are products of the ethyl groups. Some of these groups have lost one or several hydrogen atoms. The carbon-carbon group is much more stable, as can be seen by the lack of CH_x lines.

The QMS spectrum of the simple water molecule is correspondingly simple (figure 8.2(b)). The only significant lines are at mass 18 (H_2O) and 17 (OH). For oxygen plasma (figure 8.2(c)), O_2 (mass 32) and O (mass 16) are detected. It should be remarked that it does not make a difference whether the plasma is ignited or not. This indicates that the oxygen radicals in the plasma recombine before they enter the mass spectrometer.

To monitor the ALD process in-situ, a single mass is followed [1] Figure 8.3

[1] Although the QMS is operated in 'multiple ion detection' mode, it was observed that switching

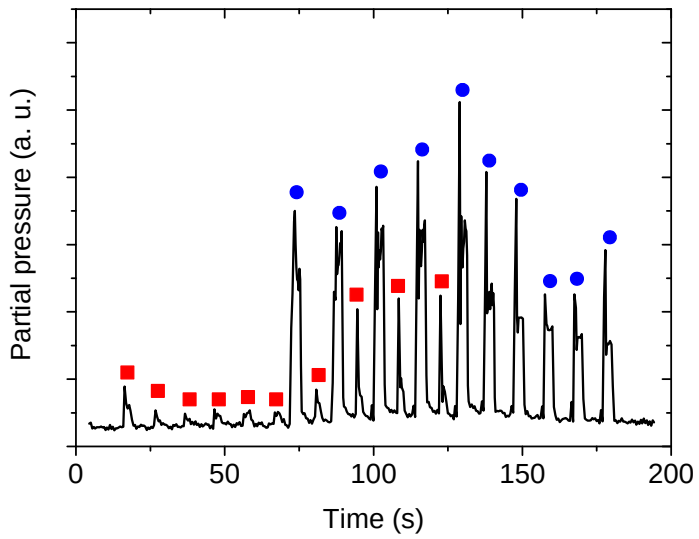

Figure 8.3: QMS of mass 18 as a function of time. Red squares indicate DEZ pulses, blue circles are water pulses.

shows the typical procedure for monitoring the ALD process. First, the precursor is pulsed five times in the reactor. This is followed by 5 ALD cycles and then 5 reactant pulses. This way, the reaction conditions are reproducible. However, the QMS signals of the subsequent cycles are not identical. Especially, some pulses have a spike at the beginning.

Figure 8.4 shows the combination of QMS spectra of masses 18, 28, 30 and 44 during thermal ALD at 200°C. As expected (figure 8.2(a)), the partial pressure of masses 30 and 28 rises during the DEZ pulse. Remarkably, the water signal (mass 18) also rises during the diethyl zinc pulse, albeit much less on the logarithmic scale compared to masses 30 and 28. During the water pulse, ethane (HEt) is formed and it is detected by QMS together with its cracking products. As a reference for PE ALD, CO_2 (mass 44) was followed as well during thermal ALD of ZnO. Although the CO_2 signal does rise during the precursor and reactive gas pulses, these rises are identical to those measured in the five first and five last pulses (cfr. figure 8.3). Therefore, we could rule out the possibility that CO_2 is formed during thermal ALD.

Figure 8.5 shows the combined mass spectra of masses 16, 18, 28, 30 and 44

between the different masses can result in non-physical correlations between the masses.

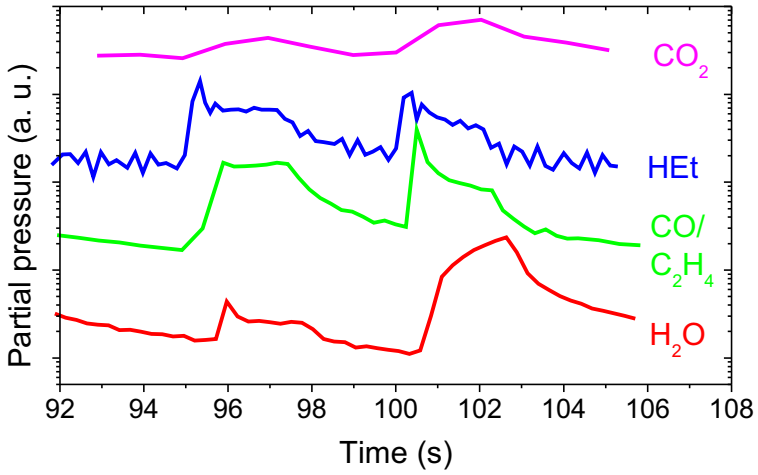

Figure 8.4: QMS of masses 18 (H_2O), 28 (CO and C_2H_4), 30 (Het = ethane) and 44 (CO_2) during thermal ALD of ZnO with DEZ (first pulse) and H_2O (second pulse). The spectra have been shifted for clarity.

during PE ALD at 200°C. During the oxygen plasma pulse, H_2O, CO and CO_2 are detected in the reactor. This observation indicates that the ligands on the growing film combust with the O radicals formed in the plasma. Some ethane (HEt) is formed as well, possibly because the water formed during the oxidation reacts with ligands which are not exposed to the oxygen radicals. The peak of CO during the DEZ pulse is a measurement of C_2H_4 instead (both species have mass 28). As can be seen in the QMS bar graph of DEZ (figure 4), C_2H_4 is one of the cracking products of the diethyl zinc precursor. The origin of the H_2O peak during the DEZ pulse, similar to thermal ALD, is harder to interpret. No cracking products of DEZ have mass 18 (figure 4(a)). In figure 8.3, all initial five DEZ pulses also result in a measurement of mass 18.

The PE ALD process was monitored in-situ by OES (figure 8.6). The plasma pulse time was taken to be 5 seconds, to approximate a pure oxygen plasma at the end of the pulse.

The difference spectrum illustrates the formation of water and consumption of oxygen during the burning of the organic ligands at the growing film. The spectrum is nearly identical to that observed during PE ALD of V_2O_5 (Chapter 7) and Al_2O_3 [109]. The 'bump' between 350 and 600 nm is a result of closely spaced emission lines of CO [109]. These OES measurements further confirm the idea put forward by Kessels and coworkers that an oxygen plasma step during ALD with metalorganic precursors results in combustion reactions [109].

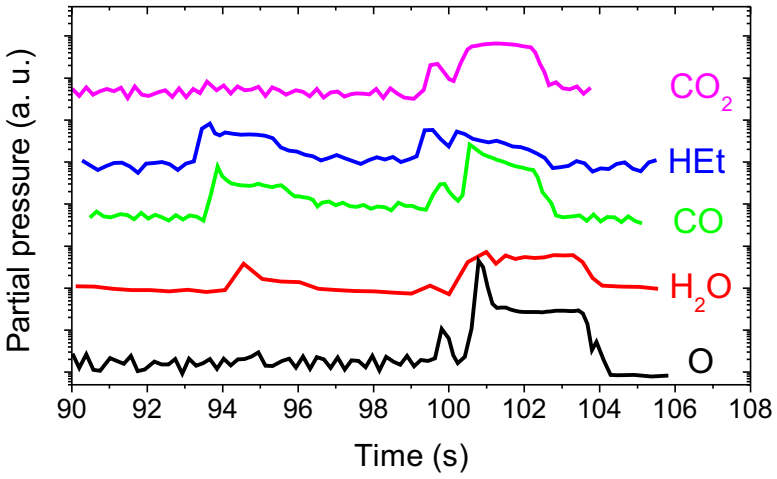

Figure 8.5: QMS of masses 16 (O), 18 (H_2O), 28 (CO), 30 (HEt) and 44 (CO_2) during PE ALD of ZnO with DEZ (pulse starting around 93.5 s) and O_2 (pulse around 99.5 s; plasma ignited 1 s later). The spectra have been shifted for clarity.

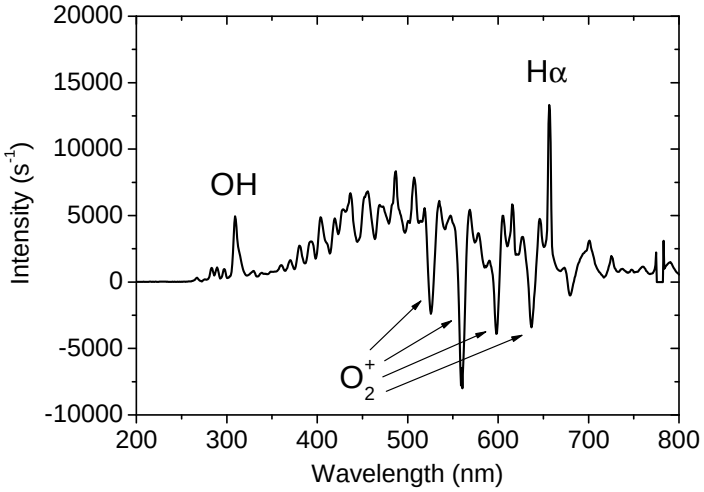

Figure 8.6: Difference of OES spectrum at start and end of a 5 s O_2 plasma pulse following 2 s DEZ exposure.

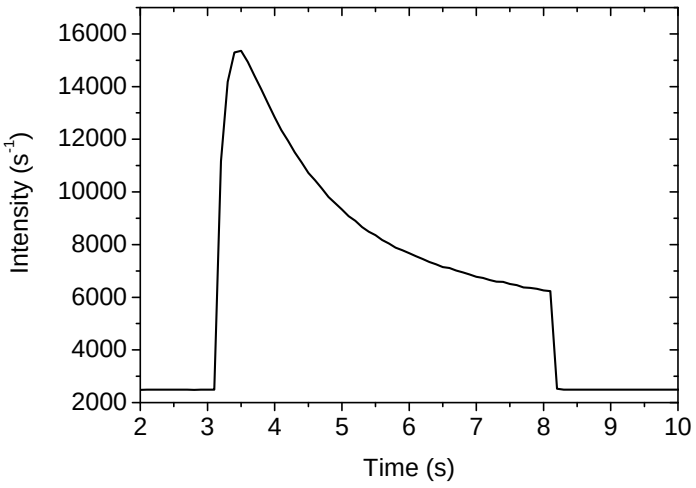

Figure 8.7: Intensity of OH line at 309 nm as a function of plasma time.

When the intensity of the OH emission line (309 nm) is plotted as a function of plasma time (figure 8.7, it is evident that the combustion reactions occur very rapidly. The maximum intensity is detected 300 ms after the RF plasma is ignited. After this moment, water is gradually removed from the plasma.

Figure 8.8 shows the XPS peaks of PE ALD ZnO deposited at 200°C. The sample is carbon free. Only at the surface, a shoulder in the O1s spectrum indicates that a detectable amount of hydrogen in the form of OH is present. Inside the film, the OH concentration is too low to measure. The XPS results of a film grown by thermal ALD at 200°C were almost identical: pure ZnO with some OH at the surface.

Based on the QMS, OES and XPS studies of the reactants and reaction products, we can write the half reactions of thermal ALD:

(a) OH + DEZ $\rightarrow$ O-Zn-C_2H_5 + C_2H_6

(b) O-Zn-C_2H_5 + H_2O $\rightarrow$ O-Zn-OH + C_2H_6

and PE ALD:

(a) OH + DEZ $\rightarrow$ O-Zn-C_2H_5 + C_2H_6

(b) O-Zn-C_2H_5 + 6 O $\rightarrow$ O-Zn-OH + CO_2 + CO + 2 H_2O

It should be noted that the ratio of CO and CO_2 was not determined exactly. To the best of our knowledge, no QMS and OES studies of ZnO PE ALD have previously been published in the scientific literature.

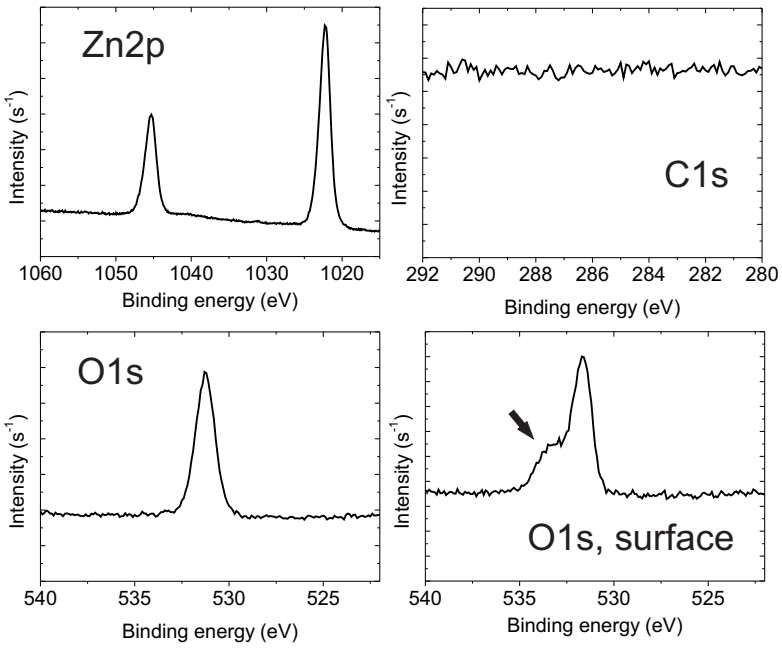

Figure 8.8: XPS data of PE ALD ZnO film after sputter cleaning, except 'O1s, surface' which shows the O1s peak measured at the surface of the film. The arrow points to the shoulder in the spectrum caused by surface OH.

8.3 Crystallinity

Figure 8.9 shows the XRD spectra of films grown at low (80°C) and high (200°C) temperatures, both for the thermal and PE process. The film grown with TMA and water at 80°C has small XRD peaks, indicating randomly oriented polycrystalline ZnO. At 200°C, the (002) orientation is larger compared to the (100) orientation. This is consistent with reports by Kowalik et al. [178], who observed (100), (002) and (110) peaks for films grown with thermal ALD at 90°C.

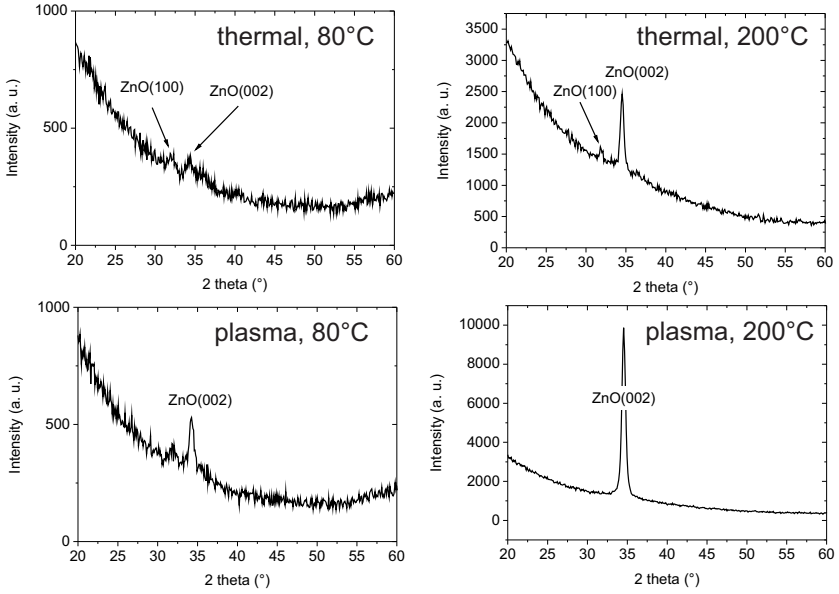

Figure 8.9: Comparison of the crystallinity of ZnO grown on SiO_2 with thermal and PE ALD at different temperatures.

For the PE ALD process, a preferential growth of Zn(002) is observed, even at low temperatures (figure 8.9). At 80°C, a small peak of ZnO(100) is still detected. At a deposition temperature of 200°C, the Zn(002) is very pronounced. The hexagonal plane of the grains is parallel to the interface with the substrate. Most likely, the energy supplied by the plasma enables the growth of a thermodynamically preferred orientation.

The OES and QMS data higher in this chapter showed that the reaction proceeds rapidly. Therefore, it was tried to reduce the reactant pulse times and purge times between the reactant pulses to just 1 s. However, the XRD spectra of the films grown with this rapid process (figure 8.10) have a single peak at about 39.5°. This does not correspond to a ZnO peak, and could attributed to the formation of

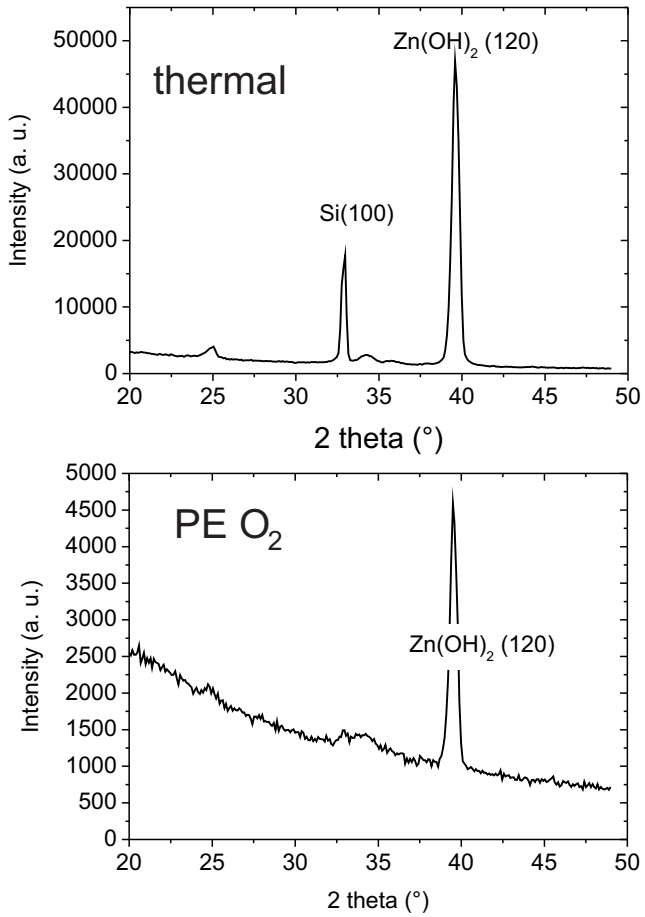

Figure 8.10: XRD of films deposited with DEZ on SiO_2 at 200°C. Top shows the result of a thermal process (H_2O reactant) with short pumping times; for the bottom film 1 s oxygen plasma per cycle was used.

zinc dihydroxide[2]. However, we should stress that some of our films grown with short pulse times only had a weak ZnO(002) peak and did not indicate the presence of $Zn(OH)_2$.

DFT calculations [225] of the gas phase reaction between DEZ and H_2O have shown that there is a low energy barrier for DEZ to hydrolyze into $Zn(C_2H_5)OH$ and subsequently $Zn(OH)_2$. These two molecules form clusters in the gas phase and elimination of ethane and water from the clusters was reported to be endother-

[2]Other zinc compounds containing oxygen, carbon or hydrogen (e.g. $ZnCO_3$) were ruled out based on the JCPDS files.

mic [225].

In principle, $Zn(OH)_2$ films can be annealed to obtain ZnO [91]. It is likely that a water film remains on the surface of the growing film in these depositions, preventing all the hydroxyl groups to react with DEZ.

For completeness, we mention that metallic zinc has been reported after thermal ALD with DEZ and H_2O [202]. Combined with our findings in the present work, this illustrates that the 'ALD' process for ZnO from DEZ and H_2O should be closely monitored in order to obtain the desired film.

8.4 Electrical properties

The intrinsic free carrier concentration of bulk ZnO at room temperature should be 10^6 cm^{-3} [99]. Experimentally however, this concentration is found to be at least 11 orders of magnitude higher in films grown with different techniques. The unintentional (n-type) doping has been attributed to zinc interstitials, oxygen vacancies and the presence of hydrogen [99] [116]. Table 8.1 compares the electrical properties of ALD films in literature with our own data.

The high resistivity of the ZnO grown with PE ALD could indicate that agressively oxidizing O radicals lead to the absence of oxygen vacancies.

For the thermal ALD films, it was observed that the resistivity decreased strongly with increasing thickness (figure 8.11). This is similar to observations of the resistivity of TiN in chapter 9 and may be related to reduced surface and interface scattering of charge carriers.

Ongoing experiments at Holst Centre are investigating the potential use of these ZnO films as gas sensors. Preliminary results show that by applying a chlorine plasma to the films prior to the electrical measurements, the conductivities of thermal and PE ALD ZnO films converge.

A similar effect of deposition temperature on the conductivity of the films was observed in a study on ALD of TiO_2 to make memristor devices [360][3]. Using RBS, it was established that the high deposition temperature titania films were oxygen deficient. The non-stoichiometry results in a higher conductivity.

8.5 Conclusions

ZnO was grown from DEZ precursor with either H_2O (thermal) or O_2 plasma. Nucleation of the film is strongly dependant on the substrate. All films were crystalline as deposited. The crystallinity follows a clear trend: enhancing the energy

[3]Memristors are passive memory devices, in which a thin metal oxide film is sandwiched between two electrodes (usually platinum). The on/off value of the memristor is determined by the conductivity of the oxide. Writing and reading is done by passing a current through the device. A high voltage moves oxygen vacancies, changing the resistivity

process	T_{dep} (°C)	resistivity (Ω cm)	mobility ($cm^2/V\ s$)	carrier density (cm^{-3})	reference
single crystal reference (no ALD)			300		[204]
2s DEZ - 8s pump - 3s H_2O (thermal) - 4s; 200 cycles	>150	<0.02	>15	1 - 3.7 · 10^{19}	[204]
2s DEZ - 8s pump - 3s H_2O (thermal) - 4s; 200 cycles	<125	>10	<3	$1{\cdot}10^{17}$	[204]
60ms DEZ - 8s pump - 15ms H_2O (thermal) - 20s pump	170	<0.004	27	$6{\cdot}10^{19}$	[121]
60ms DEZ - 8s pump - 15ms H_2O (thermal) - 20s pump	130	0.04	15	$1{\cdot}10^{19}$	[121]
60ms DEZ - 8s pump - 15ms H_2O (thermal) - 20s pump	100	>2	3	$8{\cdot}10^{17}$	[121]
60ms DEZ - 8s pump - 15ms H_2O (thermal) - 20s pump	130	0.04	15		[99]
60ms DEZ - 8s pump - 15ms H_2O (thermal) - 20s pump	120	0.05	14		[99]
60ms DEZ - 8s pump - 15ms H_2O (thermal) - 20s pump	100	>2.6	3		[99]
4s DEZ - 4.5s pump - 2.5s H_2O (thermal) - 4.5s	150	1.85	24		[250]
4s DEZ - 4.5s pump - 1.5s O_2 (plasma, 150) - 0.5s	150	too high to measure			[250]
1s DEZ - 10s pump - 1s H_2O (thermal) - 10s pump; 200 cycles	200	0.0105			this work
1s DEZ-3s pump-1s H_2O (thermal)-6s pump; 200 cycles	200	0.0064			this work
1s DEZ - 3s pump - 1s O_2 (plasma, 300W) - 6s pump; 200 cycles	200	too high to measure			this work
1s DEZ - 3s pump - 1s O_3 (180μg/ml) - 6s pump; 200 cycles	200	too high to measure			this work

Table 8.1: Comparison of electrical properties of ALD ZnO films

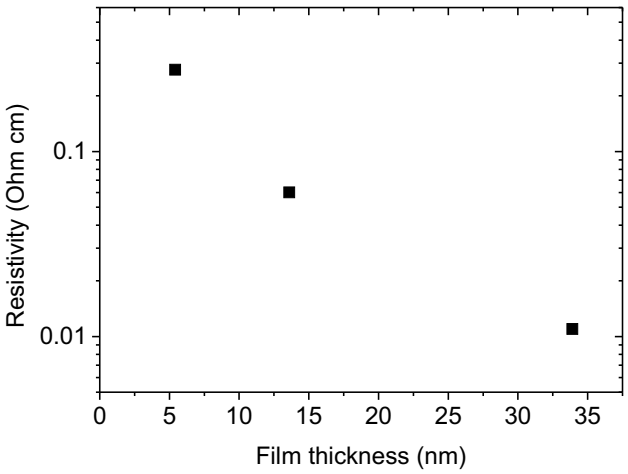

Figure 8.11: Resistivity of ZnO grown with thermal ALD at 200°C as a function of thickness.

of the growing film (by increasing the deposition temperature or using PE ALD) results in ZnO with a (001) preferential orientation. Zinc oxide deposited by thermal ALD is electrically conductive, while PE ALD ZnO is not. This difference could not be attributed to impurities, so it is believed to stem from oxygen vacancies in the thermal ALD ZnO.

9 Titanium nitride

9.1 Introduction

Titanium nitride is a hard and metallic material which has found many applications, e.g. as a wear resistant coating [119], or as a diffusion barrier for copper in microelectronics [248] [219] [64] [153]. The low resistivity and high thermal stability of TiN make it a candidate for capacitator electrode material in dynamic random access memory (DRAM) [88] and metal gate in complementary metal oxide semiconductor (CMOS) structures [79]. As device dimensions continue to shrink, new deposition techniques need to be introduced for making thin, uniform and conformal coatings. Atomic layer deposition (ALD) meets these demands. ALD is based on sequential, self-terminating reactions of a precursor and a reactive gas [275]. There are no gas phase reactions as in conventional chemical vapour deposition. The ALD process results in pinhole-free, conformal films.
Previous studies have reported thermal ALD of TiN with tetrakis(dimethylamido)-titanium (TDMAT, $Ti(N(CH_3)_2)_4$) and NH_3 [64, 79, 219]. Plasma enhanced (PE) processes have been studied with TDMAT and H_2, H_2/N_2 mixture and N_2 plasmas as reactive gas [153]. Also PE ALD using $TiCl_4$ and H_2-N_2 was reported, depositing lower resistivity films [107]. However, chlorine impurities may be detrimental to device reliability. In this chapter, we study the growth kinetics, resistivity and purity of TiN films grown using ALD/PEALD with a metalorganic precursor and N_2 or NH_3. The copper diffusion barrier properties of the resulting TiN films were tested by in-situ XRD measurements.

9.2 Growth kinetics and resistivity

TDMAT (Sigma Aldrich, 99.999%) was pulsed into the chamber by Ar carrier gas. The TDMAT precursor bottle was kept at 40°C. The tube from the precursor bottle to the chamber is heated to 50°C to prevent condensation of the precursor gas. The vacuum chamber walls were heated to 80°C.

All depositions were done with a cycle time of 25 s, unless mentioned otherwise. One cycle consists of 2 s exposure to precursor, 9 s of pumping, 6 s of exposure to the reactive gas and another 8 s of pumping. When PEALD is used, the plasma is on for 5 s at a power of 300 W, unless mentioned otherwise. No attempt was made to optimize the cycle time.

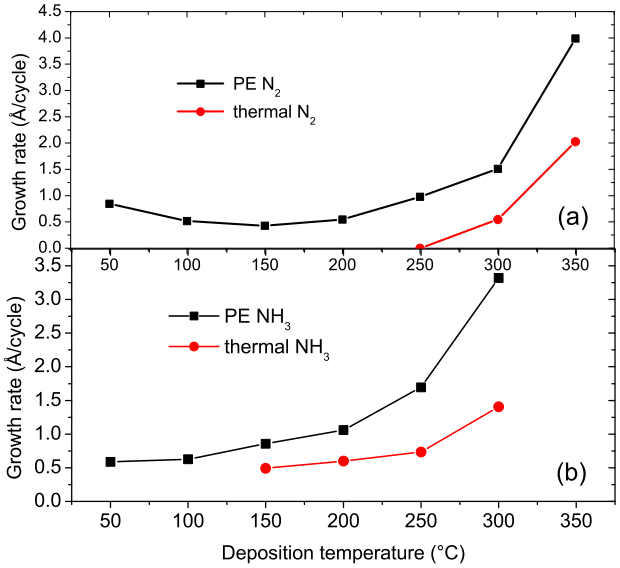

Figure 9.1: Growth rate as a function of temperature for films deposited using (a) nitrogen and (b) ammonia as reactive gas. Results for thermal and plasma enhanced processes are shown. In general, the growth rate for ammonia processes is higher than the corresponding nitrogen ALD.

The growth per cycle is shown in Fig. 9.1 as a function of deposition temperature. The GPC is higher for PEALD compared to thermal ALD for both N_2 and NH_3. Except for the PE process below 100°C, the GPC with ammonia is higher compared to processes with nitrogen.
There is no 'ALD window', a temperature range for which the GPC is constant. The lack of a clear window was already mentioned in [64]. Instead, the GPC for ammonia rises monotonically with temperature. This is unwanted, as it requires

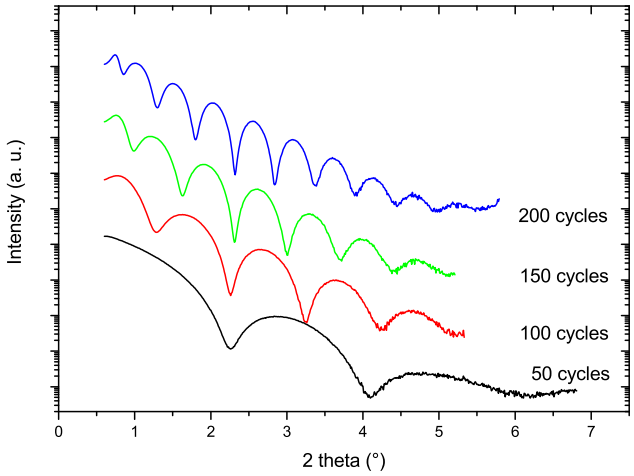

Figure 9.2: X-ray reflectometry spectra from TiN film deposited by 50, 100, 150 and 200 cycles. The thinner the film, the broader the peaks. Spectra have been shifted along the y-axis for clarity.

extra control on the deposition temperature in order to deposit films with the same thickness in different batches.
Contradicting our measurements, Kim et al. [153] found a high growth rate of 3.4 Å, independent of temperature between 200 and 300°C with a nitrogen plasma at 300W. The thermal TDMAT and ammonia process gave a GPC of 4.4 Å according to reference [219]. It seems that papers that give high values for the growth rates [219] [154] [203] use ALD reactors where the partial pressures of the reactants are high (TDMAT 4 Pa, NH_3 44 Pa in [203]). This pressure regime is not feasible in our design (figure 5.1), because all gases have to be pumped away via the turbomolecular pump. The growth rates up to two atomic layers per cycle has been explained by readsorption of the reactant [203]. However, Elam *et al.* [64], who reported similar growth rates as the ones in this work, commented that the higher growth rates might be caused be thermal decomposition of TDMAT. Infrared spectroscopy [58] of chemical vapor deposition of TiN from TDMAT in N_2 indicated that below 205°C the precursor decomposes slowly, which explains the presence of carbon in nearly all the ALD TiN films. Above 205 °C the decomposition rate increases [58]. In figure 9.1, the GPC of ALD TiN also increases above 200°C if a TiN film is already present. For thermal ALD with N_2 on Si and SiO_2, deposition only starts above 250°C.

Figure 9.2 shows the XRR spectra from TiN films with different thicknesses. For clarity, the spectra have been shifted along the y-axis. As opposed to Rutherford backscattering (RBS) or ellipsometry, XRR, which is based on interference,

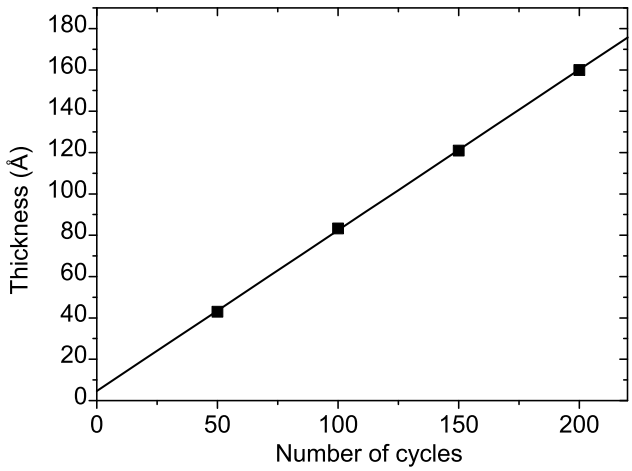

Figure 9.3: Film thickness as a function of the number of ALD cycles. The line is a linear fit to the measured points. Deposition temperature was 200° and the plasma power was 300 W.

provides a measurement of the true geometrical thickness of the film [53]. θ is the angle between the film surface and the incident X-ray beam. By curve fitting, thickness, roughness and density can be derived from the spacing, amplitude and location of the interference fringes.

Figure 9.3 shows that film thickness increases linearly with the number of cycles in the range measured. The fitted linear curve has a finite value for zero cycles. The growth rate at 200°C is about 0.8 Å/cycle.

Nucleation of the film is easy, as seen from figure 9.3. The fact that the fitted curve intersects the thickness axis above the origin, suggests that the studied ALD process has substrate-enhanced growth [275]. This can occur if the number of reactive sites on the substrate is higher than on the ALD-grown film. The GPC is then higher at the very start of the deposition.

The saturation behavior was tested by changing the precursor pulse time. The growth rate does not fully saturate at increasing precursor exposure time (figure 9.4). The fitted curve shows the expected ideal ALD saturation behavior [275]. Our results indicate that there is a slow, continuous growth after saturation. This is in agreement with earlier work by Elam *et al.*, who could not find saturation as a function of TDMAT exposure for thermal growth of TiN with NH_3 [64]. Remarkably however, if H_2O plasma is used instead of NH_3 plasma for the deposition of TiO_2, perfect saturation does occur [353].

The resistivity of the titanium nitride film as a function of plasma power and

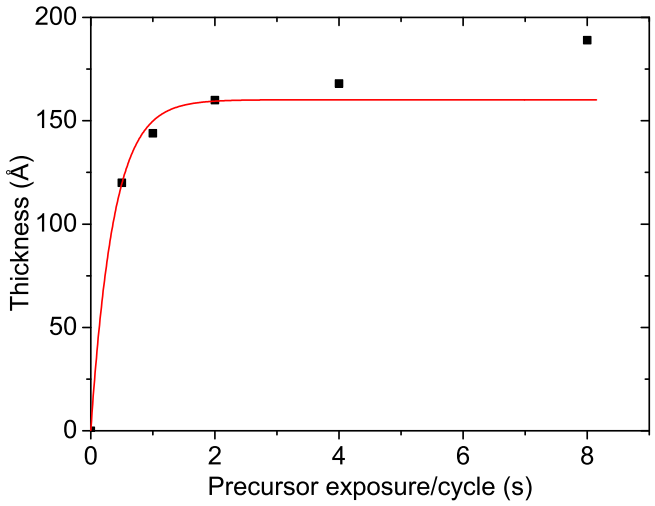

Figure 9.4: Thickness of films deposited at 200°C with 5s NH_3 plasma as a function of precursor exposure during each cycle. The fitted line assumes ideal saturation and does not take into account the measurements above 2s. The result indicate a slow, continuous growth after one second of precursor pulse.

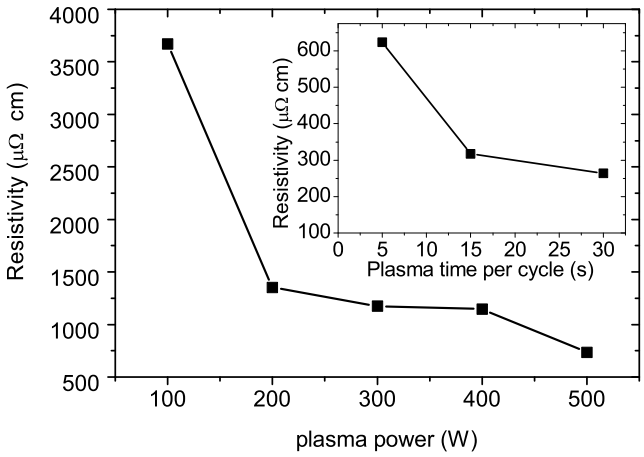

Figure 9.5: Resistivity of TiN films deposited with TDMAT and NH_3 at 200°C as a function of plasma power. Increasing power results in lower resistivity. Inset shows the effect of plasma time on the resistivity (plasma power 500W).

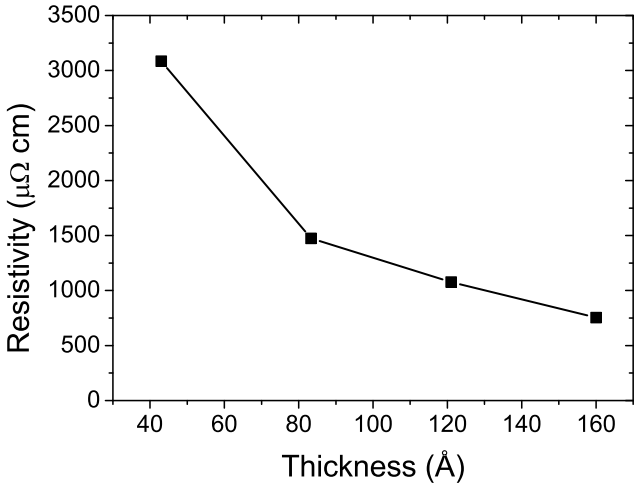

Figure 9.6: Resistivity as a function of thickness for films at 200°C and 6s plasma at 300 W.

plasma exposure time is given in figure 9.5. The resistivity decreases strongly by an increase in plasma power between 0 and 200W. A further increase of the plasma power only results in a marginal improvement of the conductivity. Longer plasma times further reduce the resistivity of the TiN films. The choice of plasma parameters does not significantly affect the growth rate.

The resistivity is given as a function of thickness for films deposited with ammonia at 200°C in figure 9.6. Resistivity roughly halves as thickness doubles. It is well known that the resistivity of very thin films is also influenced by contributions from surface, interface and grain boundary scattering (see e.g. [300]). These effects become more important as thickness decreases. This may explain the increase in resistivity for decreasing thickness as observed in figure 8.11.

9.3 XPS Analysis

The film deposited with a thermal process 'sample T' (200°C, 6 s ammonia, 2 s TDMAT) and the one with the best PEALD process 'sample P' (200°C, 30 s NH_3 plasma at 500 W) were investigated with XPS, as they represent high and low resistive samples.

Figure 9.7 shows XPS depth profiles for samples T and P. The chemical composition is more or less constant throughout the films, except at the surface, where more carbon is detected. Sample T is severely contaminated with oxygen (37%) and carbon (9%). Sample P is less oxygen contaminated (5%) and contains under

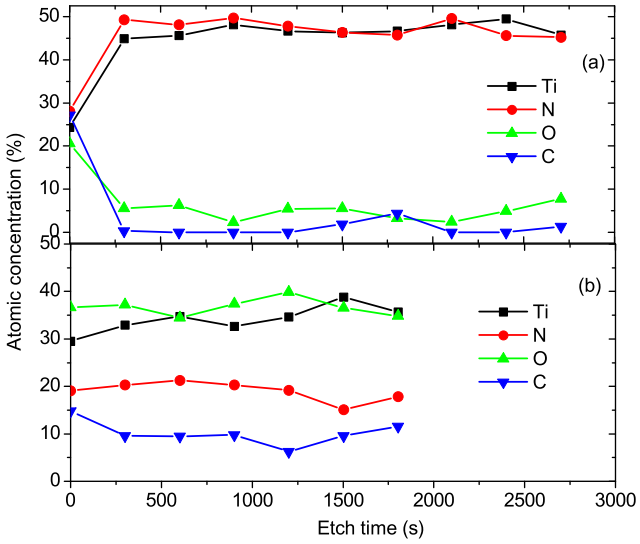

Figure 9.7: XPS depth profile of films deposited by (a) plasma enhanced ALD with 30 s 500 W NH_3 plasma and (b) thermal ALD with 6 s NH_3 pulse, both at 200° C. The film deposited by PE ALD has far fewer impurities.

1% carbon.

In figure 9.8, the carbon signal at the surface and in the film is shown. The C1s peak in the film is shifted to a lower binding energy, 282.0 eV, compared to maximum at 284.6 eV at the surface. This indicates that C is bound to Ti, so the film contains TiC impurities. If carbon were still bound to N, as in the precursor, the binding energy would be higher. As the binding energy of titanium in TiC is very close to that in TiN, it is easier to identify the carbon state directly in the C1s spectrum and not in the Ti XPS spectrum.

Figure 9.9 shows the XPS spectra of the Ti2p peak of the film deposited by (a) sample P and (b) sample T. There are two peaks due to spin-orbit coupling: the highest one, at the lower binding energy (BE), is $2p_{3/2}$, the other one is $2p_{1/2}$. The Ti2p peak has contributions from titanium bound in TiO_2 (peak BE about 458.6 eV) and TiN (peak BE about 455.0 eV). There are also smaller contributions from TiC and $TiO_{1.5}$ [243]. In figure 9.7(b), it is clear that the surface consists mainly of TiO_2, while the interior of the film consists of TiN with oxygen impurities.
The XPS results for TiN films deposited with ammonia are summarized in table 9.1.

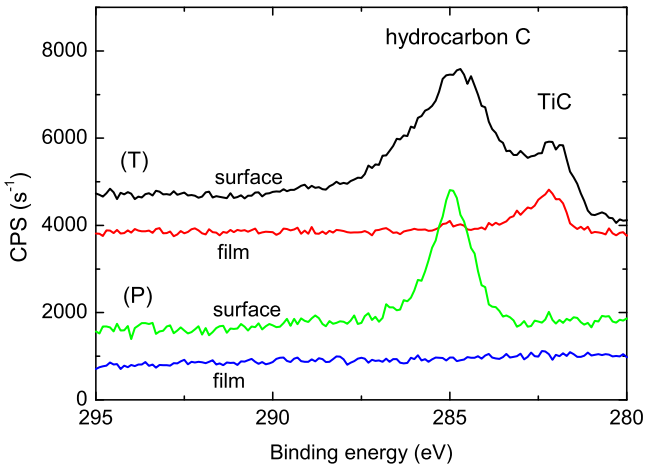

Figure 9.8: XPS signal of the C1s peak in the films deposited by (T) thermal ALD with 6 s ammonia and (P) PE ALD with 30 s 500 W NH_3 plasma, both at 200°C. At the surface, the intensity of the C1s peak has a maximum at a binding energy of 284.6 eV. In the (T) film, the C1s peak is shifted to 282.0 eV, indicating titanium carbide formation. No carbide was formed in the film deposited with the plasma process.

T_{dep} (°C)	plasma power (W)	reactive gas, pulse time	[Ti] (%)	[N] (%)	[O] (%)	[C] (%)	resistivity ($\mu\Omega$cm)
200	(no plasma)	NH_3, 6s	35	19	37	9	52900
100	300	NH_3, 6s	42	40	15	3	4828
200	300	NH_3, 6s	43	37	19	<1	1177
300	300	NH_3, 6s	41	32	22	5	1207
200	500	NH_3, 6s	45	43	10	2	763
200	500	NH_3, 30s	47	47	5	<1	180

Table 9.1: Overview of deposition parameters, film stoichiometry and resistivity.

Comparing the film deposited with ammonia in a thermal and plasma process at 200°C (see table 9.1) shows that the thermal process results in significant carbon contamination. The plasma removes most of this. More importantly, the film deposited with thermal ALD has so much oxygen in it, that it is hardly conductive anymore. It is rather a mixture of titanium oxide and titanium nitride. It has also been suggested [107] that PEALD results in denser films, improving conductivity. The carbon content in PEALD films deposited at 100°C and 300°C is higher than at 200°C. At low temperatures, not enough thermal energy will be available to remove the organic ligands from the growing film. At higher temperatures, thermal decomposition of the precursor is more important.
It was found to be impossible to get rid of all the oxygen in the films. This is

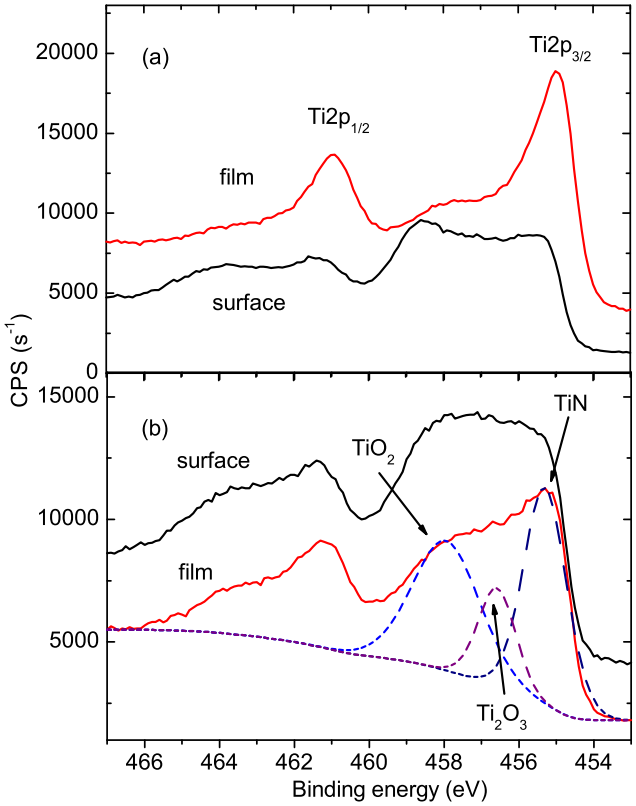

Figure 9.9: XPS profile (surface/film) of the Ti2p peak of the film deposited by (a) plasma enhanced ALD with 30 s 500 W NH_3 plasma and (b) thermal ALD with 6 s NH_3 pulse, both at 200°C. Peak decomposition shows that the film deposited by thermal ALD is severily oxidized.

surprising, as the described ALD process does not use molecules with oxygen. However, Ti easily reacts with water. Even if small traces of H_2O are present during the deposition - which takes 25s to deposit about one monolayer or less - the preferential reaction of Ti and H_2O will result in a heavily oxygen contaminated film. The oxygen concentration in the sequence 100-200-300°C deposited by PEALD shows that the oxygen level increases with temperature. Comparison with the growth rate curve (figure 9.1) learns that the optimal process temperature has to deliver enough thermal energy to have an acceptable growth rate, but low enough to prevent excessive O incorporation and precursor thermal decomposition.
There is a clear correlation between the conductivity and impurity concentration (Table 9.1).

9.4 Cu diffusion barrier properties

To investigate the diffusion barrier properties of the films, 5 nm thick TiN layers were grown by ALD on HF dipped Si(100) wafers. Next, the sample was transferred to the PVD chamber and a 50 nm thick Cu film was sputtered on the titanium nitride without breaking the vacuum. As a reference, a sample was prepared without TiN diffusion barrier.
The Cu/TiN films were heated at a ramp rate of 0.2 °C/s and an XRD scan was measured every 2 seconds. The resulting spectra are shown in figure 9.10. The intensity of the diffraction peaks is represented on a logarithmic scale, where black is the highest intensity [168].

The copper film deposited directly on the HF cleaned Si(100) has grown epitaxially [36]; only a strong Cu(200) peak at 2 $\theta \approx 50°$ can be seen. The films deposited on the titanium barrier layer have XRD peaks originating from grains with Cu(111) (at $2\theta \approx 43.5°$) and Cu(200) orientation. At a certain temperature, the Cu peak signals decrease due to the reaction of copper and silicon forming Cu_3Si. The temperature at which the Cu XRD peaks decrease at the highest rate is used to define the Cu_3Si reaction temperature [168]. This temperature indicates the breakdown of the diffusion barrier. As is indicated in figure 9.10(a), without barrier, the compound forms at 233°C. The breakdown temperature of the ammonia PE ALD film was 608°C, that of the nitrogen PE ALD film 617°C. A 5 nm thick TiN film grown by reactive dc sputter deposition had a breakdown temperature of 594°C. With a thermal ammonia ALD process, the copper reacted away at 638°C.

The in-situ XRD measurements show that the films deposited with ALD are pinhole free. Indeed, if they were not, Cu would diffuse through defects in the TiN film and silicide formation would start at about the same temperature as for the stack without TiN diffusion barrier. It can be seen that the film deposited by the

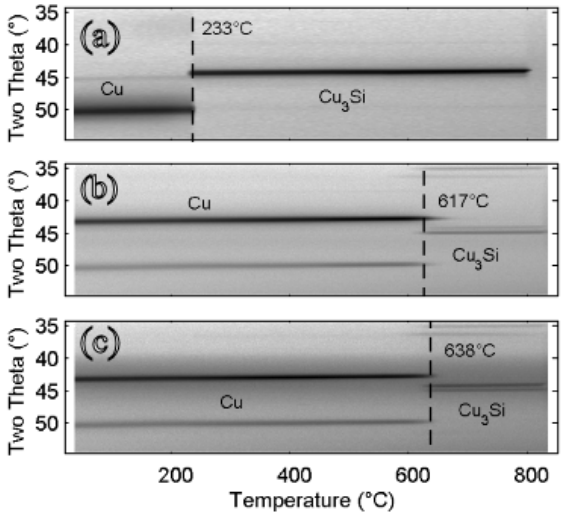

Figure 9.10: In-situ XRD data showing the reaction of 50 nm Cu with the Si(100) substrate. Heating rate was 0.2 °C/s. In (a), Cu was deposited directly on Si. (b) 5 nm TiN barrier layer deposited by PE ALD with N_2. (c) 5 nm TiN barrier layer deposited by thermal ALD with NH_3. The Cu_3Si formation temperatures are indicated by the dashed lines.

thermal process has slightly better diffusion barrier properties then the ones grown with ammonia or nitrogen plasma.

Using combined profilometry and QCM (quartz crystal microbalans) measurements of the TDMAT + NH_3 thermal process, Elam et al [64] found that the porosity of the TiN film was about 45% when deposited at 200°C. In Cu diffusion experiments with PVD TiN barrier films [248], the more porous films resulted in a lower breakdown temperature. Thus it was expected [64] that TiN films deposited with the thermal process would not be effective Cu barriers. However, our results (figure 9.10) show no significant result between thermal and plasma ALD. The copper diffusion barrier properties of ALD TiN films deposited with hydrogen and nitrogen plasmas [154] were also found to be almost the same, irrespective of the composition of the film.

9.5 Conclusions

Titanium nitride films were grown by atomic layer deposition from TDMAT. The purest films (less than 6 atom % impurities) were grown with long plasma exposure time during each cycle. Plasma is very effective in removing carbon impurities. To remove oxygen, long plasma exposure is also necessary. The copper diffusion

barrier properties of 5 nm thick ALD TiN was determined by in-situ XRD. Taking into account the low resistivity and good diffusion barrier properties of the films, the described process can be useful for the production of Cu interconnect diffusion barrier layers.

10 Ruthenium

10.1 Introduction

Ruthenium films are used as nucleation layers for the electrodeposition of copper on diffusion barriers [181] [182] [183] [251] [126] [355] [151] and as capacitator electrodes [1] [189], because of their low resistivity and thermal stability. As the aspect ratio of trenches and via holes increases, traditional deposition techniques as physical vapor deposition (PVD) and chemical vapor deposition (CVD) are experiencing difficulties in depositing films homogeneously in these structures.

Other applications where ALD of Ru could be an interesting addition to existing coating techniques include fuel cell electrodes and catalysis [24] [161]. For example, ruthenium is a better catalyst than other noble metals as Pt or Pd for the oxidation of CO into CO_2 at high oxygen pressures [244]. It can also be used in the Haber-Bosch process for the synthesis of ammonia [54]. ALD Ru has already been applied to aerogels, in order to make high surface area catalysts [24].

Both for microelectronic and catalytic applications, the texture (crystal orientation of the grains) of the Ru film is important. It has for example been shown [151] that the adhesion of copper to (001) oriented Ru is better than on Ru(100). The high activity of Ru in the oxidation of CO at high O_2 pressure has been attributed to RuO_2(110) epitaxially grown on Ru(001) [244].

We demonstrate here that it is possible to control the texture of the ALD Ru films. More specifically, highly oriented Ru(001) can be formed either by depositing Ru on a TiN buffer layer or by annealing the samples. Electron backscatter

diffraction (EBSD) measurements show that the annealed films have much larger grains compared to the as-deposited film. For Ru/Si(100), contrary to expectation, no silicide could be formed during annealing of ALD films to 800°C. However, Ru_2Si_3 was formed with sputter deposited ruthenium. We show that this is caused by the formation of a nitride barrier on the Si substrate by the ammonia plasma.

10.2 Film growth

Ru films were grown following a PE ALD process proposed by Kwon et al. [181]. The ruthenium(II)di(ethylcyclopentadienyl) ($Ru(EtCp)_2$, Sigma Aldrich) precursor bubbler was heated to 60°C, while the reactor chamber walls were heated to 75°C to prevent condensation. $Ru(EtCp)_2$ is pulsed into the chamber using Ar carrier gas. After 5 s metalorganic precursor pulse, the chamber is pumped for 10 s and an ammonia plasma step (5 s, 500 W) removes the organic ligands, followed by 10 s pumping. Applying 300 pulses resulted in 10 nm thick Ru films at a deposition temperature of 350°C.

The PE ALD process with $Ru(EtCp)_2$ has several advantages over thermal ALD with O_2. Unlike the solid precursors $Ru(thd)_3$ and $Ru(Cp)_2$ (see table 10.1), $Ru(EtCp)_2$ is a liquid at room temperature. This prevents possible problems with deposition of precursor on cold spots in the line between bubbler and reactor. Oxygen based processes can result in RuO_2 [182], which has a higher resistivity than metallic Ru. Furthermore, the PE ALD films are denser [181] than thermal ALD films.

Titanium nitride (TiN) was deposited at 200°C, from tetrakis(dimethylamino)titanium (TDMAT) and long (15 s) NH_3 plasma (500 W) pulses to avoid C and O impurities (see chapter 9).

The magnetron sputter deposited films were grown from a 3 inch Ru target, 0.5 Pa Ar atmosphere at a power of 350 W for 2 minutes. RCA cleaned Si(100) substrates which received a HF dip to remove native oxide were used. Anneals were done under N_2 flow in a Rapid Thermal Processing (RTP) system, for 60 s at 800°C.

The film thickness as a function of the number of ALD cycles is shown in figure 10.1. It is only after a delay of about 80 cycles that the ruthenium film starts growing on silicon. The slight change in the ellipsometry signal before Ru growth is likely caused by the modification of the Si surface due to the plasma (see further). A delay of 50 cycles is observed for the deposition of Ru on TiN. A delay in Ru growth has also been measured for the same precursor and process at 270°C on TiN [183] and TaN [355]. This has been attributed to a lower adsorption probability of $Ru(EtCp)_2$ on the initial surface compared to a Ru surface [183]. Furthermore, the time to reach saturated absorption on the original surface is longer than for saturation on Ru [183].

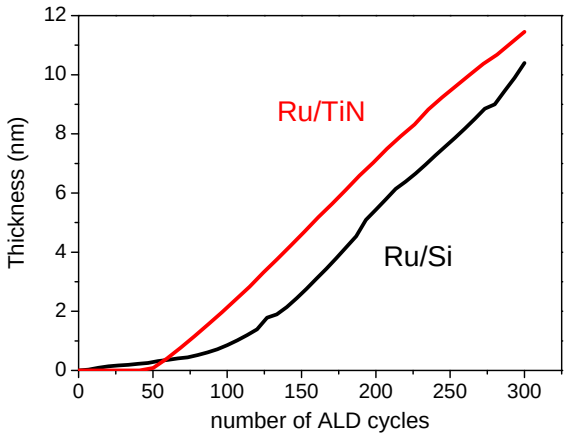

Figure 10.1: Film thickness as a function of number of cycles determined by in-situ ellipsometry. There is a delay of about 80 cycles before a Ru film starts growing on Si, and of 50 cycles for Ru growing on TiN.

The increase in film thickness, after correction for the nucleation delay, is about 0.45 Å/cycle for both substrates. This seems reasonable as the surface is covered with Ru once the film is growing. The fact that the film thickness does not increase linearly with the number of cycles (after nucleation) is a result of the imperfectness of the model with which the ellipsometer data were fitted.

10.3 Orientation and microstructure

Figure 10.2 shows the XRD signal of the as-deposited 10 nm Ru films on Si (a) and TiN (b). The film deposited directly onto Si is composed of a random mix of (100), (001) and (101) oriented grains. Note that we use a notation with three indices for orientations of the hexagonal Ru metal, so Ru(001) is the same as Ru(0001) in some publications (see insert in figure 10.2). Ru deposited on 20 nm TiN was (002) textured. For completeness, the weak XRD spectrum of 20 nm thick ALD TiN film is shown in figure 10.2(c). It can be seen that the cubic TiN has a preferential (002) orientation.

It is not unexpected that the substrate influences the film orientation. Table 10.1 shows literature data on the orientation of as-deposited ALD Ru. The orientation of the grains in the Ru film depends on the precursor, the substrate, the deposition temperature and the plasma power. It has been found that the Ru(001) orientation is more pronounced at higher plasma power [181] and at higher deposition

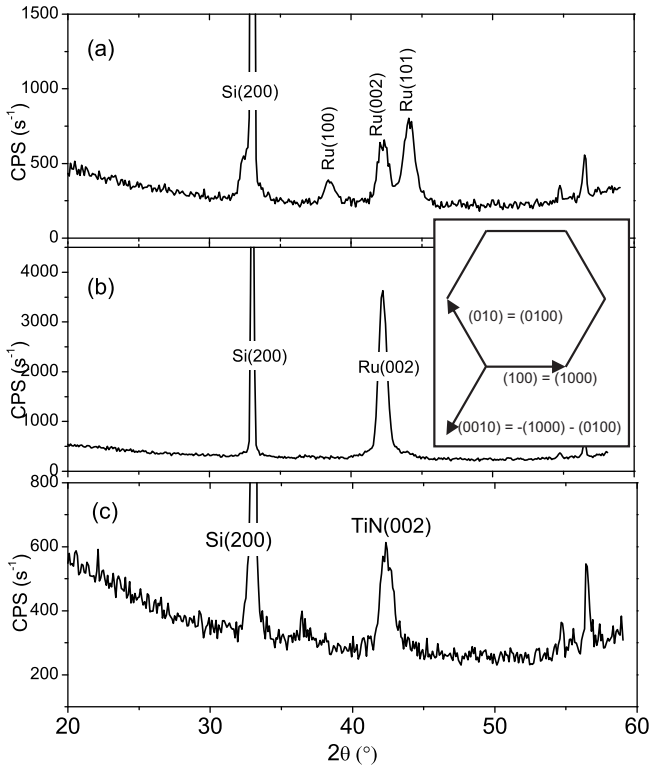

Figure 10.2: XRD spectra of as-deposited ALD films. (a) Ru on Si(100), (b) Ru/TiN/Si(100), (c) TiN/Si(100). The Ru film deposited directly on silicon has randomly oriented grains, while (b) is preferentially oriented. The inset shows the equivalence of the notation for the crystal orientation with three and four indices. The orientation perpendicularly out of the plane is (001) = (0001).

precursor	substrate	T_{dep} (°C)	gas	plasma power (W)	orientation	reference
DER	Si	280	O_2	-	(100), (002), (101)	[157]
DER	SiO_2	280	O_2	-	(002), (101)	[157]
DER	TiN	280	O_2	-	(002), (101), (102)	[157]
DER	TiO_2	280	O_2	-	(101)	[157]
$Ru(Cp)_2$	Al_2O_3	300	O_2	-	(100), (002), (101)	[2]
$Ru(Cp)_2$	Al_2O_3	400	O_2	-	(002)	[2]
$Ru(thd)_3$	Al_2O_3	450	O_2	-	(100), (002), (101)	[3]
$Ru(EtCp)_2$	TaN	200	NH_3	300	no clear XRD peaks	[355]
$Ru(EtCp)_2$	TaN	270	NH_3	300	(002)	[355]
$Ru(EtCp)_2$	TiN	270	NH_3	100	(002), (101), (102)	[181]
$Ru(EtCp)_2$	TiN	350	NH_3	500	(002)	this work
$Ru(EtCp)_2$	Si	350	NH_3	500	(100), (002), (101)	this work

Table 10.1: Comparison of the orientation of as-deposited ALD Ru films. DER stands for 2,4-(dimethylpentadienyl)(ethylcyclopentadienyl)Ru, $Ru(thd)_3$ for tris(2,2,6,6-tetramethyl-3,5-heptanedionato)Ru and $Ru(Cp)_2$ for ruthenium(II)di(cyclopentadienyl). Thermal processes are indicated by absence of plasma power.

temperature [2].

After annealing our samples under nitrogen at 800°C, the grains are preferentially out-of-plane oriented Ru (001), see figure 10.3(a-b). The arrows in the figure point to additional peaks symmetrically around the Bragg peak in the diffraction spectrum. These interference fringes are the result of interference of X-rays reflected from the bottom and top of the film, and indicate that the interface with the substrate and the surface of the film are very smooth [189]. Comparing figure 10.3(c) with figure 10.2(c) shows that the RTP treatment on 20 nm ALD TiN has no clear effect on the crystallinity of the TiN film.

Electron backscatter diffraction is a local method to probe the texture of thin films. For the as-deposited films, the grains were too small to make EBSD measurements. In the annealed Ru film on Si (figure 10.4(a)) however, individual grains can be distinguished. The pole figures of figure 10.4(b) indicate that the grains have a (001) fiber texture.

As a last method to visualize the microstructure of the films we used TEM (figure 10.5). The as-deposited film consists of a continuous layer of small grains with a diameter of about 10 nm. The anneal leads to grain growth, resulting in hexagonal grains that are much wider than they are thick. Some are even several hundreds of nm wide.

There are two driving forces for the observed grain growth in the film resulting in large Ru (001) grains: the grain boundary and surface energy. The deposition starts from many randomly oriented nuclei [367]. Subsequent growth from these

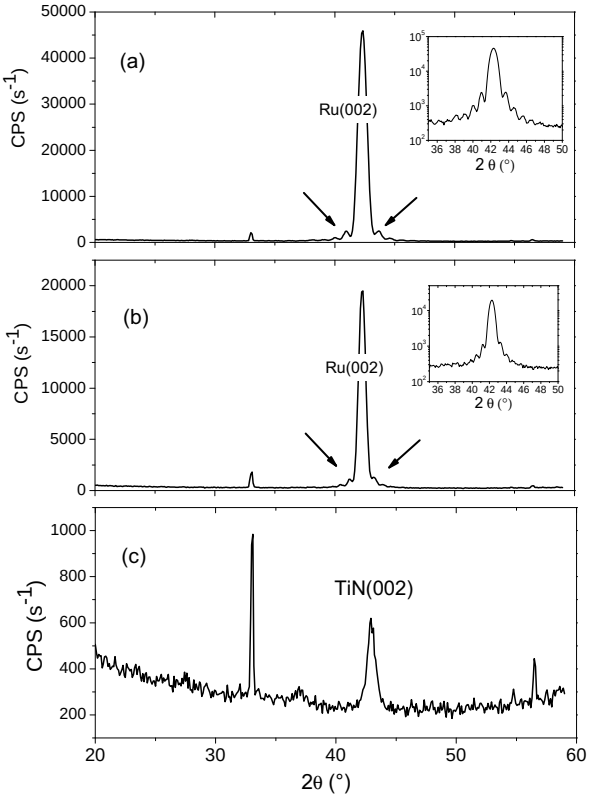

Figure 10.3: XRD spectra after RTP annealing (60 s at 800°C, under N_2 flow) of ALD films. (a) Ru on Si(100), (b) Ru/TiN/Si(100), (c) TiN/Si(100). Insets in (a) and (b) show the interference fringes on a logarithmic scale.

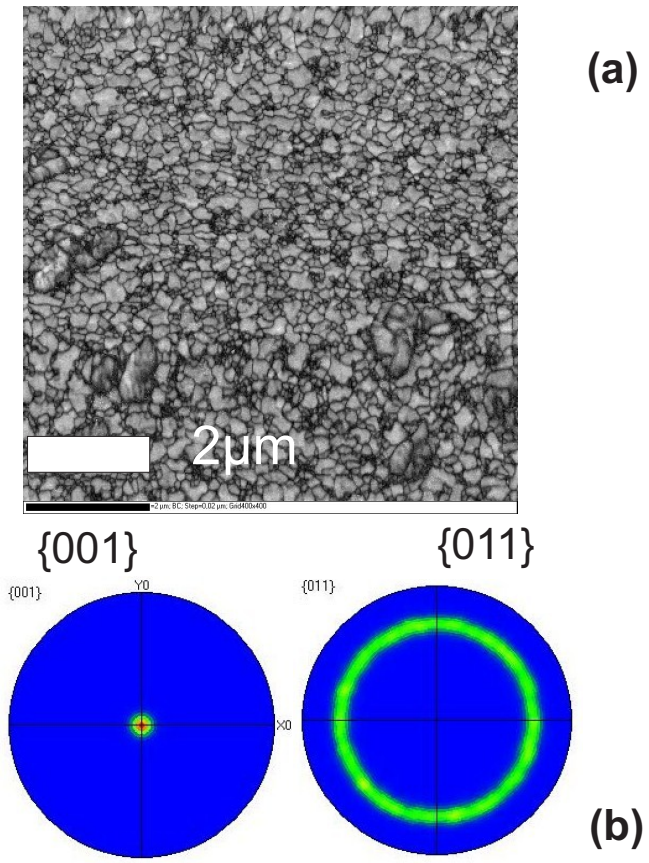

Figure 10.4: (a) SEM picture of annealed film. (b) EBSD pole figures of the annealed Ru film on Si(100). The peak in the center of the left pole figure shows the (001) orientation of Ru, while the other figure indicates that there is no preferential in-plane orientation.

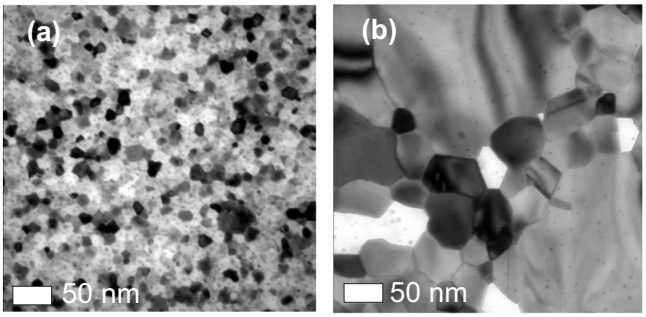

Figure 10.5: TEM of Ru on Si_3N_4. (a) As-deposited, small grains, (b) large hexagonal grains after anneal. TEM pictures made in bright field mode with magnification 230 000x.

nuclei results in a film composed of small grains. This film has a large density of grain boundaries, resulting in a high total grain boundary energy [333]. This energy can be lowered by the growth of larger grains. Secondly, since the surface energy of the (001) oriented grains is lower than other orientations [181] [151], Ru (001) grains grow at the expense of other orientations during the annealing process.

10.4 (Absence of) ruthenium silicide

Apart from the observed microstructural evolution, it was expected that Ru_2Si_3 would be formed upon annealing the Ru/Si(100) films [255]. However, no such silicide was detected (figure 10.3(a)). In order to investigate this further, we sputter deposited Ru on HF cleaned Si(100). The as-deposited film had randomly oriented grains (figure 10.6(a)), while the film reacted with the Si wafer to Ru_2Si_3 (figure 10.6(b)) during RTP anneal at 800°C.

Because Ru only starts being deposited in the ammonia plasma enhanced ALD process after about 80 cycles (figure 10.1), it was suspected that the interaction of the plasma with the substrate would be responsible for the absence of silicide formation upon annealing. Therefore, we subjected a piece of HF cleaned Si(100) to 50 cycles of ammonia plasma and then sputtered a Ru film onto it. Next, the sample was annealed under N_2 at 800°C. Indeed, the XRD pattern of the annealed sample (figure 10.6(c)) only has components due to metallic Ru, without silicide. To investigate the nature of the reaction barrier, XPS was performed on the NH_3 plasma treated silicon (figure 10.7). Nitrogen and oxygen are bound to the surface. Oxygen probably comes from residual water adsorbed on the vacuum chamber walls. The carbon on the surface is due to the contact with air during the transport of the sample to the XPS. The high resolution Si2p peak shown as an inset in figure

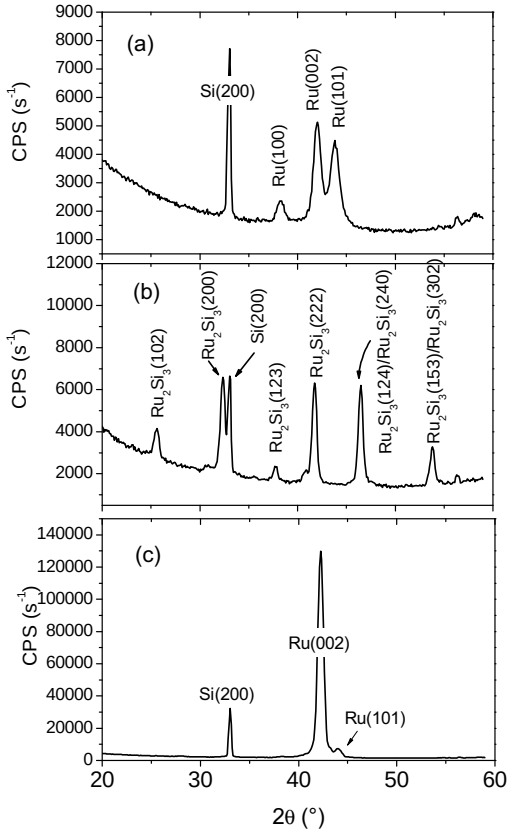

Figure 10.6: XRD spectra of Ru sputtered on HF cleaned Si(100) (a) as-deposited, (b) after anneal to 800°C, (c) film deposited on NH_3 plasma exposed substrate (see text), after anneal to 800°C.

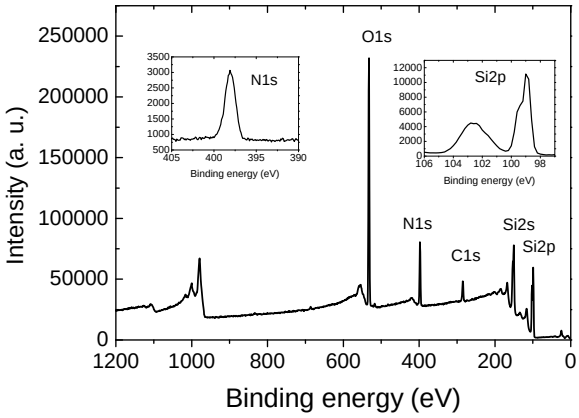

Figure 10.7: XPS scan of HF cleaned Si(100) surface after exposure to 50 cycles of NH_3 plasma. Insets show high resolution spectra of N1s and Si2p.

10.7 has two contributions: the maximum around 103 eV results from Si bound to N and O, while the maximum around 99 eV is characteristic of pure Si. Since the information depth of XPS is 1-2 nm, the presence of 'metallic' Si demonstrates that the plasma only created a silicon oxynitride layer of less than one nm.

The formation of a nitride interface has also been observed for ammonia plasma enhanced ALD of cobalt on silicon [188]. The 1 to 3 nm thick silicon nitride retarded formation of cobalt disilicide during annealing. At 800°C, the silicon nitride layer mediated the epitaxial growth of $CoSi_2$ (100) on the Si(001) substrate. The cobalt disilicide was formed by diffusion of Co through the interface into the substrate. No strong metallic Co XRD peaks comparable to the Ru(002) in this work were reported before $CoSi_2$ formation.

10.5 Conclusions

Ruthenium films were grown from $Ru(EtCp)_2$ and NH_3 plasma on Si(100) and ALD TiN. The as-deposited films on Si(100) were polycrystalline, on TiN they were (002) oriented. After annealing at 800°C for 60 s, grain growth resulted in smooth Ru films with a strong (002) texture. Electron backscatter diffraction (EBSD) and transmission electron microscopy (TEM) demonstrated that the lateral grain size of the annealed films was several 100 nm, which was large compared to the 10 nm thickness of the films. No ruthenium silicide was formed by annealing the ALD Ru films on Si(100). Comparison with sputter deposited films learned

that this occurred because the ammonia plasma created a SiO_xN_y reaction barrier layer prior to film growth.

11

Thermal and PE ALD onto fibrous materials

11.1 Introduction

Besides the obvious clothing industry, fiber based products are found in a range of markets as diverse as interior decoration (carpets), geo-engineering (river bank reinforcement), maritime technology (ship ropes), waste purification/processing (filters), sports (artificial turf), aerospace (composite materials)...

The reason textile materials are so widespread is that they can combine several intrinsic properties that make them valuable, such as being flexible, strong, having light weight, a large surface to volume ratio, good touch, softness, etc. Because of this, they are excellent for imparting additional functionalities. Dyeing, changing the wettability, improving the printability or fire retardation of certain textiles can increase their commercial value. Some other examples are protection from ultra violet (UV) radiation [306], prevention of the growth of bacteria [364] [331] and fungi, or rendering the textile conductive and hence antistatic [345]. Coating is a crucial method for adding value in this way [314].

The standard method for the application of coatings is by 'wet chemical techniques', where the fabrics are submerged in baths with solvents. This is an economically scalable technology, which nevertheless has some drawbacks. Drying of wet textile consumes a lot of energy and the solvents can be dangerous to people or the environment [314]. Therefore, other surface finishing techniques have been investigated. Examples include plasma treatment [48] [29], physical vapor

deposition (PVD) [345] and chemical vapor deposition (CVD) [331].

Considering the above, exploring ALD on textiles is a natural evolution. Because many fibers are made from heat-sensitive organic materials (natural or artificial polymers), PE ALD is of particular interest to allow a lower deposition temperature.

11.2 Literature

A number of research groups have demonstrated the feasibility of ALD on diverse fibrous materials. Fibers of wool [236], cotton [123] [125], polyester [302], poly(vinyl alcohol) [254], polypropylene [125] [327], steel [142] and paper [139] have been used as substrates for atomic layer deposition of alumina or titania. Most of these fibers can be used as sacrificial templates: after removing the substrate, a hollow metalorganic tube remains. The process is illustrated in figure 11.1(c). Figure 11.1(a, b) shows examples of these hollow tubes.

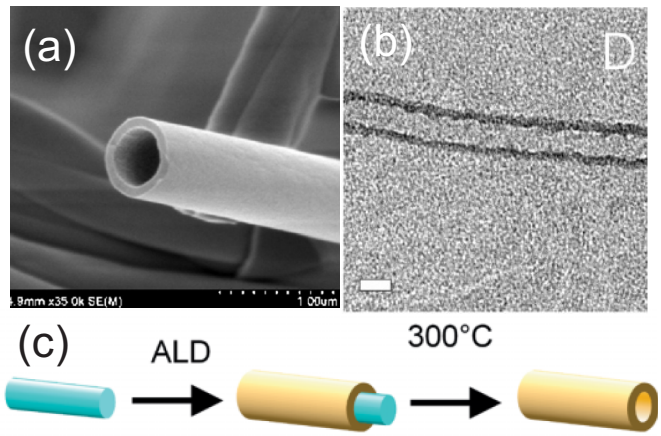

Figure 11.1: Hollow alumina tubes by using polymer fibers as templates. (a) Taken from [195], (b) and (c) taken from [286].

It is remarkable that ALD is possible on such a diverse range of substrates. As discussed in chapter 2, specific nucleation sites are required for the ALD surface reactions. For TMA, OH groups on the surface are needed. Figure 11.2(a) shows that cellulosis has plenty of such hydroxyl groups. Materials like polypropylene (PP) (figure 11.2(b)) or PMMA (figure 11.2(c)) do not offer such sites. However, ALD of Al_2O_3 from TMA and H_2O has been reported on PP and PMMA as well.

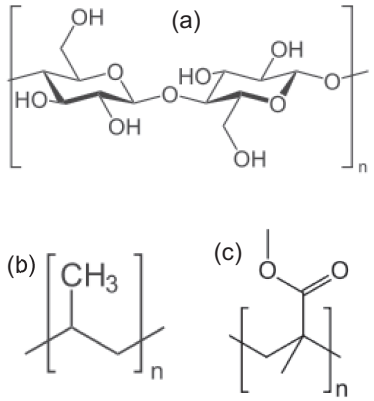

Figure 11.2: Sketch of monomer unit in polymers of cellulosis (a), polypropylene (b) and PMMA (c). Figures taken from Wikipedia.

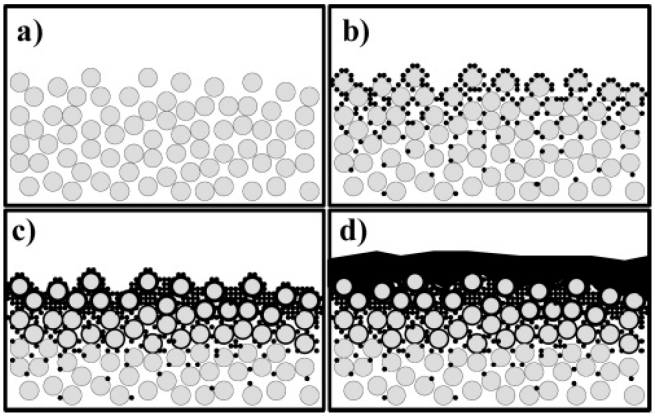

Figure 11.3: Proposed mechanism for ALD on polymers. Cross section of polymer represented by loosely packed circles (a), alumina nucleation clusters forming from H_2O reacting with TMA trapped in the near surface region (b), coalescence of alumina clusters and closure of space between polymer chains (c) and formation of a dense Al_2O_3 film that grows on top of the polymer surface (d). Taken from [348].

To explain this phenomenon, Wilson et al. [348] proposed a mechanism, which is illustrated in figure 11.3. Using QCM, they measured that TMA is absorbed by the polymers during the precursor pulse. During subsequent evacuation, some TMA stays trapped in the polymer. In the water pulse, H_2O reacts with the TMA near the polymer surface. This process creates small alumina clusters in the substrate. Upon further ALD growth, these clusters coalesce and a continuous film is

formed on the polymer. This model is able to account for the growth of alumina despite the absence of nucleation sites.

The group of Parsons at North Carolina State University have systematically studied the effect of ALD films on the wettability of textiles[1]. An example is shown in figure 11.4. At a deposition temperature of 60°C, the number of ALD cycles had a strong effect on the wettability of the substrate.

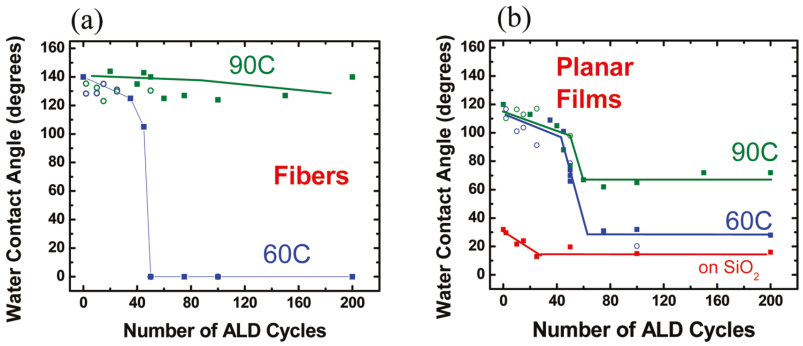

Figure 11.4: Wettability of polypropylene fibers (a) and films (b) as a function of the number of ALD alumina cycles at 60°C and 90°C. Taken from [125].

11.3 Nonwoven polyester: systematic study of ALD conformality on fibrous materials

Non-woven fabrics are a type of textile substrate that are used in a wide variety of applications, e. g. cleaning cloths, wipes, filters, disposable gowns and drapes, insulating materials (both thermal and acoustical) and many others.

In order to relate the coverage of the non-woven to ALD process parameters (pressure, exposure time...) and substrate geometry, a one dimensional (1D) test structure is now introduced and tested experimentally.

11.3.1 Model description

11.3.1.1 Diffusion and reaction based transport: transmission, reflection and loss

The substrate is modeled to be one dimensional, with precursors entering through one side. The substrate is divided into N identical cells by virtual planes (figure

[1]Engineering the wettability of materials has a long tradition, and relies on modifying the chemical composition and the roughness of the surface [85]. For non-ALD examples of a hydrophobic treatment of fibers, see e. g. [47] [118].

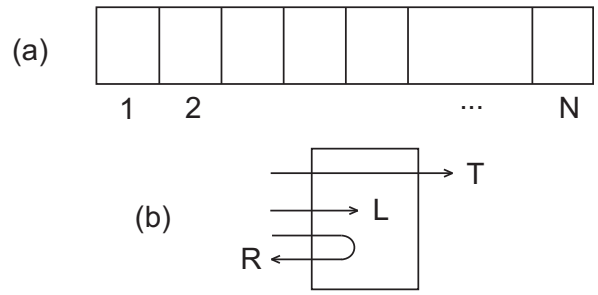

Figure 11.5: Basic concept of the one dimensional model. The substrate is divided into N identical cells; precursor molecules enter at cell 1 (a). For every cell, the precursor molecule can either be transmitted to the next cell, lost (chemisorbed) or reflected back to the previous cell (b).

11.5(a)). The cells are only distinguished by their place in the substrate and by their coverage. **It is our aim to calculate the depth profile of the ALD film: the coverage as a function of depth in the porous/fibrous substrate.**

The macroscopic transport through a cell of the substrate can be described by three numbers: the transmission probability T, the loss probability L and the reflection probability R. Loss of precursor means that the precursor has been chemisorbed, resulting in atomic layer deposition. In case of PE ALD, loss can also be caused by the recombination of radicals. The concept is represented schematically in figure 11.5(b).

Conservation of mass results in

$$T + L + R = 1. \tag{11.1}$$

The values of T, L and R for ALD depend on the geometry of the substrate, and the chemistry of precursor and substrate. What is developed next is a set of relations that link microscopic (molecular) phenomena with the macroscopic transport.

The loss probability L in a given cell is given by the product of the collision probability with the substrate surface P_c and the sticking probability P_s in the cell:

$$L = P_c \times P_s. \tag{11.2}$$

When a precursor molecule collides with the substrate in a cell and does not react with the substrate, we assume it has a 50 % probability of reflecting back to the previous cell:

$$R = 1/2 \times [P_c \times (1 - P_s)]. \tag{11.3}$$

Note that we neglect the possibility of multiple collisions within a cell, justified by taking sufficiently small cells. The transmission probability is given by

$$T = 1 - P_c + 1/2 \times [P_c \times (1 - P_s)]. \tag{11.4}$$

The first two terms on the right hand side represent the flux of precursors going through the cell without interaction, while the last term is the chance of being scattered forward.

The next step is to relate the collision probabilities P_c and sticking probability P_s with the substrate geometry and precursor chemistry.

11.3.1.2 Calculation of P_c

Intuitively, P_c will be low when the surface area of the substrate in a cell (A_{cell}) is small compared to the surface area of the opening ($A_{opening}$). When A_{cell} / $A_{opening}$ is high, P_c will approach 1. This argument is made more quantitative below.

In general, the interaction probability of a particle moving through a homogeneous medium is given by

$$P_c = 1 - e^{-\frac{x}{\lambda}}, \tag{11.5}$$

where x stands for the distance travelled and λ is the mean free path. When the medium is composed of particles with a density n and a scattering cross section σ, the mean free path can be calculated as

$$\lambda = 1/n\sigma. \tag{11.6}$$

It is assumed that the particles in the medium are at rest, and the moving particle is small.

Figure 11.6 shows that for fibers with radius r and length l, where l $>>$ r, the cross section should be calculated as 2 r l cos α, averaged over the angle α (because the particles move in random directions). We find that

$$\sigma = 2rl \left[2/\pi \int_0^{\pi/2} cos\alpha d\alpha \right] = \frac{4}{\pi} rl. \tag{11.7}$$

The area of a single fiber (neglecting the ends) is A_{fiber} = 2 π r l, the volume of a single fiber is V_{fiber} = π r^2 l = A_{fiber} r/2. The volume V of a cavity with opening area $A_{opening}$ and depth D (constant cross section, depth perpendicular to the opening) is V = $A_{opening}$ $\times$ D. The number of fibers is given by the total volume occupied by the fibers $V_{fiber,total}$ divided by the volume of a single fiber V_{fiber}. The density of fibers, n, is given by the total number of fibers divided by the cavity volume:

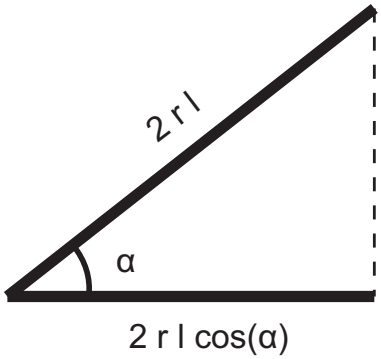

Figure 11.6: Effective cross section of a fiber with radius r and length l for a particle moving in vertical direction.

$$n = \frac{V_{fiber,total}/V_{fiber}}{V} \tag{11.8}$$

Based on the previous discussion, the surface area ($A_{fiber,total}$) of the combined fibers in the cavity is related to the total volume of the fibers by $A_{fiber,total}$ = $V_{fiber,total} \times$ 2/r.

The mean free path of precursor molecules moving in a nonwoven consisting of fibers with radius and length l can now be calculated as

$$\lambda = \frac{1}{n\sigma} = \frac{VV_{fiber}}{V_{fiber,total}} \frac{\pi}{4rl} \tag{11.9}$$

$$\lambda = \frac{A_{opening} D\pi r^2 l}{A_{fiber,total} r/2} \frac{\pi}{4rl} \tag{11.10}$$

$$\lambda = \frac{\pi^2}{2} \frac{A_{opening}}{A_{fiber,total}} D \tag{11.11}$$

It should be realized that this value of the mean free path is for three dimensions. In a one dimensional model, the effective mean free path is a factor $\sqrt{3}$ shorter.

During the crossing of a cell in the one dimensional model, the precursor moves a distance x = D/N. As a result, the collision probability in a cell is calculated as

$$P_c = 1 - e^{-x/\lambda} = 1 - e^{-\frac{2\sqrt{3}}{\pi^2 N} \frac{A_{fiber,total}}{A_{opening}}} = 1 - e^{-\frac{2\sqrt{3}}{\pi^2} \frac{A_{cell}}{A_{opening}}}. \tag{11.12}$$

By focusing on the area of the opening and the internal surface area, it is clear that similar derivations could be done for homogeneous media other than fibrous materials. Only the factor before the ratio $A_{cell}/A_{opening}$ will change.

11.3.1.3 Calculation of P_s

Atomic layer deposition is a self limiting deposition technique. When a surface is covered with chemisorbed precursors, no further precursor deposition occurs. Therefore, the sticking probability is modeled as (see chapter 2)

$$P_s = S_0(1-\theta), \tag{11.13}$$

where θ is the surface coverage of a cell, measured in monolayers of chemisorbed precursor and S_0 is the sticking coefficient (= the probability that a precursor molecule hitting a surface with θ = 0 chemisorbs onto it).

11.3.1.4 Number of particles entering the opening

The flux J of particles falling onto a surface area per time can be calculated by [94]

$$J = \frac{P}{\sqrt{2\pi m k_B T}} \tag{11.14}$$

with P, m and T the precursor pressure, molecule mass and temperature, respectively and k_B the Boltzmann constant.

The total number of particles entering the opening is simulated as follows. A homogeneous substrate has a surface density σ of 'useful' reactive sites, i.e. chemical groups accessible for precursor chemisorption in one ALD precursor pulse. The total number of reactive sites of a cell is reduced to an arbitrary number N_{max} in the program, typically 500. The total number of molecules entering the opening of the structure in the program then is

$$N_{opening} = JtA_{opening}N_{max}/(\sigma A_{cell}) \tag{11.15}$$

That is, we reduce the total physical reactive sites (in the order of 10^{14}/cm^2) to 500. Whether a precursor molecule is lost, reflected or transmitted is determined by a simple Monte Carlo approach [52]:

A random number rn between 0 and 1 is generated.

If rn $<$ L, the precursor is lost.

Else if rn $>$ (1 - T), the molecule is transmitted to the next cell.

Else, the molecule is reflected back: its direction is reversed and it moves back to the previous cell.

When a particle is lost (chemisorbed or recombined) or leaves the substrate, a new particle is followed that moves into the 1D substrate.

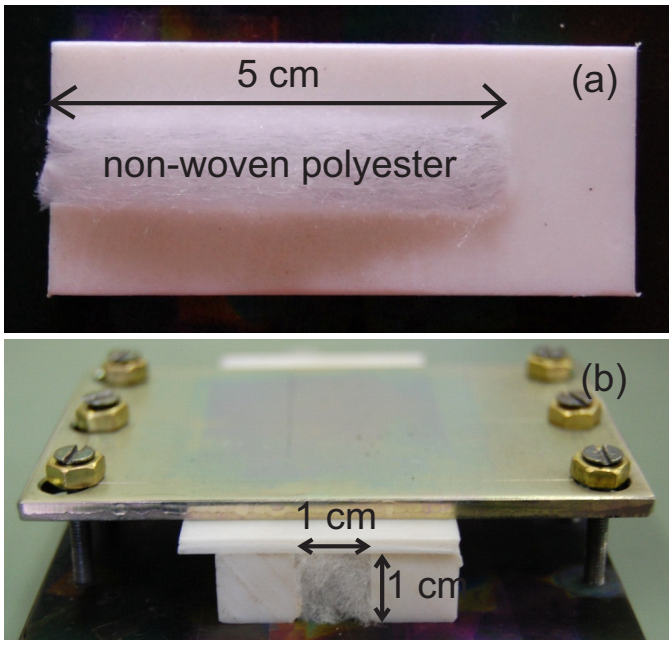

Figure 11.7: Experimental test structure to study the conformality of ALD on porous materials.

11.3.2 Experimental setup

To test the model proposed above, a 1 cm $\times$ 1 cm $\times$ 5 cm square hole was machined in Teflon (figure 11.7). The hole is filled with non-woven polyester (mass density of 1.15 g/cm^3). The structure is clamped between the substrate holder and a piece of flat Teflon on top, so that the precursor can only enter the nonwoven from one side. The setup is similar to the one used by Dendooven et al. [51] [52] who studied the conformality of ALD inside hollow macroscopic test structures.

11.3.3 Model parameter values

The fibers (figure 11.8) are modeled as cylinders with length l, mass density ρ_{fiber} and radius r. The total volume $V_{fiber,total}$ of the fibers in the nonwoven is given by

$$V_{fiber,total} = \pi r^2 l = \frac{(2\pi rl)r}{2} \approx A_{fiber,total} \cdot \frac{r}{2}, \tag{11.16}$$

where $A_{fiber,total}$ denotes the surface area of the fibers when the small area of the top and bottom of the cylinders is neglected. $V_{fiber,total}$ is related to the mass $m_{fiber,total}$ of the nonwoven by $V = \frac{m_{fiber,total}}{\rho_{fiber}}$. For the 'high fiber density'

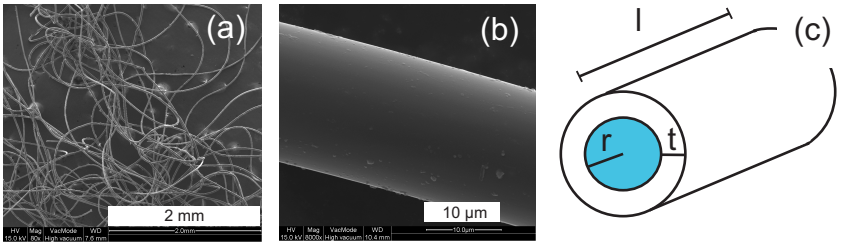

Figure 11.8: (a) SEM of fibers in nonwoven, (b) zoomed on single fiber, (c) schematic representation of fiber (radius r and length l) with ALD coating (thickness t).

nonwoven used in this study, using $m_{fiber,total}$ = 0.32 g, a volume of 0.28 cm^3 and a surface area of 700 cm^2 is calculated. Figure 11.8(b) shows that r $\approx$ 8 μm. As a reference, the internal surface area of the empty test structure is 4 $\cdot$ 5 cm^2 + 1 cm^2 = 21 cm^2. The low density nonwoven was made of the same fibers, but only had a mass of 0.14 g. This corresponds to a surface area of 300 cm^2. Because of the small ALD film thickness (see below), the surface area of the substrate does not change appreciably as a function of the number of ALD cycles.

The ideal surface density σ of Al_2O_3 is $\sigma = (\frac{\rho_{Al_2O_3}}{M_{Al_2O_3}} N_A)^{2/3}$ = 8.2 $\cdot$ 10^{14}/cm^3, with $\rho_{Al_2O_3}$ the mass density (3.97 g/cm^3) and $M_{Al_2O_3}$ the molar mass (109 g/-mole) of alumina, and N_A Avogadro's constant. The ideal growth per ALD cycle (GPC) is $(\frac{\rho_{Al_2O_3}}{M_{Al_2O_3}} N_A)^{-1/3}$ = 3.5 Å (one monolayer of molecular alumina). However, experimentally we found a GPC of 0.65 Å for thermal ALD at 75°C (measured on a planar sample). Furthermore, 2 Al are needed for the deposition of Al_2O_3. As a result, the surface density in our experiments was estimated as $\sigma = 2 \cdot \frac{0.65}{3.5} \cdot 8.2 \cdot 10^{14}/cm^2 = 3.0 \cdot 10^{14}/cm^2$.

Table 11.1 summarizes the parameters used in the simulations.

	Parameter	Value
	ρ_{fiber}	1.15 g/cm^3
	r	8 μm
high fiber density substrate	$m_{fiber,total}$	0.32 g
	$V_{fiber,total}$	0.28 cm^3
	$l_{fiber,total}$	1400 m
	$A_{fiber,total}$	700 cm^2
low fiber density substrate	$m_{fiber,total}$	0.14 g
	$V_{fiber,total}$	0.12 cm^3
	$l_{fiber,total}$	610 m
	$A_{fiber,total}$	300 cm^2

Table 11.1: Parameters of nonwoven, used for simulations.

11.3.4 Results

11.3.4.1 Optimizing program

It is first tested how many virtual cells the substrate should be divided in, so that the simulated coverage profile does not depend on this choice. For the high density substrate (area of cavity walls and fibers combined = 720 cm^2), the simulations converge to the same profile with increasing number of cells. A small number of cells results in the prediction of deeper penetration into the nonwoven (figure 11.9). For all following simulations, 500 cells were used.

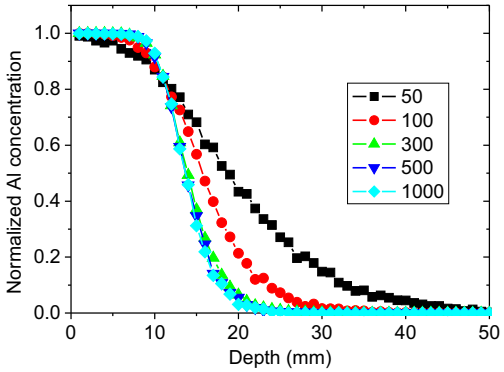

Figure 11.9: Influence of the number of cells on the simulated coverage profile. Standard conditions used.

Knowledge of the sticking coefficient S_0 is needed for the model (equation 11.13). This was estimated by running simulations with a deposition time of 8 s with different values of S_0 (figure 11.10) and comparing the coverage profile to the experiment (figure 11.11). Reasonable agreement was obtained for S_0 = 0.01. Like ALD in pores [51] [297], a higher S_0 results in a steeper interface between coated and non-coated substrate.

S_0 depends on the chemistry of precursor and substrate and deposition temperature (cfr. Chapter 2). It has been reported that S_0 = 0.1 for TMA gave a good agreement with experiments in rectangular holes at a deposition temperature of 200°C [51]. However, in the present work, the deposition temperature is just 75°C, possibly resulting in a lower reactivity of TMA with the surface.

11.3.4.2 Influence of deposition time and substrate density on coverage profile

Figure 11.11 shows the experimental coverage profile on the high density nonwoven for TMA pulse lengths of 2 s, 8 s and 30 s. The error bars indicate standard

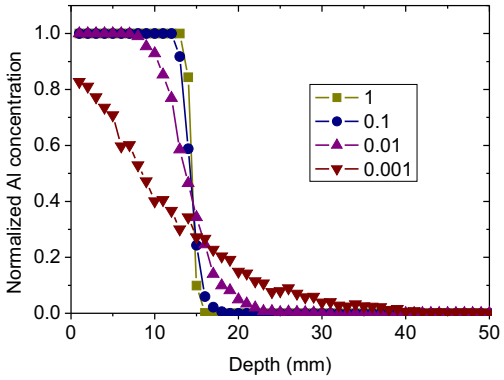

Figure 11.10: Influence of the sticking coefficient S_0 on the simulated coverage profile.

Parameter	Symbol	Value
Precursor pressure	P	0.08 Pa
Precursor temperature	T	75°C [a]
Exposure time	t	8 s
Mass TMA	m	$1.2 \cdot 10^{-25}$ kg [b]
Initial sticking coefficient	S_0	0.01
Precursor flux	J	$1.33 \cdot 10^{17}$ cm^{-2} s^{-1}
Surface density	σ	$3.0 \cdot 10^{14}$ cm^{-2}
Area of walls + fibers (HD)	$A_{internal}$	720 cm^2
Area of walls + fibers (LD)	$A_{internal}$	320 cm^2
Area of opening	$A_{opening}$	1 cm^2
Number of cells	N_{layers}	500
Number of sites per cell in simulation	N_{max}	500
Number of reactive sites on HD	$\sigma \cdot A_{internal}$	$2.16 \cdot 10^{17}$
Number of reactive sites on LD	$\sigma \cdot A_{internal}$	$9.6 \cdot 10^{16}$
Number of molecules entering structure	$J \cdot t \cdot A_{opening}$	$1.06 \cdot 10^{18}$

Table 11.2: Parameters used for 'standard simulation' and corresponding physical quantities. [a] Temperature estimated from reactor temperature. [b] Mass TMA = 72 atomic mass units. HD = high density nonwoven, LD = low density nonwoven.

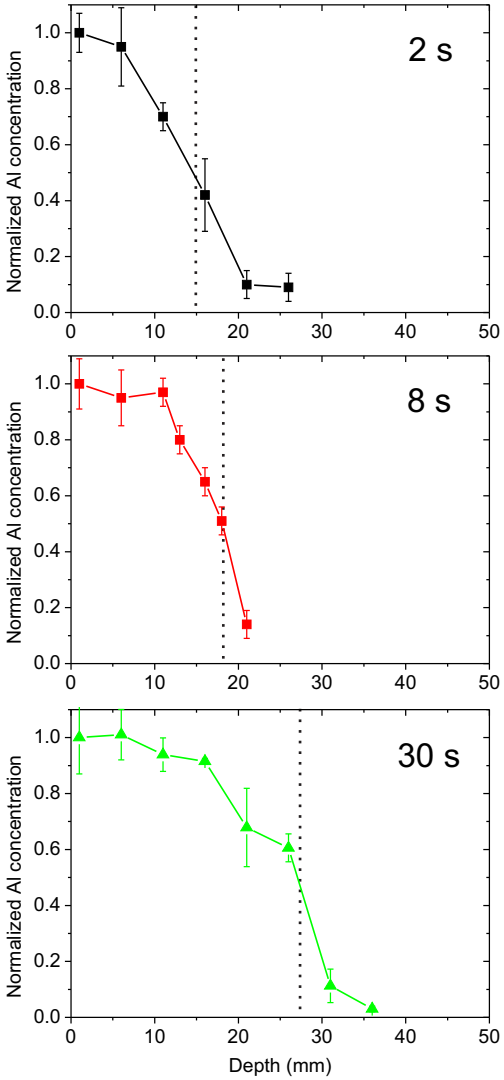

Figure 11.11: Experimental penetration of ALD alumina in non-woven structure as a function of TMA pulse time per cycle: 2 s, 8 s and 30 s. Dotted lines indicate depth at which the Al concentration is half that at the opening of the nonwoven.

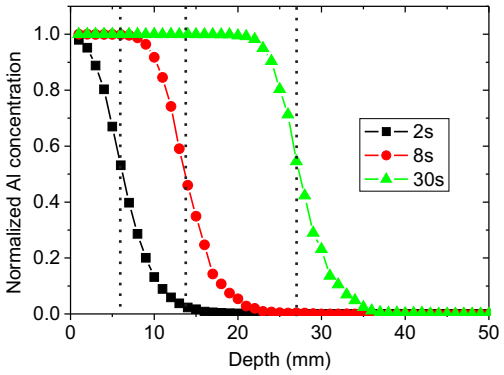

Figure 11.12: Simulated penetration of ALD alumina in non-woven structure as a function of TMA pulse time per cycle: 2 s, 8 s and 30 s. Dotted lines indicate depth at which the Al concentration is half that at the opening of the nonwoven.

deviations. The water pulse length was chosen sufficiently long (5 s, 15 s and 30 s) so that TMA was the depth limiting step. Figure 11.12 compares the simulated coverage profiles, using variables (except for deposition time) listed in table 11.2. Different runs of the same simulation resulted in almost identical profiles. As expected, increasing the deposition time t results in the growth of alumina deeper into the test structure. However, the experimental penetration depth from 2 s of TMA is deeper than the simulation. The simulation assumes a constant effective TMA pressure in the chamber during the pulse. However, in our reactor (figure 5.1) pressure builds up in the tube between the TMA bottle and the pneumatic valve on the reactor between pulses. When the valve opens, a transient higher pressure than 0.08 Pa is present in the reactor. As a result, more TMA than simulated enters the nonwoven, leading to a deeper coverage. Also the simulation for 8 s is slightly less deep than the experimental one. When the nonwoven density is not perfectly homogeneous throughout the structure, the coverage profile may deviate from the simulation.

Table 11.3 shows the simulated fraction of TMA entering the nonwoven that react with the nonwoven or leave the substrate without reaction. During the 8 s TMA pulse, $1.1 \cdot 10^{18}$ precursor molecules ($J \cdot A_{opening} \cdot t$) enter the 1 cm^2 opening (see Table 11.2). The number of reactive sites on the nonwoven in the structure ($\sigma \cdot A_{substrate}$) is $2.2 \cdot 10^{17}$. Almost five times the amount of TMA necessary to cover the entire substrate surface enters the hole during the precursor pulse. However, 94.5 % of the TMA is re-emitted from the test structure without chemisorption. Only a small number of the precursor molecules contribute to film growth. The rest diffuses out of the nonwoven, back into the reactor. For longer

S_0	t (s)	Out front (%)	Reacted (%)	$(J \cdot t \cdot A_{opening})/(\sigma \cdot A_{internal})$
0.01	2	90.1	9.9	1.2
0.01	8	94.5	5.5	4.9
0.01; LD	8	94.6	5.4	11.1
0.01	30	97.1	2.9	18.5
1	2	88.9	11.1	1.2
1	8	94.3	5.7	4.9
1	30	97.0	3.0	18.5

Table 11.3: Simulated fraction of TMA molecules entering the structure that react with the nonwoven (Reacted) and that leave without reaction (Out front). Variables (except for S_0) as in table 11.2, LD indicates low density nonwoven.

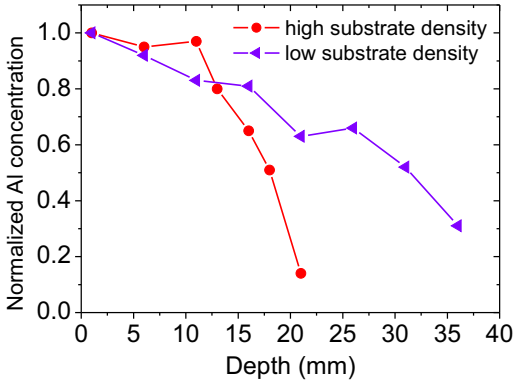

Figure 11.13: Relative ALD thickness for high and low density nonwoven.

pulse times, the fraction of consumed precursors is even lower. A higher reactivity (S_0) does not make much of a difference; the growth is diffusion limited [64].

The coverage profile in trenches with a high aspect ratio (AR) has a sharper edge (interface between covered and non covered surface) as a function of depth than holes with a lower AR [51]. Figure 11.13 compares the coverage profile of alumina on the high and low density nonwovens. For both depositions, the TMA pulse time was 8 s. Indeed, the ratio of internal and opening areas of porous materials acts as the equivalent for the AR in simple pores. The same qualitative behavior for the edge is observed: for the low density substrate, the edge is spread out in the depth. Figure 11.14 shows a simulation for an internal area of 720 cm^2 and 320 cm^2 and S_0 = 0.01. A better fit of the experimental profile on the low density substrate could be obtained by using S_0 = 0.003.

Note that although the coating reaches deeper into the low density substrate, this does not result in more coated fibers (see table 11.3). The deeper penetration is offset by the lower number of fibers, so lowering the density of the substrate

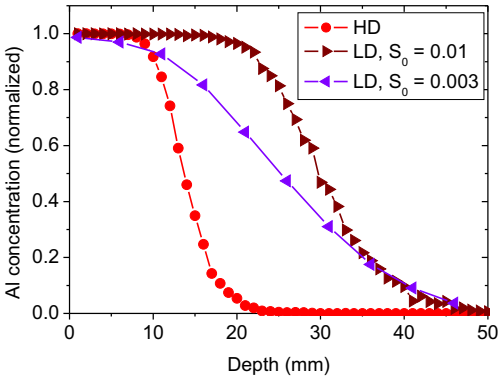

Figure 11.14: Simulated ALD thickness for high (HD) and low density (LD) nonwoven. When a lower sticking coefficient of 0.003 is used, the simulated profile better matches the experiment.

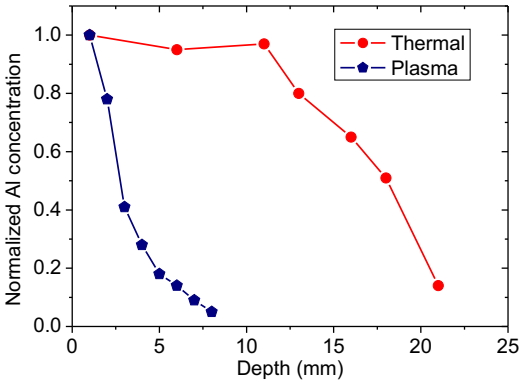

Figure 11.15: Relative ALD penetration for thermal and plasma enhanced ALD.

cannot be used to reduce deposition times at the same precursor pressure.

11.3.5 Model for PE ALD

Figure 11.15 shows the experimental depth profile of the alumina film into the nonwoven, deposited with thermal ALD and PE ALD. For both depositions, 8 s TMA and 8 s reactive gas were used. Clearly, the penetration depth of the coating deposited by PE ALD is much lower compared to thermal ALD.

When a radical collides with a surface, there is a recombination probability P_r (sometimes called recombination coefficient) that it will recombine with another oxygen radical to form non-reactive molecular O_2 [52]. The transport equations

Variable	Symbol	Value	Units
O pressure	P	0.06	Pa
O mass	m	$1.3 \cdot 10^{-26}$	kg
O temperature	T	75	°C
O flux	J	$3.0 \cdot 10^{17}$	$cm^{-2}\ s^{-1}$
Deposition time	t	8	s
Surface density	σ	$1 \cdot 10^{15}$	cm^{-2}
Sticking coefficient	S_0	0.1	-
Area fibers + walls	$A_{substrate}$	720	cm^2

Table 11.4: Standard conditions used in simulations of PE ALD

are modified to allow for recombination of radicals:

$$L = P_c \times (P_s + (1 - P_s) \times P_r) \tag{11.17}$$

$$R = 1/2 \times [P_c \times (1 - L)] \tag{11.18}$$

$$T = 1 - (L + R) \tag{11.19}$$

Simulations were ran using equations 11.17 - 11.19 for L, R and T and the variables listed in table 11.4. The RF plasma source results in a partial dissociation of O_2. Based on literature [98], a dissociation of 10 % and corresponding partial pressure of 0.06 Pa for oxygen radicals seems a realistic value for the oxygen pressure and plasma power used in this work. Before the plasma step, the surface is covered with methyl (CH_3) groups. The O radicals react with these in a combustion like fashion [109] [52]. Multiple O radicals are needed per methyl group. Therefore, a higher surface density σ compared to table 11.2 was chosen for the simulation. Because of the high reactivity of O radicals, a sticking coefficient S_0 of 0.1 was assumed[2].

The effect of surface recombination on the depth profile is shown in figure 11.16. The penetration into the nonwoven is severely reduced because of radical recombination. Comparison to the experiment (figure 11.15) shows that the simulated steepness of the interface between coated and non-coated nonwoven is too high. This may be related to the occurrence of a secondary thermal ALD reaction. Indeed, the combustion reaction produces H_2O, which can penetrate deeper into the nonwoven and result in thermal ALD [52]. The simulation taking into account some thermal ALD (PE + thermal) does match the experimental result.

Table 11.5 shows the simulated number of reacted, recombined and out diffused O radicals. It can be seen that a large fraction of the radicals entering the nonwoven recombine. Because of the self limiting nature of ALD (equation 11.13), radicals need to enter deeper into the substrate after coating the area closest to the

[2]It is assumed that the TMA pulse is sufficiently long in order to reach saturation.

RC	Out front (%)	Reacted (%)	Recombined (%)
0	93.2	6.8	0
0.01	84.9	2.3	12.8
0.1	59.4	1.0	39.6
0.5	23.6	0.4	76.0

Table 11.5: Simulated fraction of O radicals entering the structure that react with the nonwoven (Reacted), that leave through the front as radicals without reaction (Out front) and that recombine on the nonwoven (Recombined) for different values of the recombination coefficient (RC). Sticking coefficient was 0.1.

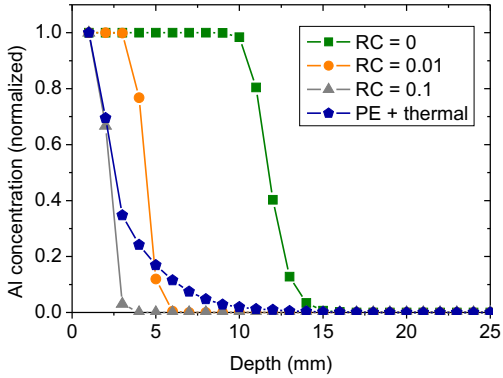

Figure 11.16: Simulated effect of the recombination coefficient (RC) on the penetration profile. The PE + thermal profile was calculated with the assumption of S_0 = 0.1 and RC = 0.2 for PE ALD and a 0.5 s water pulse (S_0 = 0.01) for simulating the simultaneous occurrence of thermal ALD caused by the H_2O generated during the combustion reactions. All other parameters where taken from the standard set as described in the tables.

substrate to contribute to deposition. However, recombination eliminates the radicals before they can reach unreacted ligands and contribute to the ALD process.

Due to radical recombination, increasing exposure of the nonwoven to O radicals (e. g. by increasing the plasma power or increasing the plasma pulse time) will not result in a significantly enhanced penetration of the coating.

11.4 Exploration of ALD on different fibrous materials

This part of the chapter about ALD on textiles gives an overview of unpublished experiments that explored the possibility of ALD on different types of fibrous materials. Films were atomic layer deposited on diverse fibrous substrates. The presence of the coating was demonstrated by a range of different techniques, from

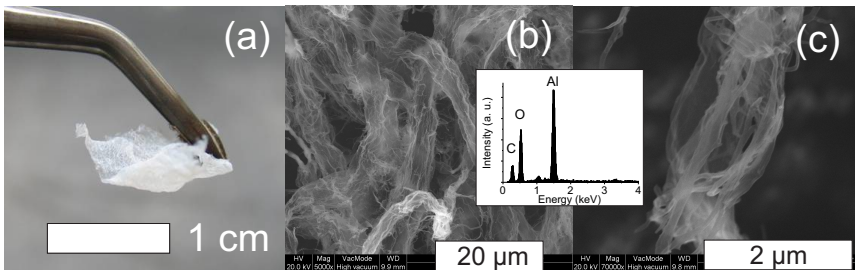

Figure 11.17: Fotograph (a) and SEM pictures (b), (c) of tissue paper coated with ALD after burning the substrate. The inset shows that the hollow fibers consist of alumina.

microscopic and spectroscopic methods to very easily detectable changes of the physical properties of the substrate. I want to thank Dr. Jan D'Haen for the TEM and some of the SEM pictures shown in this section. I. Lambrechts and M. Jans are acknowledged for the preparation of TEM slides with the ultramicrotome. Olivier Janssens and Koen De Keyser kindly made the other SEM and EDX pictures shown in this chapter. The textile samples were provided to us by Dr. Guy Buyle from Centexbel. Alfatex N.V. (Belgium) supplied the hook and loop fasteners. The work on tissue paper was mainly done by Dr. Davy Deduytsche.

11.4.1 Tissue paper: conformality and hydrophilicity

As a first fibrous substrate, tissue paper was used. Leskelä and Ritala and collaborators have grown TiO_2 on paper using ALD in order to make high surface area photocatalysts [139] [236]. Here, we deposit alumina (Al_2O_3) with thermal ALD, because it is a well-studied, easy to handle ALD process [275]. Furthermore, the GPC of thermal ALD of Al_2O_3 from TMA and H_2O is rather high, even at 75°C. Conformality of the Al_2O_3 ALD coating (200 cycles, 2 s TMA, 5 s H_2O) on the natural cellulose fibers of the tissue paper could be demonstrated by a very easy method. The paper was ignited with a lighter[3]. Without ALD coating, the paper fully burned away. Figure 11.17(a) shows that for alumina ALD coated paper, a network of white fibers was left behind. As shown in figure 11.17(b, c), SEM/EDX demonstrated that the fibers were composed of hollow alumina tubes of various diameters.

When water was dropped on untreated tissue paper, it was immediately absorbed (figure 11.18(a)). However, after the ALD of alumina (100 cycles, 2 s TMA, 5 s H_2O), the water formed droplets that stood on the surface (figure 11.18(b)).

Hyde et al. [123] observed the same change in wettability of cotton fibers upon ALD of alumina. The contact angle measured on treated cotton fabric was consid-

[3]Pictures and videos of the experiments are available at the website of the CoCooN research group: http://www.cocoon.ugent.be

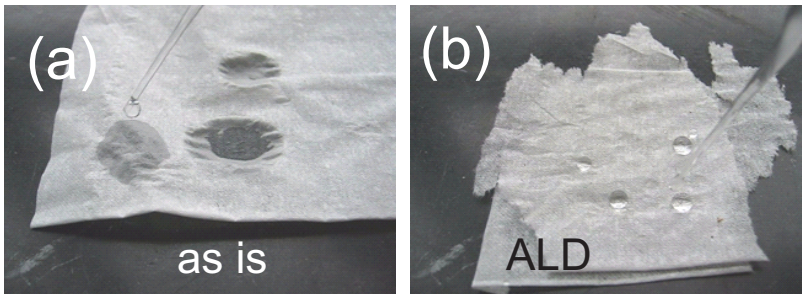

Figure 11.18: Drops on tissue paper: original (as is) (a) and coated with 100 cycles Al_2O_3 ALD (b).

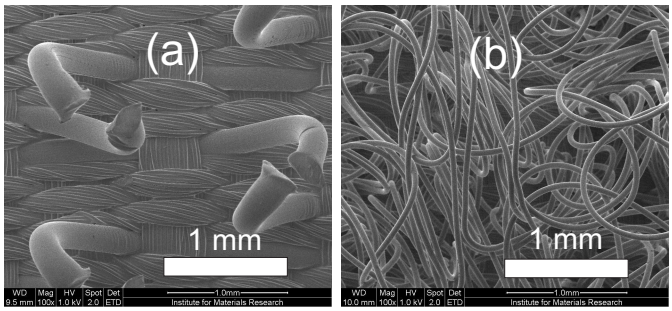

Figure 11.19: SEM of (a) hooks and (b) loops.

erably higher than on coated silicon samples. This was explained to be a consequence of the increase in rigidity of the cellulose fibers by the Al_2O_3 coating [123].

11.4.2 Polyamide hook and loop fasteners: conformality and hydrophylicity

Hook and loop fasteners are reversible closing means, often encountered on clothing or shoes and sometimes also referred to as 'velcro'. Al_2O_3 films (200 cycles, 2 s TMA, 5 s H_2O) were grown on the substrates (figure 11.19).

First, the conformality of the coating was investigated. The simple method of burning away the substrate employed for ALD on paper did not work for the artificial fibrous materials we tested. The plastic materials all shrank and resulted in an amorphous black residue. Therefore, the conformality of these textiles was investigated with other methods. The velcro loops were embedded in epoxy. Slices of about 0.1 m of the fibers and matrix were made (figure 11.20(a)) with a diamond knife in an ultramicrotome.

Figure 11.20(b) is a high angle annular dark field (HAADF) STEM image of an untreated loop in the epoxy. The difference in material densities results in a

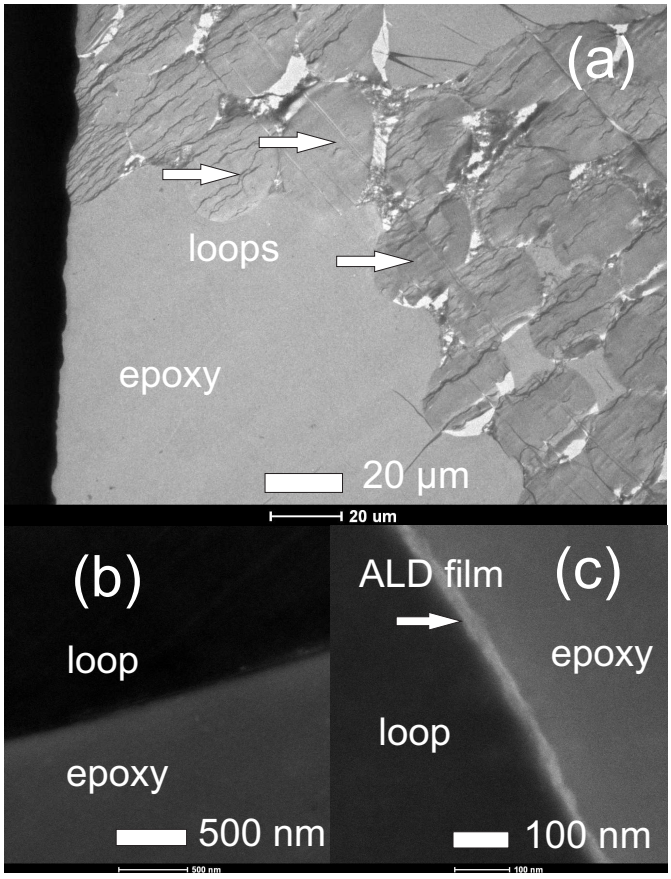

Figure 11.20: TEM of loops embedded in epoxy (a), uncoated loop (b) and loop with alumina film grown by 200 cycles thermal ALD (c).

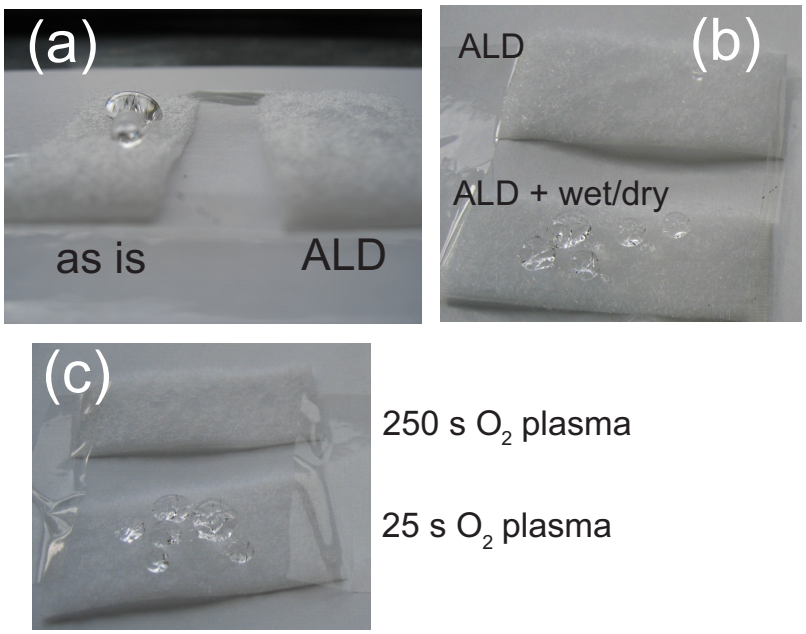

Figure 11.21: Hydrophilicity tests on loops without (as is) and with Al_2O_3 (a), drops on loops with ALD and with ALD after one wetting + drying cycle (b) and on plasma treated loops (c).

clear picture in the HAADF mode. In figure 2(c), an ALD alumina coating can be seen at the interface of loop and epoxy. The film follows the shape of the loop, and shows no cracks or other defects. TEM pictures of ALD Al_2O_3 on polyethylene particles [77] and on cotton fibers [123] have revealed that the films on these substrates are about 4 times thicker than films deposited on planar silicon wafers with the same process. This behavior has been explained by the presence of water in the substrate material, resulting in a CVD like reaction during the TMA pulse. In the present work, this problem does not occur. Indeed, the alumina on the fibers is about 20 nm thick, similar to ALD alumina on Si (15 nm).

As a second experiment, the influence of the ALD coating on the surface energy was assessed by the water drop test previously discussed for tissue paper. Figure 11.21(a) shows loops with and without ALD alumina, on which water was dropped with a pipette. Droplets stood on the surface of the untreated loops, whereas the water was immediately absorbed by the alumina coated loops. This behaviour is opposite to what was observed for tissue paper (figure 11.18).

The loops are much thicker than the paper fibers, as can be seen by comparing figures 11.20(a) and 11.17(c). The loops of the hook-and-loop fastener are made from hydrophobic polyamide. Alumina is much more hydrophylic [123]. There-

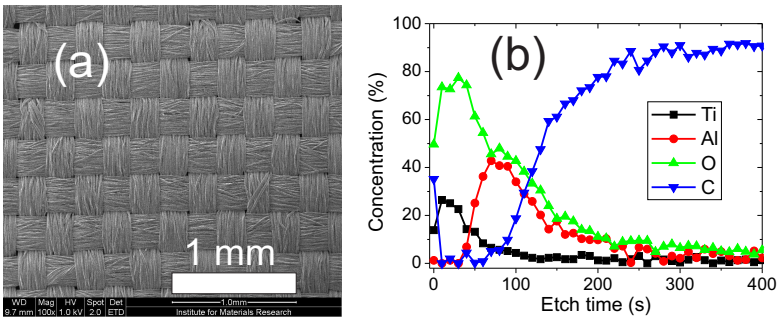

Figure 11.22: SEM of woven polyester (a) and XPS of TiO_2/Al_2O_3 on the polyester textile (b).

fore, it seems likely that the enhancement of wettability of the loops is a result of the surface material, rather than a change in mechanical properties of the fibers. After one or two wetting and drying cycles of the ALD treated loops, the loops became hydrophobic again (figure 11.21(b)). This might be because the water damages the coating, although we could not find evidence for this mechanism by TEM. An easier way to make the loops hydrophylic was by subjecting them for 250 s to pure oxygen plasma (0.3 Pa, 300 W) generated in the RF source (no ALD). The result is shown in figure 11.21(c). The loop fastener with plasma treatment remained hydrophylic for multiple wetting and drying cycles.

11.4.3 Woven polyester textile: XPS study

Non woven fibrous materials were studied above. However, most textiles consist of fibers woven into patterns. A simple polyester woven (density ca. 100 g/m^2, fiber diameter 10 m) was used for the experiments reported in this section (figure 11.22(a)). This type of fabric is commonly used, e. g. as material for protective workwear.

First, 10 nm Al_2O_3 (75 cycles, 2 s TMA, 5 s O_2) was deposited with PE ALD. Then, 10 nm of TiO_2 (250 cycles, 2 s TTIP, 5 s O_2) was deposited in the same reactor. Such a structure might be useful for photocatalysis or as UV-blocker [306]. The Al_2O_3 buffer layer can protect the substrate from attack by electron hole pairs produced by UV in the TiO_2.

Unlike EDX, XPS is surface sensitive (information depth of 1-2 nm), enabling the study of thin multilayer structures. Figure 11.22(b) shows the XPS depth profile of the woven sample with an alumina/titania bilayer. First, only Ti and O are found. This demonstrates that a pure titania coating fully covers the substrate. Deeper, the Ti content of the bilayer decreases and Al appears. However, titanium is still visible. This is because the woven fabric is not flat. While all Ti is etched

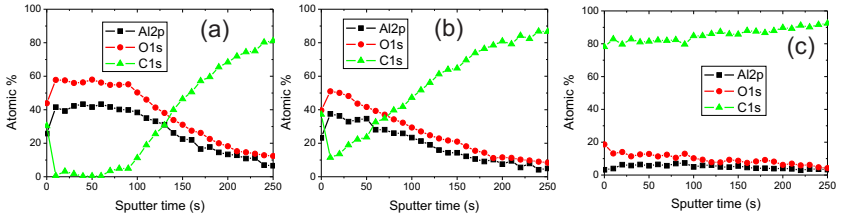

Figure 11.23: XPS depth profile of alumina on polyester: as deposited (a), after washing test (b) and after abrasion test (c).

away from the top of the fibers, the Ti at the sides is not. For the same reason, further etching shows that also the Al signal persists and does not exhibit a steep decline in concentration as a function of etching depth. At the end of the depth profile, the pure polyester fibers are measured. They consist of carbon and some oxygen.

Figure 11.23(a) shows the XPS depth profile of the woven polyester covered with 100 cycles of PE ALD alumina. At Centexbel, the Belgian research center for textiles, washing and wear tests were performed. Figure 11.23(b) shows that washing removes the alumina film from the top of the textile. Abrasion removes almost the entire coating (figure 11.23(c)). This shows that the use of ALD on products exposed to aggressive treatments will require special care to enhance the adhesion.

It is interesting to note that ALD Al_2O_3 and TiO_2 have been shown to adhere well to the polymers PMMA and PEEK [141] [135]. Specifically, Kemell et al. [141] comment that the ALD films on PTFE failed the Scotch tape test and this is likely because of different nucleation of ALD on the different polymers. On PMMA and PEEK, the precursors are chemically bonded to surface groups on the polymers. When ALD films adhere poorly, they suspect that nucleation occurs as described by Wilson et al. [348]. Like the figure shows, the precursor diffuses into the polymer substrate (note that the grey circles indicate individual polymer molecules, not fibers) and reacts with water trapped in the substrate. The film starts growing from separated nucleation sites that are not chemically bonded to the polymer. After a number of ALD cycles, the polymers at the outside of the substrate are surrounded by the ALD film. Because there are no chemical bonds between film and substrate, the adhesion is poor.

If this mechanism describes our ALD/polyester experiments, the possibility to coat heavy duty textiles with ALD should not be dismissed based on the XPS results. A long plasma exposure before ALD might introduce enough reactive sites in the polyester to enable a strong chemical bond between film and substrate.

11.5 Antibacterial ZnO on woven polyester/cotton blend

This work was performed in collaboration with Ilse Garez and Prof Marc Van Parys from University College Ghent (Hogeschool Gent).

ALD ZnO has been used as an antibacterial coating on a biological material (egg shell membrane) by the group of Knez [191]. However, they irradiated the samples with UV light (like TiO_2) to obtain the antimicrobial effect. Microorganisms living on the clothing of medical personnel and on other textiles used in hospitals can cause infection of patients [227]. To prevent the growth of bacteria or fungi on fabrics, researchers have treated them with anorganic materials like silver [364], copper [308], titanium dioxide [331] and zinc oxide [337] with a variety of coating technologies such as sputter deposition [344] [308] and chemical vapor deposition [331]. Here we describe the deposition of ZnO with ALD on polyester/cotton (PES/CO) fabric. Standard microbe and fungi growth tests were performed on the ZnO coated textile. Uncoated PES/CO and PES/CO with Al_2O_3 ALD coating were used as reference materials.

11.5.1 Sample preparation and characterization

ZnO films grown with PE ALD from diethylzinc and oxygen plasma (see Chapter 8). The pressure of DEZ and O_2 in the chamber are controlled with needle valves to 0.02 Pa and 0.5 Pa, respectively. One ALD cycle consists of 2 s DEZ, 10 s pumping, 5 s O_2 plasma and 8 s pumping. Unless mentioned otherwise, 200 cycles were used for the deposition of the coating. The duration of the pulse and pumping times was not optimized. For the deposition of alumina, the same process was used, with trimethylaluminum (TMA) instead of DEZ. As substrates, a woven blend of 65 $\%$ polyester and 35 $\%$ cotton with a fabric weight of 248 g/m^2 were used. This is the material from which for example lab coats and scrub suits are made [227]. The samples received a conventional pre-treatment consisting of being two sided singed, desized, bleached and mercerized.

All textile samples were cut in a circular shape with a radius of 2.1 cm. They were placed into intimate contact with nutrient agar (VWR), which had previously been inoculated with the testing bacterium (Staphylococcus Aureus). After incubation at 37°C during 18-24 hours, a clear area of interrupted growth underneath and along the sides of the test material indicates an antibacterial activity of the specimen. The antifungal properties were checked with AATCC 30 tests. These tests are standardly used to determine the sensitivity of textile against fungi and to evaluate the efficacy of fungicides on fabrics. A small quantity of inoculum, containing spores of Aspergillus Niger, was dispersed homogeneously on the surface of a culture medium. The PES/CO is placed on the surface of the medium

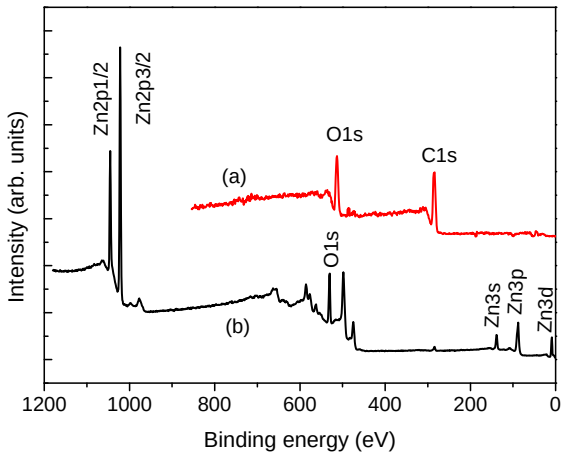

Figure 11.24: XPS survey of (a) uncoated PES/CO textile and (b) fabric coated with 200 cycles ZnO, showing conformal ALD coverage of the substrate. The non-indexed peaks in (b) are Auger lines of Zn and O.

and incubated during at least 72 hours at a temperature of 28°C. To estimate the ALD film thicknesses, pieces of silicon wafer were coated together with the textile substrates. On the silicon, 200 cycles of the DEZ/O_2 ALD process resulted in 16 nm thick ZnO film and in 24 nm Al_2O_3 film for TMA/O_2 ALD (thicknesses were determined by XRR). Figure 11.24(a) shows the XPS spectrum of untreated PES/CO. The textile consists of oxygen and carbon. The beam of X-rays removes electrons from the textile, which are not compensated. As a result, the sample becomes positively charged. This leads to an apparant increase of several hundred electron volts in the binding energy of the peaks in the spectrum. Furthermore, the charging did not stabilize over time, so we could not take detailed scans of peaks associated with a single element. In order to present the XPS result, the measured data were shifted so the maximum of the C1s peak is situated at 285 eV. The fact that O1s and C1s are closer together in 11.24(a) compared to (b) is extra evidence of the charging of this sample during measurement.

The XPS survey of PES/CO coated with 200 ALD cycles ZnO is shown in figure 11.24(b). Here, the charging was much less of an issue (only 20 eV). It is clear that ZnO is deposited on the fibers. The little carbon that can be seen is probably a result from the atmospheric exposure during the transfer from the ALD to the XPS setup.

Since ALD ZnO easily crystallizes (see chapter on ZnO), we measured the

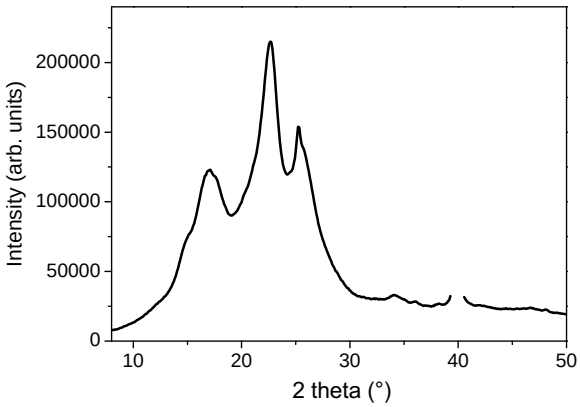

Figure 11.25: XRD spectrum of PES/CO fabric coated with 200 cycles ZnO. The peaks in the signal are caused by the crystalline polyester in the textile blend, there are no peaks due to ZnO crystals.

XRD signal of ZnO on PES/CO (figure 11.25). For reasons of clarity, the molybdenum peak of the XRD substrate holder at 40° was removed from the figure. The peaks in the spectrum are a result of the crystalline polyester in the fabric [277]. No peaks corresponding to crystalline ZnO can be seen, suggesting that zinc oxide is amorphous at these low deposition temperatures.

11.5.2 Antimicrobial test

Figure 11.26 shows the result of the antimicrobial test on PES/CO with 200 cycles of ZnO and the reference samples (uncoated and PES/CO with 200 ALD cycles of alumina). The reference samples have a yellow color because of the bacteria colonies, while the ZnO sample remained clean. The antimicrobial test was also applied to a sample with 200 cycles ZnO that was washed at 40°C for 30 minutes according to the procedure described in ISO 105-C01 (5 g/l ECE detergent, liquor ratio 50:1) and another sample with only 100 ALD cycles of ZnO. Both samples remained white like figure 11.26(b). This demonstrates that the films can be very thin to have effect and that they have good adhesion properties.

Since Staphyllococcus Aureus is an often used model organism for Gram positive bacteria [227] [337], it can be expected that the ALD ZnO will demonstrate antibacterial behavior towards other members of this class. Zinc oxide is known to be a UV-absorbing photocatalyst [337] [191]. However, the incubation was performed in the dark, so that there could not be any photocatalytic breakdown

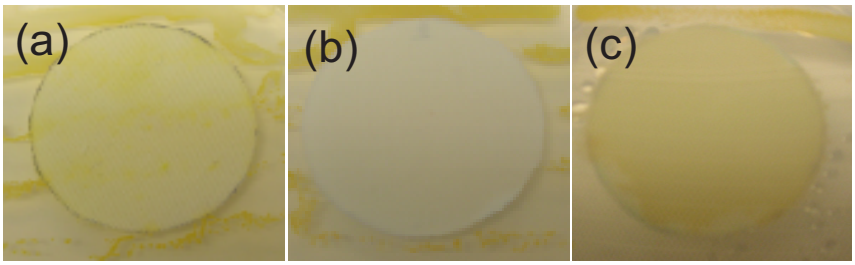

Figure 11.26: Bacteria growth on (a) untreated PES/CO, (b) 200 cycles ALD ZnO and (c) 200 cycles ALD Al_2O_3. The zinc oxide film prevents growth of Staphyllococcus Aureus.

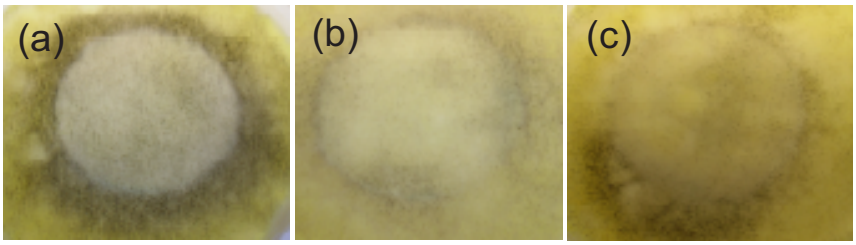

Figure 11.27: Fungus growth on (a) untreated PES/CO, (b) 200 cycles ALD ZnO and (c) 200 cycles ALD Al_2O_3.

of the bacteria. The antibacterial activity of ZnO in the dark is an advantage over TiO_2 coatings on textiles, which are irradiated with UV light for sterilization purposes [331] [277]. This behavior of ZnO might be useful for bandages contacting wounds, especially in view of the resistance of some bacteria against antibiotics [227].

11.5.3 Antifungal test

The samples that underwent the AATCC 30 test are shown in figure 11.27. It is clear that both reference samples and the PES/CO coated with ZnO are overgrown with the Aspergillus Niger fungus. The fact that ZnO is antibacterial but has little or no antifungal effect has also been observed in a study with ZnO nanoparticles [307].

11.6 Conclusions

ALD is promising as a general coating technique for fiber based materials. Especially PE ALD could enable film growth on heat sensitive fibers. Because conformal deposition is one of the key benefits of ALD, the conformality of thermal and

plasma enhanced ALD on non-woven polyester was modeled and studied experimentally in this chapter.

A Monte Carlo based simulation code was developed to study the transport of the precursor in the fiber substrate. The motion of the precursor molecules could be described either as transmission or reflection through a part of the non-woven, or as deposition on the fiber surface. The physical parameters of the substrate taken into account in the model are the total fiber surface area, the surface density of reactive sites and the sticking coefficient. The relevant gas property is the number of particles impinging on the outside of the non-woven.

Experimentally, a piece of non-woven was confined in a Teflon holder. The precursor could only enter through one side, thus enabling us to study the conformality on the substrate in a one-dimensional way. The conformality of the alumina films was determined by measuring the relative Al concentration with EDX.

It was demonstrated that increasing the precursor pulse time per cycle led to a deeper homogeneous coverage of the nonwoven (measured from the opening). The dependence is sub-linear: doubling the exposure time does not result in a doubling of the penetration depth. The reason for this is that molecules can diffuse out of the non-woven before chemisorbing. For a TMA pulse time of 2 s, the simulations show that 90 $\%$ of the precursor escapes the test structure without being deposited on the non-woven. For a TMA pulse time of 30 s, 97 $\%$ of the precursor that enters the test structure leaves without reacting. Varying the sticking coefficient from 1 to 0.01 had little effect on the coverage profile.

For PE ALD, recombination of the oxygen radicals at the non-woven substrate limits the coverage of the non-woven to a few millimeter from the opening. For 8 s of O radical exposure, assuming a sticking coefficient of 0.1 and a recombination coefficient of 0.1, it was calculated that about 40 $\%$ of the radicals recombine to O_2. Only 1 $\%$ reacts with the precursor ligands at the surface of the non-woven. The rest of the O radicals leave the test structure unreacted.

After the study of (PE) ALD conformality on non-wovens, ALD on a number of other fiber based materials was demonstrated. Alumina deposited on tissue paper makes the paper hydrophobic. The same coating on polyamide loops made the loops hydrophilic. The conformal coverage of the loops was illustrated by TEM. ALD was also performed on a woven polyester.

As a final potential application of ALD on textiles, a woven polyester/cotton blend was coated with ZnO. The coating reduced the growth of Staphyllococcus Aureus bacteria on the fabric.

12 Conclusions

The scientific work described in this thesis has atomic layer deposition as its common denominator. Looking back, a number of general conclusions can be drawn.

12.1 Thermal and plasma enhanced ALD processes

First of all, ALD processes were developed or reproduced from literature. The list of processes is summarized in table 12.1. Although no chapter describes ALD of alumina, this process is used so frequently in chapter 11 that it is added for completeness. For details, the reader can consult the conclusions of the separate chapters.

	H_2O	O_2	NH_3	N_2
TMA	Al_2O_3	Al_2O_3	AlN	AlN *
TDMAT	TiO_2	TiO_2	TiN	TiN *
Ti-isopropoxide	TiO_2	TiO_2 *	TiO_xN_y *	-
DEZ	ZnO	ZnO	-	-
V-isopropoxide	V_2O_5	V_2O_5	-	-
$Ru(EtCp)_2$	-	-	Ru *	-

Table 12.1: ALD processes treated in this thesis: combination of precursor and reactive gas results in a film. An asterix indicates that PE ALD is necessary to obtain the film. A dash means the process was not studied or no film growth was observed.

12.2 In-situ study of ALD processes

Once an ALD recipe[1] is established, the question that needs to be answered is 'How does the growth process proceed?'. Therefore, a number of in-situ measurement techniques were combined.

In an attempt to understand the reactions that are taking place during ALD, we have used OES (chapters 7 and 8) and QMS (chapter 8). The growth of metal oxide films from metalorganic precursors and water can be understood as ligand exchange. The organic ligands at the surface of a growing film are hydrogenated by H_2O. The newly formed volatile components are desorbed from the surface. Hydroxyl groups cover the surface, ready to react with the precursor in the next pulse. For example, the thermal process for ZnO is characterized by the half reactions

(a) OH + Zn-$(C_2H_5)_2$ → O-Zn-C_2H_5 + C_2H_6

(b) O-Zn-C_2H_5 + H_2O → O-Zn-OH + C_2H_6

For PE ALD from O_2, the reactive species in the plasma are oxygen radicals. The process has been dubbed a 'combustion like reaction' and was first studied for PE ALD of Al_2O_3 from TMA and oxygen [109]. The organic radicals are oxidized by the radicals, breaking the C-H bonds:

(a) OH + Al-$(CH_3)_3$ → O-Al-$(CH_3)_2$ + CH_4

(b) O-Al-$(CH_3)_2$ + 7 O → O-Al-$(OH)_2$ + CO_2 + CO + 2 H_2O

In the present work, we have verified that this mechanism describes several other PE ALD processes as well. The mechanism was confirmed here for the PE ALD of ZnO (chapter 8):

(a) OH + Zn-$(C_2H_5)_2$ → O-Zn-C_2H_5 + C_2H_6

(b) O-Zn-C_2H_5 + 6 O → O-Zn-OH + CO_2 + CO + 2 H_2O

The organic ligands react with O radicals to form CO, CO_2 and H_2O which can be detected by the mass spectrometer. The transient reaction is also visible as a 'blue flash', where emission lines of the reaction products can be seen or detected with OES.

For nitrides (chapter 9) and metals (chapter 10), we were not able to determine the reaction mechanisms using OES and QMS.

12.3 Benefits and drawbacks of plasma enhanced ALD

Throughout this work, we have compared thermal ALD with PE ALD. The known advantages and disadvantages of PE ALD, already mentioned in chapter 2 are summarized in table 12.2. Specific examples of the pro's and contra's that were observed during the Ph.D. work are summarized below.

[1] A set of experimental parameters that enable the growth of a certain film.

+	-
Low deposition temperature	Limited conformality
Higher reactivity (shorter deposition times)	More complicated reactor designs
Higher film purity	

Table 12.2: Advantages and disadvantages of PE ALD compared to thermal ALD.

12.3.1 Low deposition temperatures

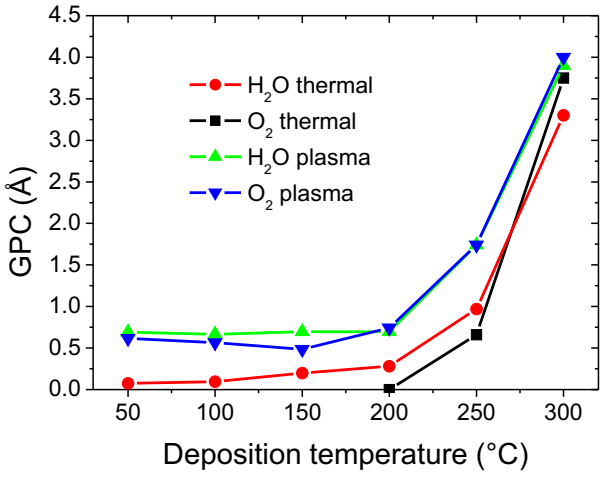

Figure 12.1: GPC as a function of temperature for ALD of vanadia from VTIP

Figure 12.1 shows that no vanadia could be grown by thermal ALD with O_2. This is a result of the double oxygen bond in O_2. When the thermal oxygen step was substituted by an oxygen plasma pulse time, ALD was possible even at 50°C. The energetic electrons in the plasma crack the oxygen molecules into reactive radicals. The possibility to use low deposition temperatures by the plasma step enables ALD on heat-sensitive substrates.

12.3.2 Higher reactivity

An example from the vanadia process illustrates that reaction kinetics can hinder the completion of half-reactions (figure 12.2). In this case, substitution the thermal reagent pulse by a plasma step can reduce the saturation time. The use of a plasma thus significantly increases the throughput of samples.

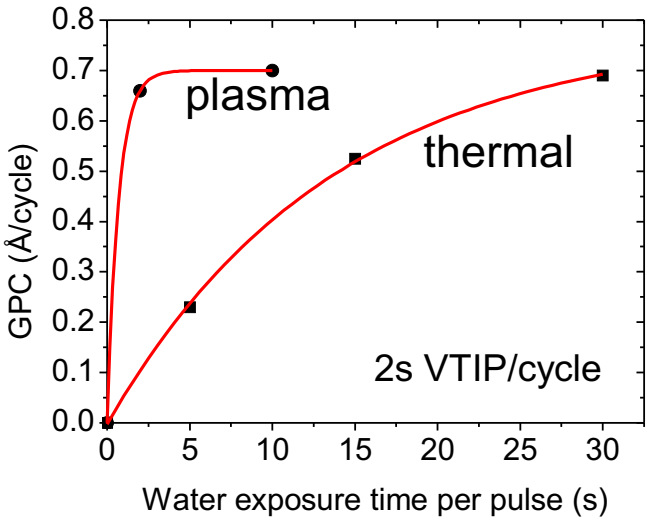

Figure 12.2: GPC of V_2O_5 as a function of water exposure for thermal and PE ALD. Cfr. figure 7.2.

12.3.3 Film stoichiometry and purity

Thermal ALD from TDMAT and NH_3 leads to contamination of oxygen and carbon in the titanium nitride (see Table 9.1 in chapter 9). This was ascribed to reactivity of TDMAT with residual water in vacuum chamber and ligands that had not been completely removed. However, when ammonia plasma was used instead, the amount of impurities was reduced and the stoichiometry of the films was very close to TiN. The purity was also reflected in the observation of low resistivities, expected for pure titanium nitride.

Vanadium pentoxide grown by PE ALD did not contain carbon impurities, while films grown with the thermal process did (chapter 7). The purity of the films were found to be correlated to their crystallinity. The PE ALD grown films were crystalline as-deposited. In addition to the purer films, energy deposited by the plasma onto the growing film may help explain its crystallinity. For titanium dioxide (chapter 6), the film purity (resulting from the thermal or PE ALD process) and its crystallization behavior were also correlated.

12.3.4 Limited conformality

Reactors for PE ALD are more complicated than those suited only for thermal ALD (see chapter 3). Furthermore, the conformality of PE ALD is much reduced

compared to the conformality achieved by thermal ALD [52]. Here, we have studied the conformality on fibrous substrates.

12.4 ALD on fibrous materials

The process development described in chapters 6 to 10 was done on planar samples for ease of characterization. One of the advantages of (thermal) ALD is that it can cover any surface with the right chemical groups and temperature, exposed to the reagents.

To understand of how the coverage of ALD on non-planar substrates (more specifically a non-woven) is linked to the experimental parameters, a combination of experiments and modeling was done. The experimental setup and the coverage profiles for thermal and PE ALD are shown in figure 12.3.

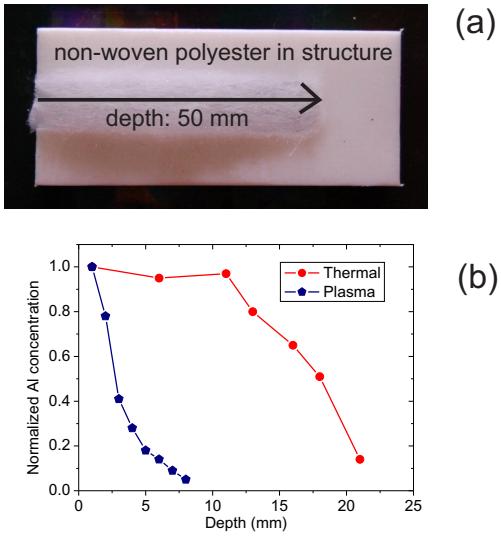

Figure 12.3: Photograph of text structure used for determining ALD penetration into non-woven (a). Relative ALD alumina penetration for thermal and plasma enhanced ALD into a polyester non-woven (b).

An exact model for the motion of the precursor molecules in this structure is almost impossible to built. Such a hypothetical model would not even be interesting because it would lack generality. Therefore, a simplified model was deviced. By using the conservation of mass, it was possible to describe the motion of the aggregated precursor molecules through the substrate as either transmission, reflection or deposition. For PE ALD, recombination of radicals had to be taken into account as well. Figure 12.4 shows the simulated profiles. The recombination

of radicals seriously hampers the ability of PE ALD for coating high aspect ratio substrates. Before the present work, this phenomenon had only been modeled on simple geometries [52].

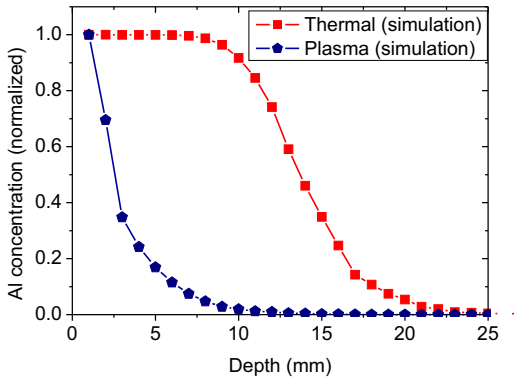

Figure 12.4: Simulated relative ALD alumina penetration for thermal and plasma enhanced ALD into a polyester non-woven, using the same conditions as for the experimental profiles shown in figure 12.3(b).

The ability to coat fibers is more usefull than being a proof-of-principle. Indeed, by the application of an ALD alumina coating, the wettability of fibers could be engineered. When ZnO was deposited on a fabric, the growth of bacteria was reduced.

12.5 Visions for the future of ALD

It was demonstrated in chapter 3 that ALD has already moved from the R&D lab to the manufacturing plant. Technology and scientific understanding of ALD go hand in hand. Improvements in reactors and precursors will broaden the range of applications. Advances in theory and experiments will enhance the technological scope of ALD.

ALD is an enabling technique for everything 'nano'. Because of its Ångstrom-level control over thickness and its conformality, ALD will likely prove to be indespensible for all sorts of future nano-devices. These range from the transistors in processors, to advanced optics (more examples in chapter 3).

Catalysis research is another branch of science determined by the nanoscale. ALD could become very relevant for catalysis, because of the ability to make controlled reactive sites. If cost efficient processes and reactors can be developed, ALD treating tons of industrial catalysts should be possible.

The reaction mechanisms for ALD of metals merit further study. Some experiments and theoretical ideas were already discussed in chapter 2. As was shown in chapter 10, long nucleation delays can occur for metal ALD. A better understanding of the reaction mechanisms may help to reduce this idle time.

Although ALD is over 40 years old, its importance is likely too keep on growing. As the technology matures further, it will become a standard deposition tool. Hopefully, new generations of researchers will be able to use ALD routinely without having to consider all the work done by their predecessors to develop the technology.

A

List of ALD companies

A growing number of companies commercialize ALD reactors or products, mainly for the semiconductor sector. The companies I am aware of are listed below, together with some information on their market, history or products.

- ALD Nanosolutions: IP generation on ALD, spinoff Steven George group (USA)
- Alditri: ALD on filters for biomedical applications, probably not longer active (USA)
- Altatech Semiconductor: ALD/CVD system for semiconductor industry (France)
- Applied Materials: ALD systems integrated with CVD or PVD (USA)
- ARRadiance: ALD system with small footprint (USA)
- ASM: ALD reactor 'Pulsar' for semiconductor manufacturers such as Intel and AMD. ASM acquired the Finnish ALD company Microchemistry in 1999 (Netherlands)
- Atomicity Systems: ALD system (USA)
- ATV-Tech: company specialized in vacuum systems (Germany)
- Aviza: ALD system suited for 300 mm wafers (USA)
- Beneq: ALD for diverse markets (Finland)

- Cambridge Nanotech: ALD systems (USA)
- Jusung Engineering: 'space domain' ALD system (Korea)
- Kurt J. Lesker: ALD system for R&D (USA)
- Levitech: high throughput ALD for solar cells, spinoff of ASM (Netherlands)
- Oxford Instruments: ALD system (USA)
- Picosun: ALD systems, founded by ALD pioneer Suntola (Finland)
- Planar Systems: ALD systems for displays (USA)
- SoLayTec: ALD system for high throughput of solar cells (Netherlands)

References

[1] T. Aaltonen, A. Rahtu, M. Ritala, M. Leskelä, Electrochem. Solid-State Lett. 6, C130 (2003)

[2] T. Aaltonen, P. Alén, M. Ritala, M. Leskelä, Chem. Vap. Dep. 9, 45 (2003)

[3] T. Aaltonen, M. Ritala, K. Arstila, J. Keinonen, M. Leskelä, Chem. Vap. Dep. 10, 215 (2004)

[4] J. Aarik, A. Aidla, H. Mändar, V. Sammelselg, J. Cryst. Growth 220, 531 (2000)

[5] J. Aarik, A. Aidla, T. Uustare, M. Ritala, M. Leskela, Appl. Surf. Sci. 161, 385 (2000)

[6] G. Agostinelli, A. Delabie, P. Vitanov, Z. Alexieva, H. F. W. Dekkers, S. De Wolf, G. Beaucarne, Solar Energy Mater. Solar Cells 90, 3438 (2006)

[7] P. C. Andricacos, ECS Interface (Spring 1999), 32 (1999)

[8] L. M. Apatiga, V. M. Castano, Thin Solid Films 496, 576 (2006)

[9] M. M. Aslan, N. A. Webster, C. L. Byard, M. B. Pereira, C. M. Hayes, R. S. Wiederkehr, S. B. Mendes, Thin Solid Films 518, 4935 (2010)

[10] N. Avci, J. Musschoot, P. F. Smet, K. Korthout, A. Avci, C. Detavernier and D. Poelman, J. Electrochem. Soc. 156, J333 (2009)

[11] L. B. Backman, A. Rautiainen, A. O. I. Krause, M. Lindblad, Catal. Today 43, 11 (1998)

[12] L. B. Backman, A. Rautiainen, M. Lindblad, A. O. I. Krause, Appl. Catal. A 360, 183 (2009)

[13] J. C. Badot, S. Ribes, E. B. Yousfi, V. Vivier, J. P. Pereira-Ramos, N. Baffier, D. Lincot, Electrochem. Solid-State Lett. 3, 485 (2000)

[14] J. C. Badot, A. Mantoux, N. Baffier, O. Dubrunfaut, D. Lincot, J. Mat. Chem. 14, 3411 (2004)

[15] J. C. Badot, A. Mantoux, N. Baffier, O. Dubrunfaut, D. Lincot, J. Phys. Chem. Solids 67, 1270 (2006)

[16] J. R. Bakke, S. F. Bent, ECS Transactions 25, 9 (2009)

[17] E. Ballée, A. Ringuedé, M. Cassir, M. Putkonen, L. Niinistö, Chem. Mater. 21, 4614 (2009)

[18] M. Baltes, A. Kytökivi, B. M. Weckhuysen, R. A. Schoonheydt, P. Van Der Voort, E. F. Vansant, J. Phys. Chem. B. 105, 6211 (2001)

[19] P. Banerjee, I. Perez, L. Henn-Lecordier, S.-B. Lee, G. W. Rubloff, Nature Nanotechnol. 4, 4 (2009)

[20] P. Banerjee, I. Perez, L. Henn-Lecordier, S.-B. Lee, G. W. Rubloff, ECS Transactions 25, 345 (2009)

[21] D. R. Beaulieu, D. Gorelikov, P. de Rouffignac, K. Saadatmand, K. Stenton, N. Sullivan, A. S. Tremsin, Description of ARRadiance, online at http://www.arradiance.com

[22] S. Beke, S. Giorgio, L. Körösi, L. Nanái, W. Marine, Thin Solid Films 516, 4659 (2008)

[23] M. Benmoussa, E. Ibnouelghazi, A. Bennouna, E. L. Ameziane, Thin Solid Films 265, 22 (1995)

[24] J. Biener, T. F. Baumann, Y. Wang, E. J. Nelson, S. O. Kucheyev, A. V. Hamza, M. Kemell, M. Ritala, M. Leskalä, Nanotechnol. 18, 055303 (2007)

[25] M. T. Bohr, R. S. Chau, T. Ghani, K. Mistry, "The high-k solution", IEEE Spectrum (September 2007), available online at http://spectrum.ieee.org/semiconductors/design/the-highk-solution

[26] A. Borras, J. Cotrino, A. R. Gonzalez-Elipe, J. Electrochem. Soc. 154, P152 (2007)

[27] J. K. F. Buijink, J. J. M. van Vlaanderen, M. Crocker, F. G. M. Niele, Catal. Today 93, 199 (2004)

[28] K. S. A. Butcher, P. Afifuddin, P.-T. Chen, M. Godlewski, A. Szczerbakov, E. M. Goldys, T. L. Tansley, J. A. Freitas, J. Cryst. Growth 246, 237 (2002)

[29] G. Buyle, Mater. Technol. 24 (1), 46 (2009)

[30] Cambridge Nanotech website: http://www.cambridgenanotech.com/

[31] D. Cameron, P. Maydannik, T. Kääriäinen, "Towards a roll-to-roll ALD process", available online at http://www.miics.net/2010/material/Towards%20a%20roll-to-roll%20ALD%20process.pdf (2010)

[32] O. Carp, C. L. Huisman, A. Reller, Prog. Solid State Chem. 32, 33 (2004)

[33] A. S. Cavanagh, C. A. Wilson, A. W. Weimer, S. M. George, Nanotechnol. 20, 255602 (2009)

[34] J. Chae, H.-S. Park, S.-W. Kang, Electrochem. Solid-State Lett. 5, C64 (2002)

[35] P. R. Chalker, S. Romani, P. A. Marshall, M. J. Rosseinsky, S. Rushworth, P. A. Williams, Nanotechnol. 21, 405602 (2010)

[36] C. A. Chang, J. Appl. Phys. 67, 566 (1990)

[37] S.-Y. Chang, D.-S. Chen, J. Electrochem. Soc. 157, G154 (2010)

[38] Y.-J. Chang, J. M. Gray, A. Imtiaz, D. Seghete, T. M. Wallis, S. M. George, P. Kabos, C. T. Rogers, V. M. Bright, Sens. Actuat. A 154, 229 (2009)

[39] Z. Chen, Y. B. Jiang, D. R. Dunphy, D. P. Adams, C. Hodges, N. G. Liu, N. Zhang, G. Xomeritakis, X. Z. Jin, N. R. Aluru, S. J. Gaik, H. W. Hillhouse, C. J. Brinker, Nature Mater. 9, 667 (2010)

[40] H.-E. Cheng, C.-M. Hsu, Y.-C. Chen, J. Electrochem. Soc. 156, D275 (2009)

[41] H.-E. Cheng, S. H. Hsiao, D.-M. Lu, Electrochem. Solid-State Lett. 13, D19 (2010)

[42] J. H. Clark, Green Chemistry (Februari 1999), 1 (1999)

[43] M. N. Colpaert, P. Clauws, L. Fiermans, J. Vennik, Surf. Sci. 36, 513 (1973)

[44] R. Cooper, H. P. Upadhyaya, T. K. Minton, M. R. Berman, X. Du, S. M. George, Thin Solid Films 516, 4036 (2008)

[45] R. M. Costescu, D. G. Cahill, F. H. Fabreguette, Z. A. Sechristi, S. M. George, Science 303, 989 (2004)

[46] A. D. Dameron, S. D. Davidson, B. B. Burton, P. F. Garcia, R. S. McLean, S. M. George, J. Phys. Chem. C 112, 4573 (2008)

[47] W. A. Daoud, J. H. Xin, X. Tao, J. Am. Chem. Soc. 87, 1782 (2004)

[48] N. De Geyter, R. Morent, C. Leys, Plasma Sources Sci. Technol. 15, 78 (2006)

[49] A. Delabie, F. Bellenger, M. Houssa, T. Conard, S. Van Elshocht, M. Caymax, M. Heyns, M. Meuris, Appl. Phys. 91, 082904 (2007)

[50] J. Dendooven, unpublished

[51] J. Dendooven, D. Deduytsche, J. Musschoot, R. L. Van Meirhaeghe, C. Detavernier, J. Electrochem. Soc. 156, P63 (2009)

[52] J. Dendooven, D. Deduytsche, J. Musschoot, R. L. Van Meirhaeghe, C. Detavernier, J. Electrochem. Soc. 157, G111 (2010)

[53] C. Detavernier, R. De Gryse, R. L. Van Meirhaeghe, F. Cardon, G. P. Ru, X. P. Qu, B. Z. Li, R. A. Donaton, K. Maex, J. Vac. Sci. Technol. A 18, 470 (2000)

[54] H. Dietrich, P. Geng, K. Jacobi, G. Ertl, J. Chem. Phys. 104, 375 (1996)

[55] Y. Ding, S. Xu, Y. Zhang, A. C. Wang, M. H. Wang, Y. Xiu, C. P. Wong, Z. L. Wang, Nanotechnol. 19, 355708 (2008)

[56] M. E. Donders, H. C. M. Knoops, M. C. M. van de Sanden, W. M. M. Kessels, P. H. L. Notten, ECS Transactions

[57] M. E. Donders, H. C. M. Knoops, M. C. M. van de Sanden, W. M. M. Kessels, P. H. L. Notten, J. Electrochem. Soc. 158, G92 (2011)

[58] J. P. A. M. Driessen, J. Schoonmans, K. F. Jensen, J. Electrochem. Soc. 148, G178 (2001)

[59] T. Driscoll, H.-T. Kim, B.-G. Chae, B.-J. Kim, Y.-W. Lee, N. M. Jokerst, S. Palit, D. R. Smith, M. Di Ventra, D. N. Basov, Science 325, 1518 (2009)

[60] X. Du, S. M. George, Sens. Actuators B 135, 152 (2008)

[61] C. Dücsö, N. Q. Khanh, Z. Horváth, I. Bärsony, M. Utriainen, S. Lehto, M. Nieminen, L. Niinistö, J. Electrochem. Soc. 143, 683 (1996)

[62] J. W. Elam, M. D. Groner, S. M. George, Rev. Sci. Instruments 73, 8 (2002)

[63] J. W. Elam, D. Routkevitch, P. P. Mardilovich, S. M. George, Chem. Mater. 15, 3507 (2003)

[64] J. W. Elam, M. Schuisky, J. D. Ferguson, S. M. George, Thin Solid Films 436, 145 (2003)

[65] K.-E. Elers, T. Blomberg, M. Peussa, B. Aitchison, S. Haukka, S. Marcus, Chem. Vap. Deposition 12, 13 (2006)

[66] S. D. Elliott, G. Scarel, C. Wiemer, M. Fanciulli, G. Pavia, Chem. Mater. 18, 3764 (2006)

[67] S. D. Elliott, Langmuir 26, 9179 (2010)

[68] T.-K. Eom, W. Sari, K.-J. Choi, W.-C. Shin, J. H. Kim, D.-J. Lee, K.-B. Kim, H. Sohn, S.-H. Kim, Electrochem. Solid State Lett. 12, D85 (2009)

[69] K. Eufinger, D. Poelman, H. Poelman, R. De Gryse, G. B. Marin, Appl. Surf. Sci. 254, 148 (2007)

[70] F. H. Fabreguette, S. M. George, Thin Solid Films 515, 7177 (2007)

[71] Z. Fan, D. Wang, P.-C. Chang, W.-Y. Tseng, J. G. Lu, Appl. Phys. Lett. 85, 5923 (2004)

[72] N. Fateh, G. A. Fontalvo, C. Mitterer, Tribol. Lett. 30, 21 (2008)

[73] H. Feng, J. W. Elam, J. A. Libera, M. J. Pellin, P. C. Stair, Chem. Eng. Sci. 64, 560 (2009)

[74] H. Feng, J. W. Elam, J. A. Libera, M. J. Pellin, P. C. Stair, J. Catal. 269, 421 (2010)

[75] J. D. Ferguson, E. R. Smith, A. W. Weimer, S. M. George, J. Electrochem. Soc. 151, G528 (2004)

[76] J. D. Ferguson, K. J. Buechler, A. W. Weimer, S. M. George, Powder Technol. 156, 154 (2005)

[77] J. D. Ferguson, A. W. Weimer, S. M. George, Chem. Mater. 16, 5602 (2005)

[78] J. D. Ferguson, A. W. Weimer, S. M. George, J. Vac. Sci. Technol. A 23, 118 (2005)

[79] F. Fillot, T. Morel, S. Minoret, I. Matko, S. Maitrejean, B. Guillaumot, B. Chenevier, Microelec. Eng. 82, 248 (2005)

[80] D. S. Finch, T. Oreskovic, K. Ramadurai, C. F. Herrmann, S. M. George, R. L. Mahajan, J. Biomed. Mater. Res. 87, 100 (2008)

[81] A. Fridman, L. A. Kennedy, Plasma physics and engineering, New York: Taylor and Francis (2004)

[82] L. Fu, Z. Liu, Y. Liu, B. Han, P. Hu, L. Cao, D. Zhu, Adv. Mater. 17, 217 (2005)

[83] J. R. Fyson, Zs. Nagy, C. L. Bower, e-J. Surf. Sci. Nanotech. 7, 284 (2009)

[84] D. P. Gaillot, O. Deparis, V. Welch, B. K. Wagner, J. P. Vigneron, C. J. Summers, Phys. Rev. E 78, 031922 (2008)

[85] L. Gao, T. J. McCarthy, Langmuir 25, 14105 (2009)

[86] J. Gatineau, K. Yanagita, C. Dussarrat, Microelectron. Eng. 83, 2248 (2008)

[87] S. M. George, Chem. Rev. 110, 111 (2010)

[88] E. Gerritsen, N. Emonet, C. Caillat, N. Jourdan, M. Piazza, D. Fraboulet, B. Boeck, A. Bertholet, S. Smith, P. Mazoyer, Solid-State Electronics 49, 1767 (2005)

[89] A. Gervasini, P. Carniti, J. Keränen, L. Niinistö, A. Auroux, Catal. Today 96, 187 (2004)

[90] A. P. Ghosh, L. J. Gerenser, C. M. Jarman, J. E. Fornalik, Appl. Phys. Lett. 86, 223503 (2005)

[91] M. Y. Ghotbi, J. Alloys Compounds 491, 420 (2010)

[92] E. Gillis, Comptes rendus hebdomadaires des séances de l'Académie des sciences 258, 4765 (1964)

[93] D. N. Goldstein, J. A. McCormick, S. M. George, J. Phys. Chem. C 112, 19530 (2008)

[94] R. G. Gordon, D. Hausmann, E. Kim, J. Shepard, Chem. Vap. Deposit. 9, 73 (2003)

[95] M. D. Groner, F. H. Fabreguette, J. W. Elam, S. M. George, Chem. Mater. 16, 639 (2004)

[96] M. D. Groner, S. M. George, R. S. McLean, F. Garcia, Appl. Phys. Lett. 88, 051907 (2006)

[97] W. Gu, C. P. Tripp, Langmuir 21, 211 (2005)

[98] J. T. Gudmundsson, E. G. Thorsteinsson, Plasma Sources Sci. Technol. 16, 399 (2007)

[99] E. Guziewicz, I. A. Kowalik, M. Godlewski, K. Kopalko, V. Osinniy, A. Wojcik, S. Yatsunenko, E. Lusakowska, W. Paszkowicz, M. Guziewicz, J. Appl. Phys. 103, 033515 (2008)

[100] T. L. Gyeong, K. Do-Heyoung, Thin Solid Films 498, 254 (2006)

[101] J. Haber, M. Witko, R. Tokarz, Appl. Catal. A 157, 3 (1997)

[102] J. Haemers, Comptes rendus hebdomadaires des séances de l'Académie des sciences 259, 3740 (1964)

[103] J. Haemers, E. Baetens, J. Vennik, Phys. Stat. Sol. A - Appl. Res. 20, 381 (1973)

[104] S. Hashimoto, A. Tanaka, Surf. Interface Anal. 34, 262 (2002)

[105] S. Haukka, E.-L. Lakomaa, T. Suntola, Stud. Surf. Sci. Catal. 120, 715 (1998)

[106] M. Heikkilä, E. Puukilainen, M. Ritala, M. Leskelä, J. Photochem. Photobiol. A: Chem. 204, 200 (2009)

[107] S. B. S. Heil, E. Langereis, F. Roozeboom, M. C. M. van de Sanden, W. M. M. Kessels, J. Electrochem. Soc. 153, G956 (2006)

[108] S. B. S. Heil, J. L. van Hemmen, C. J. Hodson, N. Singh, J. H. Klootwijk, F. Roozeboom, M. C. M. van de Sanden, W. M. M. Kessels, J. Vac. Sci. Technol. A 25, 1357 (2007)

[109] S. B. S. Heil, J. L. van Hemmen, M. C. M. van de Sanden, W. M. M. Kessels, J. Appl. Phys. 103, 103302 (2008)

[110] J. E. Herrera, J. H. Kwak, J. Z. Hu, Y. Wang, C. H. F. Peden, Top. Catal. 39 245 (2006)

[111] T. Hirvikorpi, M. Vähä-Nissi, T. Mustonen, E. Iiskola, M. Karppinen, Thin Solid Films 518, 2654 (2010)

[112] T. Hirvikorpi, M. Vähä-Nissi, A. Harlin, M. Karppinen, Thin Solid Films 518, 5463 (2010)

[113] B. Hoex, S. B. S. Heil, E. Langereis, M. C. M. van de Sanden, W. M. M. Kessels, Appl. Phys. Lett. 89, 042112 (2006)

[114] B. Hoex, J. Schmidt, R. Bock, P. P. Altermatt, M. C. M. van de Sanden, W. M. M. Kessels, Appl. Phys. Lett. 91, 112107 (2007)

[115] B. Hoex, J. Schmidt, P. Pohl, M. C. M. van de Sanden, W. M. M. Kessels, J. Appl. Phys. 104, 044903 (2008)

[116] D. M. Hofmann, A. Hofstaetter, F. Leiter, H. Zhou, F. Henecker, B. K. Meyer, S. B. Orlinskii, J. Schmidt, P. G. Baranov, Phys. Rev. Lett. 88, 045504 (2002)

[117] T. P. Holme, C. Lee, F. B. Prinz, Solid State Ionics 179, 1540 (2008)

[118] C.-T. Hsieh, W.-Y. Chen, F.-L. Wu, Carbon 46, 1218 (2008)

[119] M. Hua, H. Y. Tam, H. Y. Ma, C. K. Mok, Wear 260, 1153 (2006)

[120] J. Huang, X. Wang, Z. L. Wang, Nanotechnol. 19, 025602 (2008)

[121] N. Huby, S. Ferrari, E. Guziewicz, M. Godlewski, V. Osinniy, Appl. Phys. Lett. 92, 023502 (2008)

[122] D.-K. Hwang, M.-S. Oh, J.-H. Lim, S.-J. Park, J. Phys. D: Appl. Phys. 40, R387 (2007)

[123] G. K. Hyde, K. J. Park, S. M. Stewart, J. P. Hinestroza, G. N. Parsons, Langmuir 23, 9844 (2007)

[124] G. K. Hyde, S. D. McCullen, S. Jeon, S. M. Stewart, H. Jeon, E. G. Loboa, G. N. Parsons, Biomed. Mater. 4, 025001 (2009)

[125] G. K. Hyde, G. Scarel, J. C. Spagnola, Q. Peng, K. Lee, B. Gong, K. G. Roberts, K. M. Roth, C. A. Hanson, C. K. Devine, S. M. Stewart, D. Hojo, J.-S. Na, J. S. Jur, G. N. Parsons, Langmuir 26, 2550 (2010)

[126] I. K. Igumenov, P. P. Semyannikov, S. V. Trubin, N. B. Morozova, N. V. Gelfond, A. V. Mischenko, J. A. Norman, Surf. Coat. Technol. 201, 9003 (2007)

[127] J. Ihanus, T. Hanninen, T. Hatanpaa, M. Ritala, M. Leskela, J. Electrochem. Soc. 151, H221 (2004)

[128] M. Ishii, S. Iwai, H. Kawata, T. Ueki, Y. Aoyagi, J. Cryst. Growth 180, 15 (1997)

[129] A. H. Janssen, P. Van Der Voort, A. J. Koster, K. P. A. de Jong, Chem. Comm. 15, 1632 (2002)

[130] K. Jefimovs, J. Vila-Comamala, T. Pilvi, J. Raabe, M. Ritala, C. David, Phys. Rev. Lett. 99, 264801 (2007)

[131] C. Jezewski, W. A. Lanford, C. J. Wiegand, J. P. Singh, P.-I. Wang, J. J. Senkevich, T.-M. Lu, J. Electrochem. Soc. 152, C60 (2005)

[132] X. Jiang, H. Huang, F. B. Prinz, S. F. Bent, Chem. Mater. 20, 3897 (2008)

[133] J. Joo, S. M. George, J. Kor. Phys. Soc. 54, 1048 (2009)

[134] Y. S. Jung, A. S. Cavanagh, A. C. Dillon, M. D. Groner, S. M. George, S.-H. Lee, J. Electrochem. Soc. 157, A75 (2010)

[135] T. O. Kääriäinen, D. C. Cameron, M. Tanttari, Plasma Proc. Polym. 6, 631 (2009)

[136] K. Kaiya, N. Yoshii, N. Takahashi, T. Nakamura, J. Mater. Sci. Lett. 19, 2089 (2000)

[137] A. Kasikov, J. Aarik, H. Mändar, M. Moppel, M. Pärs, T. Uustare, J. Phys. D: Appl. Phys. 39, 54 (2006)

[138] E. M. Kelder, J. R. Van Ommen, J. Nijenhuis, US 2009/0155590 A1 (2009)

[139] M. Kemell, V. Pore, M. Ritala, M. Leskelä, M. Lindén, J. Am. Chem. Soc. 127, 14178 (2005)

[140] M. Kemell, V. Pore, M. Ritala, M. Leskelä, Chem. Vap. Deposition, 12, 419 (2006)

[141] M. Kemell, E. Färm, M. Ritala, M. Leskelä, Eur. Polymer J. 44, 3564 (2008)

[142] M. Kemell, M. Ritala, M. Leskelä, R. Groenen, S. Lindfors, Chem. Vap. Dep. 14, 347 (2008)

[143] J. Keränen, A. Auroux, S. Ek, L. Niinistö, Appl. Cat. A: Gen. 228, 213 (2002)

[144] J. Keränen, A. Auroux, S. Ek, L. Niinistö, Appl. Catal. A 228, 213 (2002)

[145] H. Kim, C. Cabral, C. Lavoie, S. M. Rossnagel, J. Vac. Sci. Technol. B 20, 1321 (2002)

[146] H. Kim, S. M. Rossnagel, J. Vac. Sci. Technol. A 20, 802 (2002)

[147] H. Kim, J. Vac. Sci. Technol. B 21, 2231 (2003)

[148] H. Kim, S. M. Rossnagel, Thin Solid Films 441, 311 (2003)

[149] H. Kim, C. Detavernier, O. Van der Straten, S. M. Rossnagel, A. J. Kellock, D. G. Park, J. Appl. Phys. 98, 014308 (2005)

[150] H. Kim, Surf. Coat. Technol. 200, 3104 (2006)

[151] H. Kim, T. Koseki, T. Ohba, T. Ohta, Y. Kojima, H. Sato, S. Hosaka, Y. Shimogaki, Appl. Surf. Sci. 252, 3938 (2006)

[152] H. Kim, H.-B.-R. Lee, W.-J. Maeng, Thin Solid Films 517, 2563 (2009)

[153] J. Y. Kim, S. Seo, D. Y. Kim, H. Jeon, Y. Kim, J. Vac. Sci. Technol. A 22, 8 (2004)

[154] J. Y. Kim, D. Y. Kim, H. O. Park, H. Jeon, J. Electrochem. Soc. 152, G29 (2005)

[155] S. K. Kim, C. S. Hwang, S.-H. K. Park, S. J. Yun, Thin Solid Films 478, 103 (2005)

[156] S. K. Kim, K.-M. Kim, O. S. Kwon, S. W. Lee, C. B. Jeon, W. Y. Park, C. S. Hwang, J. Jeong, Electrochem. Solid-State Lett. 8, F59 (2005)

[157] S. K. Kim, S. Y. Lee, S. W. Lee, G. W. Hwang, C. S. Hwang, J. W. Lee, J. Jeong, J. Electrochem. Soc. 154, D95 (2007)

[158] S. K. Kim, S. Hoffmann-Eifert, M. Reiners, R. Waser, J. Electrochem. Soc. 158, D6 (2011)

[159] T. Kim, I. E. Wachs, J. Catal. 255, 197 (2008)

[160] W. D. Kim, G. W. Hwang, O. S. Kwon, S. K. Kim, M. Cho, D. S. Jeong, S. W. Lee, M. H. Seo, C. S. Hwang, Y.-S. Min, et al. J. Electrochem. Soc. 152, C552 (2005)

[161] W.-H. Kim, S.-J. Park, J.-Y. Son, H. Kim, Nanotechnol. 19, 045302 (2008)

[162] W.-S. Kim, B.-S. Lee, D.-H. Kim, H.-C. Kim, W.-R. Yu, S.-H. Hong, Nanotechnol. 21, 245605 (2010)

[163] Y.-S. Kim, G. A. Ten Eyck, D. Ye, C. Jezewski, T. Karabacak, H.-S. Shin, J. J. Senkevich, T.-M. Lu, J. Electrochem. Soc. 152, C376 (2005)

[164] D. M. King, J. A. Spencer, X. Liang, L. F. Hakim, A. W. Weimer, Surf. Coat. Technol. 201, 9163 (2007)

[165] D. M. King, X. H. Liang, A. W. Weimer, ECS Transactions 25, 163 (2009)

[166] J. S. King, D. Heineman, E. Graugnard, C. J. Summers, Appl. Surf. Sci. 244, 511 (2005)

[167] J. A. Kittl, K. Opsomer, M. Popovici, N. Menou, B. Kaczer, X. P. Wang, C. Adelmann, M. A. Pawlak, K. Tomida, A. Rothschild, B. Govoreanu, R. Degraeve, M. Schaekers, M. Zahid, A. Delabie, J. Meersschaut, W. Polspoel, S. Clima, G. Pourtois, W. Knaepen, C. Detavernier, V. V. Afanas'ev, T. Blomberg, D. Pierreux, J. Swerts, P. Fischer, J. W. Maes, D. Manger, W. Vandervorst, T. Conard, A. Franquet, P. Favia, H. Bender, B. Brijs, S. Van Elshocht, M. Jurczak, J. Van Houdt, D. J. Wouters, Microelectron. Eng. 86, 1789 (2009)

[168] W. Knaepen, C. Detavernier, R. L. Van Meirhaeghe, J. Jordan Sweet, C. Lavoie, Thin Solid Films 516, 4946 (2008)

[169] W. Knaepen, Ph. D. Thesis "Characterization of solid state reactions and crystallization in thin films using in situ X-ray diffraction", Ghent University (2010)

[170] M. Knez, A. M. Bittner, F. Boes, C. Wege, H. Jeske, E. Maiss, K. Kern, Nano Lett. 3, 1079 (2003)

[171] M. Knez, A. Kadri, C. Wege, U. Gösele, H. Jeske, K. Nielsch, Nano Lett. 6, 1172 (2006)

[172] M. Knez, K. Nielsch, L. Niinistö, Adv. Mater. 19, 3425 (2007)

[173] H. C. M. Knoops, M. E. Donders, L. Baggato, M. C. M. van de Sanden, P. H. L. Notten, W. M. M. Kessels, ECS Transactions 25, 333 (2009)

[174] H. C. M. Knoops, E. Langereis, M. C. M. van de Sanden, W. M. M. Kessels, J. Electrochem. Soc. 157, G241 (2010)

[175] M. Kolle, P. M. Salgard-Cunha, M. R. J. Scherer, F. Huang, P. Vukusic, S. Mahajan, J. J. Baumberg, U. Steiner, Nature Nanotechnol. DOI:10.1038/NNANO.2010.101 (2010)

[176] B. H. Kong, M. K. Choi, H. K. Cho, J. H. Kim, S. Baek, J.-H. Lee, Electrochem. Solid-State Lett. 13, K12 (2010)

[177] G. Kotliar, D. Vollhardt, Phys. Today March 2004, 53 (2004)

[178] I. A. Kowalik, E. Guziewicz, K. Kopalko, S. Yatsunenko, M. Godlewski, A. Wojcik, V. Osinniy, T. Krajewski, T. Story, E. Lusakowska, W. Paszkowicz, Acta Physica Polonica A 112, 401 (2007)

[179] K. Kukli, J. Aarik, A. Aidla, T. Uustare, I. Jogi, J. Lu, M. Tallarida, M. Kemell, A.-A. Kiisler, M. Ritala, M. Leskela, J. Cryst. Growth 312, 12 (2010)

[180] J. H. Kwak, J. E. Herrera, J. Z. Hu, Y. Wang, C. H. F. Peden, Appl. Catal. A 300, 109 (2006)

[181] O.-K. Kwon, S.-H. Kwon, H.-S. Park, S.-W. Kang, Electrochem. Solid-State Lett. 7, C46 (2004)

[182] O.-K. Kwon, J.-H. Kim, H.-S. Park, S.-W. Kang, J. Electrochem. Soc. 151, G109 (2004)

[183] S.-H. Kwon, O.-K Kwon, J.-H. Kim, H.-R. Oh, K.-H. Kim, S.-W. Kang, J. Electrochem. Soc. 155, H296 (2008)

[184] E. Langereis, M. Creatore, S. B. S. Heil, M. C. M. van de Sanden, W. M. M. Kessels, Appl. Phys. Lett. 89, 081915 (2006)

[185] E. Langereis, S. B. S. Heil, H. C. M. Knoops, W. Keuning, M. C. M. van de Sanden, W. M. M. Kessels, J. Phys. D: Appl. Phys. 42, 073001 (2009)

[186] C.-S. Lee, J. Kim, J. Y. Son, W. Choi, H. Kim, Appl. Catal. B 91, 628 (2009)

[187] H.-B.-R. Lee, H. Kim, Electrochem. Solid-State Lett. 9, G323 (2006)

[188] H.-B.-R. Lee, J. Y. Son, H. Kim, Appl. Phys. Lett. 90, 213509 (2007)

[189] H.-Y. Lee, Y.-W. Hsieh, C.-H. Hsu, K. S. Liang, Mat. Chem. Phys. 82, 984 (2003)

[190] S.-H. Lee, H. M. Cheong, M. J. Seong, P. Liu, C. E. Tracy, A. Mascarenhas, J. R. Pitts, S. K. Deb, Solid State Ionics 165, 111 (2003)

[191] S.-M. Lee, G. Grass, G.-M. Kim, C. Dresbach, L. Zhang, U. Gösele, M. Knez, Phys. Chem. Chem. Phys. 11, 3608 (2009)

[192] S.-M. Lee, E. Pippel, U. Gösele, C. Dresbach, Y. Qin, C. V. Chandran, T. Bräuniger, G. Hause, M. Knez, Nature 324, 488 (2009)

[193] S.-M. Lee, E. Pippel, O. Moutanabbir, I. Gunkel, T. Thurn-Albrecht, M. Knez, Appl. Mater. Interfaces 2, 2436 (2010)

[194] M. Leskelä, M. Ritala, Thin Solid Films 409, 138 (2002)

[195] M. Leskelä, M. Kemell, K. Kukli, V. Pore, E. Santala, M. Ritala, J. Lu, Mat. Sci. Eng. C 27, 1504 (2007)

[196] M. Leskelä, V. Pore, T. Hatanpää, M. Heikkilä, M. Ritala, A. Schrott, S. Raoux, S. M. Rossnagel, ECS Transactions 25, 399 (2009)

[197] D. H. Levy, D. Freeman, S. F. Nelson, P. J. Cowdery-Corvan, L. M. Irving, Appl. Phys. Lett. 92, 192101 (2008)

[198] J. Li, X. Liang, D. M. King, Y.-B. Jiang, A. W. Weimer, Appl. Catal. B 97, 220 (2010)

[199] J. F. Li, Y. F. Huang, Y. Ding, Z. L. Yang, S. B. Li, X. S. Zhou, F. R. Fan, W. Zhang, Z. Y. Zhou, D. Y. Wu, B. Ren, Z. L. Wang, Z. Q. Tian, Nature 464, 392 (2010)

[200] X. Liang, D. M. King, P. Li, A. W. Weimer, J. Am. Ceram. Soc. 92, 649 (2009)

[201] X. H. Liang, A. D. Lynn, D. M. King, S. J. Bryant, A. W. Weimer, ACS Appl. Materials and Interfaces 1, 1988 (2009)

[202] J. A. Libera, J. W. Elam, M. J. Pellin, Thin Solid Films 516, 6158 (2008)

[203] J.-W. Lim, J.-S. Park, S.-W. Kang, J. Appl. Phys. 87, 4632 (2000)

[204] S. J. Lim, S. Kwon, H. Kim, Thin Solid Films 516, 1523 (2008)

[205] S. P. Lim, J. D. Long, S. Xu, K. Ostrikov, J. Phys. D: Appl. Phys. 40, 1085 (2007)

[206] W. T. Lim, C. H. Lee, Thin Solid Films 353, 12 (1999)

[207] G. X. Liu, F. K. Shan, W. J. Lee, G. H. Lee, I. S. Kim, B. C. Shin, S. G. Yoon, C. R. Cho, Integrated Ferroelectrics 81, 239 (2006)

[208] J. Lu, K. M. Kosuda, R. P. Van Duyne, P. C. Stair, J. Phys. Chem. C 113, 12412 (2009)

[209] T. Machold, W. Y. Suprun, H. Papp, J. Mol. Cat. A: Chem. 280, 122 (2008)

[210] A. J. M. Mackus, S. B. S. Heil, E. Langereis, H. C. M. Knoops, M. C. M. van de Sanden, W. M. M. Kessels, J. Vac. Sci. Technol. A 28, 77 (2010)

[211] A. Mantoux, H. Groult, E. Balnois, P. Doppelt, L. Gueroudji, J. Electrochem. Soc. 150, A368 (2004)

[212] E. Marin, L. Guzman, A. Lanzutti, L. Fedrizzi, M. Saikkonen, Electrochem. Comm. 11, 2060 (2009)

[213] A. Martin Hoyas, J. Schuhmacher, D. Shamiryan, J. Waeterloos, W. Besling, J. P. Celis, K. Maex, J. Appl. Phys. 95, 381

[214] T. Massalski (editor), Assessed V-O Phase Diagram, Binary alloy phase diagrams [CDROM], ASM International (1996).

[215] R. Matero, A. Rahtu, M. Ritala, M. Leskelä, T. Sajavaara, Thin Solid Films 368, 1 (2000)

[216] J. A. McCormick, B. L. Cloutier, A. W. Weimer, S. M. George, J. Vac. Sci. Technol. A 25, 67 (2007)

[217] J. Meyer, D. Schneidenbach, T. Winkler, S. Hamwi, T. Weimann, P. Hinze, S. Ammermann, H.-H. Johannes, T. Riedl, W. Kowalsky, Appl. Phys. Lett. 94, 23305 (2009)

[218] V. Miikkulainen, M. Suvanto, T. A. Pakkanen, S. Siitonen, P. Karvinen, M. Kuittinen, H. Kisonen, Surf. Coat. Technol. 202, 5103 (2008)

[219] J.-S. Min, H.-S. Park, S.-W. Kang, Appl. Phys. Lett. 75, 1521 (1999)

[220] D. R. G. Mitchell, G. Triani, D. J. Attard, K. S. Finnie, P. J. Evans, C. J. Barbé, J. R. Bartlett, Smart Mater. Struct. 15, S57 (2006)

[221] B. Mitra, I. E. Wachs, G. Deo, J. Catal. 240, 151 (2006)

[222] F. J. Morin, Phys. Rev. Lett. 3, 34 (1959)

[223] N. F. Mott, Rev. Mod. Phys. 40, 677 (1968)

[224] M. N. Mullings, H.-B.-R. Lee, N. Marchack, X. Jiang, Z. Chen, Y. Gorlin, K.-P. Lin, S. F. Bent, J. Electrochem. Soc. 157, D600 (2010)

[225] B. H. Munk, H. B. Schlegel, Chem. Mater. 18, 1878 (2006)

[226] I. Muylaert, J. Musschoot, C. Detavernier, P. Van Der Voort, in preparation

[227] A. N. Neely, M. P. Maley, J. Clin. Microbiol. 38, 724 (2000)

[228] C. J. W. Ng, H. Gao, T. T. Y. Tan, Nanotechnol. 19, 445604 (2008)

[229] L. Niinistö, Curr. Opinion Solid State Mater. Sci. 3, 147 (1998)

[230] O. Nilsen, O. B. Karlsen, A. Kjekshus, H. Fjellvåg, Thin Solid Films 515, 4527 (2007)

[231] O. Nilsen, O. B. Karlsen, A. Kjekshus, H. Fjellvåg, Thin Solid Films 515, 4538 (2007)

[232] O. Nilsen, O. B. Karlsen, A. Kjekshus, H. Fjellvåg, Thin Solid Films 515, 4550 (2007)

[233] O. Nilsen, E. Rauwel, H. Fjellvåg, A. Kjekshus, J. Mater. Chem. 17, 1466 (2007)

[234] Y. Ningyi, L. Jinhua, L. Chenglu, Appl. Surf. Sci. 191, 176 (2002)

[235] A. Niskanen, K. Arstila, M. Ritala, M. Leskelä, J. Electrochem. Soc. 152, F90 (2005)

[236] A. Niskanen, K. Arstila, M. Leskelä, M. Ritala, Chem. Vap. Dep. 13, 152 (2007)

[237] C. Nistorica, J.-F. Liu, I. Gory, G. D. Skidmore, F. M. Mantiziba, B. E. Gnade, J. Kim, J. Vac. Sci. Technol. A 23, 836 (2005)

[238] L. Norin, E. Vanin, P. Soininen, M. Putkonen, 2007 Conference on lasers and electro-optics/quantum electronics and laser science conference, 769 (2007)

[239] P. H. L. Notten, F. Roozeboom, R. A. H. Niessen, L. Baggetto, Adv. Mater. 19, 4564 (2007)

[240] K. S. Novoselov, A. K. Geim, S. V. Morozov, D. Jiang, Y. Zhang, S. V. Dubonos, I. V. Grigorieva, A. A. Firsov, Science 306, 666 (2004)

[241] K. S. Novoselov, A. K. Geim, S. V. Morozov, D. Jiang, M. I. Katsnelson, I. V. Grigorieva, S. V. Dubonos, A. A. Firsov, Nature 438, 197 (2005)

[242] L. Nyns, L.-A. Ragnarsson, L. Hall, A. Delabie, M. Heyns, S. Van Elshocht, C. Vinckier, P. Zimmerman, S. De Gendt, J. Electrochem. Soc. 155, G9 (2008)

[243] P. Osiceanu, Appl. Surf. Sci. 253, 381 (2006)

[244] H. Over, Y. D. Kim, A. P. Seitsonen, S. Wendt, E. Lundgren, M. Schmid, P. Varga, A. Morgante, G. Ertl, Science 1474 (2000)

[245] J. Paivasaari, M. Putkonen, L. Niinisto, Thin Solid Films 472, 275 (2005)

[246] A. Paranjpe, S. Gopinath, T. Omstead, R. Bubber, J. Electrochem. Soc. 148, G465 (2001)

[247] C. W. Park, H. Y. Yu, U. H. Pi, S. Y. Choi, Nanotechnol. 16, 361 (2006)

[248] K.-C. Park, K.-B. Kim, I. J. M. M. Raaijmakers, K. Ngan, J. Appl. Phys. 80, 5674 (1996)

[249] S.-H. K. Park, J. Oh, C.-S. Hwang, J.-I. Lee, Y. S. Yang, H. Y. Chu, Electrochem. Solid State Lett. 8, H21 (2005)

[250] S.-H. K. Park, C.-S. Hwang, H.-S. Kwack, J.-H. Lee, H. Y. Chu, Electrochem. Solid-State Lett. 9, G299 (2006)

[251] S.-J. Park, W.-H. Kim, H.-B.-R. Lee, W. J. Maeng, H. Kim, Microelectron. Eng. 85, 39 (2008)

[252] M. J. Pellin, J. N. Hryn, J. W. Elam, US2004/0178175 A1 (2004)

[253] M. J. Pellin, P. C. Stair, G. Xiong, J. W. Elam, J. Birrell, L. Curtiss, S. M. George, C. Y. Han, L. Iton, H. Kung, M. Kung, H.-H. Wang, Catal. Lett. 102, 127 (2005)

[254] Q. Peng, X. Y. Sun, J. C. Spagnola, G. K. Hyde, R. J. Spontak, G. N. Parsons, Nano Lett. 7, 719 (2007)

[255] C. S. Petersson, J. E. E. Baglin, J. J. Dempsey, F. M. d'Heurle, S. J. La Placa, J. Appl. Phys. 53, 4866 (1982)

[256] R. Pheamhom, C. Sunwoo, D.-H. Kim, J. Vac. Sci. Technol. A 24, 1535 (2006)

[257] H. Poelman, J. Vennik, G. Dalmai, J. Electron Spectroscop. Related Phenomena 44, 251 (1987)

[258] H. Poelman, B. F. Sels, M. Olea, K. Eufinger, J. S. Paul, B. Moens, I. Sack, V. Balcaen, F. Bertinchamps, E. M. Gaigneaux, P. A. Jacobs, G. B. Marin, D. Poelman, R. De Gryse, J. Catal. 245, 156 (2006)

[259] P. Poodt, A. Lankhorst, F. Roozeboom, K. Spee, D. Maas, A. Vermeer, Adv. Mater. 22, 3564 (2010)

[260] W. J. Potscavage, S. Yoo, B. Domercq, B. Kippelen, Appl. Phys. Lett. 90, 253511 (2007)

[261] S. E. Potts, W. Keuning, E. Langereis, G. Dingemans, M. C. M. van de Sanden, W. M. M. Kessels, J. Electrochem. Soc. 157, P66 (2010)

[262] I. M. Povey, M. Bardosova, F. Chalvet, M. E. Pemble, H. M. Yates, Surf. Coat. Technol. 201, 9345 (2007)

[263] H. B. Profijt, P. Kudlacek, M. C. M. van de Sanden, W. M. M. Kessels, J. Electrochem. Soc. 158, G88 (2011)

[264] S.-W. Pung, K.-L. Choy, X. Hou, C. Shan, Nanotechnol. 19, 435609 (2008)

[265] M. Putkonen, J. Harjuoja, T. Sajavaara, L. Niinistö, J. Mater. Chem. 17, 664 (2007)

[266] M. Putkonen, T. Luiskala, J. Lappalainen, ALD 2008 Book of Abstracts TueA2-3, 8th international conference on atomic layer deposition, Bruges, Belgium (2008).

[267] M. Putkonen, M. Rajala, T. Mäntylä, "Increasing the glass cracking resistance by atomic layer deposition", Poster 63 at ALD 2008, Bruges, Belgium (2008)

[268] M. Putkonen, ECS Transactions 25 (4), 143 (2009)

[269] M. Putkonen, T. Aaltonen, M. Alnes, T. Sajavaara, O. Nilsen, H. Fjellvåg, J. Mater. Chem. 19, 8767 (2009)

[270] M. Putkonen, T. Sajavaara, P. Rahkila, L. Xu, S. Cheng, L. Niinistö, H. J. Whitlow, Thin Solid Films 517, 5819 (2009)

[271] R. Puurunen, Ph. D. Thesis, Helsinki University of Technology (2002)

[272] R. L. Puurunen, A. Root, P. Sarv, M. M. Viitanen, H. H. Brongersma, M. Lindblad, A. O. I. Krause, Chem. Mater. 14, 720 (2002)

[273] R. L. Puurunen, S. M. K. Airaksinen, A. O. I. Krause, J. Catal. 213, 281 (2003)

[274] R. L. Puurunen, W. Vandervorst, J. Appl. Phys. 96, 7686 (2004)

[275] R. L. Puurunen, J. Appl. Phys. 97, 121301 (2005)

[276] M. M. Qazilbash, K. S. Burch, D. Whisler, D. Shrekenhamer, B. G. Chae, H. T. Kim, D. N. Basov, Phys. Rev. B 74, 205118 (2006)

[277] K. Qi, J. H. Xin, W. A. Daoud, C. L. Mak, Int. J. Appl. Ceram. Technol. 4, 554 (2007)

[278] H. Qiao, X. Zhu, Z. Zheng, L. Liu, L. Zhang, Electrochem. Comm. 8, 21 (2006)

[279] A. Rahtu, T. Alaranta, M. Ritala, Langmuir 17, 6506 (2001)

[280] A. Rahtu, M. Ritala, M. Leskelä, Chem. Mater. 13, 1528 (2001)

[281] A. Rahtu, M. Ritala, Chem. Vap. Dep. 8, 21 (2002)

[282] V. R. Rai, S. Agarwal, J. Phys. Chem. C 112, 9552 (2008)

[283] V. R. Rai, S. Agarwal, J. Phys. Chem. C 113, 12962 (2009)

[284] V. R. Rai, V. Vandalon, S. Agarwal, Langmuir 26, 13732 (2010)

[285] G. Rampelberg, M. Schaekers, K. Martens, Q. Xie, D. Deduytsche, B. De Schutter, N. Blasco, J. Kittl, C. Detavernier, Appl. Phys. Lett. 98, 162902 (2011)

[286] R. H. A. Ras, M. Kemell, J. de Wit, M. Ritala, G. ten Brinke, M. Leskelä, O. Ikkala, Adv. Mater. 19, 102 (2007)

[287] M. Raulio, V. Pore, S. Areva, M. Ritala, M. Leskelä, M. Lindén, J. B. Rosenholm, K. Lounatmaa, M. Salkinoja-Salonen, J. Ind. Microbiol. Biotechnol. 33, 261 (2006)

[288] J. Ren, F.-Y. Liu, Y.-T. Zhang, D. W. Zhang, Thin Solid Films 515, 4702 (2007)

[289] J. Ren, Appl. Surf. Sci. 255, 5742 (2009)

[290] D. Riihelä, M. Ritala, R. Matero, M. Leskelä, Thin Solid Films 289, 250 (1996)

[291] M. Riordan, "The silicon dioxide solution", IEEE Spectrum (December 2007). Available online at http://spectrum.ieee.org/semiconductors/design/the-silicon-dioxide-solution

[292] D. Rische, H. Parala, A. Baunemann, T. Thiede, R. Fischer, Surf. Coat. Technol. 201, 9125 (2007)

[293] M. Ritala, M. Leskelä, L. Niinistö, P. Haussalo, Chem. Mater. 5, 1174 (1993)

[294] M. Ritala, M. Kemell, M. Lautala, A. Niskanen, M. Leskelä, S. Lindfors, Chem. Vap. Deposition 12, 655 (2006)

[295] M. Ritala, V. Pore, T. Hatanpää, M. Heikkilä, M. Leskelä, K. Mizohata, A. Schrott, S. Raoux, S. M. Rossnagel, Microelectron. Eng. 86, 1946 (2009)

[296] J. Robertson, Rep. Prog. Phys. 69, 327 (2006)

[297] M. Rose, J. W. Bartha, I. Endler, Appl. Surf. Sci. 256, 3778 (2010)

[298] A. Rosental, A. Tarre, A. Gerst, J. Sundqvist, A. Harsta, A. Aidla, J. Aarik, V. Sammelselg, T. Uustare, Sens. Actuators B 93, 552 (2003)

[299] S. M. Rossnagel, A. Sherman, F. Turner, J. Vac. Sci. Technol. B 18, 2016 (2000)

[300] S. M. Rossnagel, T. S. Kuan, J. Vac. Sci. Technol. B 22, 240 (2004)

[301] S. M. Rossnagel, "From PVD to CVD to ALD in semiconductor manufacturing applications", talk at ICTF 14, Ghent, Belgium (November 19, 2008)

[302] K. M. Roth, K. G. Roberts, G. K. Hyde, Textile Res. J. (2010), doi:10.1177/0040517510371868

[303] A. K. Roy, W. Baumann, I. Knig, G. Baumann, S. Schulze, M. Hietschold, T. Mäder, D. J. Nestler, B. Wielage, W. A. Goedel, Anal. Bioanal. Chem. 396, 1913 (2010)

[304] G. W. Rubloff, P. Banerjee, I. Perez, L. Henn-Lecordier, E. Cleveland, S. B. Lee, "Electrostatic Nanocapacitors for High Performance Energy Storage", Presentation at ALD 2009, Monterey, CA, USA

[305] B. W. Sanders, A. Kitai, Chem. Mater. 4, 1005 (1992)

[306] M. Sangermano, E. Borlatto, F. D. D'Hérin Bytner, A. Priola, G. Rizza, Prog. Organ. Coat. 59, 122 (2007)

[307] J. Sawai, T. Yoshikawa, J. Appl. Microbiol. 96, 803 (2004)

[308] J. Scholz, G. Nocke, F. Hollstein, A. Weissbach, Surf. Coat. Technol. 192, 252 (2005)

[309] M. Schuisky, A. Harsta, A. Aidla, K. Kukli, A.-A. Kiisler, J. Aarik, J. Electrochem. Soc. 147, 3319 (2000)

[310] M. Schuisky, J. W. Elam, S. M. George, Appl. Phys. Lett. 81, 180 (2002)

[311] J. Schmidt, F. Werner, B. Veith, D. Zielke, R. Bock, V. Tiba, P. Poodt, F. Roozeboom, A. Li, A. Cuevas, R. Brendel, "Industrially relevant Al_2O_3 deposition techniques for the surface passivation of Si solar cells", 25th European Photovoltaic Solar Energy Conference, Valencia, Spain (September 6-10, 2009)

[312] D. Schuring, Ph. D. Thesis, Eindhoven University of Technology (2002)

[313] Z. A. Sechrist, B. T. Schwartz, J. H. Lee, J. A. McCormick, R. Piestun, W. Park, S. M. George, Chem. Mater. 18, 3562 (2006)

[314] A. K. Sen, Coated Textiles - Principles and Applications, Technomic Publishing Company, Inc. (2001) ISBN 1-58716-023-4

[315] C. X. Shan, X. Hou, K.-L. Choy, P. Choquet, Surf. Coat. Technol. 202, 2147 (2008)

[316] C. X. Shan, X. Hou, K.-L. Choy, Surf. Coat. Technol. 202, 2399 (2008)

[317] J. H. Shim, C.-C. Chao, H. Huang, F. B. Prinz, Chem. Mater. 19, 3850 (2007)

[318] J. H. Shim, X. Jiang, S. Bent, F. B. Prinz, ECS Transactions 25, 323 (2009)

[319] J. H. Shim, J. S. Park, J. An, T. M. Gür, S. Kang, F. B. Prinz, Chem. Mater. 21, 3290 (2009)

[320] M. Shirolkar, M. K. Abyaneh, A. Singh, A. Tomer, R. Choudhary, V. Sathe, D. Phase, S. Kulkarni, J. Phys. D: Appl. Phys. 41, 155308 (2008)

[321] R. J. Silvennoinen, O. J. T. Jylhä, M. Lindblad, H. Österholm, A. O. I. Krause, Catal. Lett. 114, 135 (2007)

[322] G. Silversmit, D. Depla, H. Poelman, G. B. Marin, R. De Gryse, J. Electron Spectrosc. Relat. Phenom. 135, 167 (2004)

[323] R. E. J. Sladek, E. Stoffels, R. Walraven, P. J. A. Tielbeek, R. A. Koolhoven, IEEE Trans. Plasma Sci. 32, 1540 (2004)

[324] M. Q. Snyder, B. A. McCool, J. DiCarlo, C. P. Tripp, W. J. DeSisto, Thin Solid Films 514, 97 (2006)

[325] Solaytec website: http://www.solaytec.com

[326] K. Solehmainen, T. Aalto, J. Dekker, M. Kapulainen, M. Harjanne, K. Kukli, P. Heimala, K. Kolari, M. Leskelä, J. Lightwave Technol. 23, 3875

[327] J. C. Spagnola, B. Gong, S. A. Arvidson, J. S. Sur, S. A. Khan, G. N. Parsons, J. Mater. Chem. 20, 4213 (2010)

[328] S. P. Sree, J. Dendooven, T. I. Koranyi, G. Vanbutsele, K. Houthoofd, D. Deduytsche, J. A. Martens, C. Detavernier, submitted (2010)

[329] P. C. Stair, C. Marshall, G. Xiong, H. Feng, M. J. Pellin, J. W. Elam, L. Curtiss, L. Iton, H. Kung, M. Kung, H.-H. Wang, Top. Catal. 39, 181 (2006)

[330] F. Svegl, B. Orel, M. G. Hutchins, K. Kalcher, J. Electrochem. Soc. 143, 1532 (1996)

[331] H. Szymanowski, A. Sobczyk, M. Gazicki-Lipman, W. Jakubowski, L. Klimek, Surf. Coat. Technol. 200, 1036 (2005)

[332] C. Thambidurai, Y.-G. Kim, J. L. Stickney, Electrochim. Acta 53, 6157 (2008)

[333] C. V. Thompson, J. Appl. Phys. 58, 763 (1985)

[334] T. Törndahl, C. Platzer-Björkman, J. Kessler, M. Edoff, Prof. Photovolt.: Res. Appl. 15, 225 (2007)

[335] P. Van Der Voort, R. van Welzenis, M. de Ridder, H. H. Brongersma, M. Baltes, M. Mathieu, P. C. van de Ven, E. F. Vansant, Langmuir 18, 4420 (2002)

[336] A. Vansteenkiste, K. W. Chou, M. Weigand, M. Curcic, V. Sackmann, H. Stoll, T. Tyliszczak, G. Woltersdorf, C. H. Back, G. Schütz, B. Van Waeyenberge, Nature Phys. 5, 332 (2009)

[337] N. Vigneshwaran, S. Kumar, A. A. Kathe, P. V. Varadarajan, V. Prasad, Nanotechnology 17, 5087 (2006)

[338] S. Vilhunen, M. Bosund, M.-L. Kääriäinen, D. Cameron, M. Sillanpää, Sep. Purif. Technol. 66, 130 (2009)

[339] J. J. Wang, A. Nikolov, Q. Wu, IEEE Photon. Technol. Lett. 18, 2650 (2006)

[340] X. Wang, S. M. Tabakman, H. Dai, J. Am. Chem. Soc. 130, 8152 (2008)

[341] J. R. Wank, S. M. George, A. W. Weimer, Powder Technol. 142, 59 (2004)

[342] T. Watanabe, S. Hoffman-Eifert, L. Yang, A. Rüdiger, C. Kügeler, C. S. Hwang, R. Waser, J. Electrochem. Soc. 154, G134 (2007)

[343] B. M. Weckhuysen, D. E. Keller, Catal. Today 78, 25 (2003)

[344] Q. Wei, Q. Li, D. Hou, Z. Yang, W. Gao, Surf. Coat. Technol. 201, 1821 (2006)

[345] Q. Wei, L. Yu, N. Wu, S. Hong, J. Ind. Text. 37, 275 (2008)

[346] M. A. Weimer, L. F. Hakim, D. M. King, X. Liang, A. W. Weimer, S. M. George, P. Li, M. D. Groner, Appl. Phys. Lett. 92, 164101 (2008)

[347] C. A. Wilson, D. N. Goldstein, J. A. McCormick, A. W. Weimer, S. M. George, J. Vac. Sci. Technol. A 26, 430 (2004)

[348] C. A. Wilson, R. K. Grubbs, S. M. George, Chem. Mater. 17, 5625 (2005)

[349] C. A. Wilson, J. A. McCormick, A. S. Cavanagh, D. N. Goldstein, A. W. Weimer, S. M. George, Thin Solid Films 516, 6175 (2008)

[350] J. Wöllenstein, M. Burgmair, G. Plescher, T. Sulima, J. Hildenbrand, H. Böttner, I. Eisele, Sens. Actuators B 93, 442 (2003)

[351] Y. M. Wu, D. C. Bradley, R. M. Nix, Appl. Surf. Sci. 64, 21 (1993)

[352] Q. Xie, X.-P. Qu, J.-J. Tan, Y.-L. Jiang, M. Zhou, T. Chen, G.-P. Ru, Appl. Surf. Sci. 253, 1666 (2006)

[353] Q. Xie, Y. L. Jiang, C. Detavernier, D. Deduytsche, R. L. Van Meirhaeghe, G. P. Ru, B. Z. Li, X. P. Qu, J. Appl. Phys. 102, 083521 (2007)

[354] Q. Xie, J. Musschoot, D. Deduytsche, R. L. Van Meirhaeghe, C. Detavernier, S. Van den Berghe, Y.-L. Jiang, G.-P. Ru, B.-Z. Li, X.-P. Qu, J. Electrochem. Soc. 155, H688 (2008)

[355] Q. Xie, Y.-L. Jiang, J. Musschoot, D. Deduytsche, C. Detavernier, R. L. Van Meirhaeghe, S. Van den Berghe, G.-P. Ru, B.-Z. Li, X.-P. Qu, Thin Solid Films 517, 4689 (2009)

[356] Q. Xie, D. Deduytsche, M. Schaekers, M. Caymax, A. Delabie, X.-P. Qu, C. Detavernier, Appl. Phys. Lett. 97, 112905 (2010)

[357] Y. Xuan, Y. Q. Wu, T. Shen, M. Qi, M. A. Capano, J. A. Cooper, P. D. Ye, Appl. Phys. Lett. 92, 013101 (2008)

[358] S. V. Yakovlev, A. A. Malygin, S. I. Koltsov, V. B. Aleskovskii, Y. G. Chesnokov, I. O. Protodyakonov, J. Appl. Chem. USSR 52, 959 (1979)

[359] S. Yamamoto, A. Kawaguchi, K. Nagata, T. Hattori, S. Oda, Appl. Surf. Sci. 122, 30 (1997)

[360] J. J. Yang, N. P. Kobayashi, J. P. Strachan, M.-X. Zhang, D. A. A. Ohlberg, M. D. Pickett, Z. Li, G. Medeiros-Ribeiro, R. S. Williams, Chem. Mater. 23, 123 (2011)

[361] M. Ylilammi, T. Ranta-aho, J. Electrochem. Soc. 141, 1278 (1994)

[362] T. Yoshimura, S. Tatsuura, W. Sotoyama, Appl. Phys. Lett. 59, 482 (1991)

[363] S. J. Yun, Y. S. Kim, S.-H. K. Park, Appl. Phys. Lett. 78, 721 (2001)

[364] T. Yuranova, A. G. Rincon, A. Bozzi, S. Parra, C. Pulgarin, P. Albers, J. Kiwi, J. Photochem. Photobiol. A: Chem. 161, 27 (2003)

[365] F. Zaera, J. Mater. Chem. 18, 3521 (2008)

[366] S. Zaitsu, T. Jitsuno, M. Nakatsuka, T. Yamanaka, S. Motokoshi, Appl. Phys. Lett. 80, 2442 (2002)

[367] M. Zhang, W. Chen, S.-J. Ding, X.-P. Wang, D. W. Zhang, L.-K. Wang, J. Vac. Sci. Technol. A 25, 775 (2007)

[368] Y. Zhang, Y.-Z. Zhang, D. C. Miller, J. A. Bertrand, S.-H. Jen, R. Yang, M. L. Dunn, S. M. George, Y. C. Lee, Thin Solid Films 517, 6794 (2009)

[369] M. Zhu, H.-C. Chin, C.-H. Tung, Y.-C. Yeo, J. Electrochem. Soc. 154, H879 (2007)

[370] L. T. Zhuravlev, Colloids Surf. A: Phys. Eng. Aspects 173, 1 (2000)